A molecular dynamics investigation of water and ion transport through model carbon nanotubes

by

Lin Liu

B.Sc., Nankai University, 2011

A THESIS SUBMITTED IN PARTIAL FULFILLMENT OF
THE REQUIREMENTS FOR THE DEGREE OF

DOCTOR OF PHILOSOPHY

in

The Faculty of Graduate and Postdoctoral Studies

(Chemistry)

THE UNIVERSITY OF BRITISH COLUMBIA

(Vancouver)

March 2017

Abstract

In this dissertation, we investigate water and ion transport through carbon nanotubes using molecular dynamics simulations. Specifically, we examine how different water models influence the simulated conduction rates. We consider three common water models, which are TIP4P/2005, SPC/E, and TIP3P, and observe that water flow rates through the same nanotube are strikingly different amongst the different water models. Also, the water flow rate dependence on temperature fits an Arrhenius-type equation over a temperature range from 260 to 320 K. We provide evidence that there are two factors which determine the conduction rate: the bulk fluid mobility, and the molecular structure of confined water. For narrow nanotubes, for example, a (6,6) nanotube, where water only forms a single-file configuration, the first factor can largely account for the flow rate differences. In this case, we show that the conduction rate correlates with the diffusion coefficient of bulk water. Our simulation results are well described by continuum hydrodynamics as well. The factor of bulk fluid mobility is still important in the water conduction through intermediate-size nanotubes, such as a (9,9) nanotube. Also, the formation of complex configurations within such nanotubes can impede the transport rate by influencing the mode of water conduction. The ordered structure occurring within nanotubes can also explain the differences between simulation results and continuum hydrodynamics predictions. Hence, both factors decide the water conduction rates through intermediate-size nanotubes. Moreover, we demonstrate that the ion flow rate depends on the viscosity of the bulk solution, as well as the water structure within the nanotubes, together with the ion size. In particular, at lower temperatures complex water configurations act to impede ion transport while still allowing water to flow at a significant rate. In general, our efforts on this issue are of importance for future simulation studies investigating water and

ion conduction through nanoscopic channels. This dissertation might also prove useful in designing more efficient nanoscopic conduits for future experimental studies.

Preface

The research presented in this dissertation has appeared as co-authored, peer-reviewed publications by L. Liu and G. N. Patey. Parts of this dissertation have been published as journal articles:

- L. Liu and G. N. Patey, "Simulations of water transport through carbon nanotubes: How different water models influence the conduction rate", J. Chem. Phys., **141**, 18C518 (2014).

- L. Liu and G. N. Patey, "Simulated conduction rates of water through a (6,6) carbon nanotube strongly depend on bulk properties of the model employed", J. Chem. Phys., **144**, 184502 (2016).

- L. Liu and G. N. Patey, "A molecular dynamics investigation of the influence of water structure on ion conduction through a carbon nanotube", J. Chem. Phys., **146**, 074502 (2017).

The computer simulations and data analysis were conducted by L. Liu with guidance and suggestions from G. N. Patey. The manuscripts were written by L. Liu with revisions and polishing by G. N. Patey.

Table of Contents

List of Tables

List of Figures

List of Symbols and Abbreviations

A	Area of Membrane
D	Diffusion Coefficient
E_a	Activation Energy
N_{nt}	Number of Confined Water Molecules
P	Pressure
R	Gas Constant
R_{entry}	Entry Rate
R_{flow}	Flow Rate
R_{Stokes}	Stokes Radius
T	Temperature
U	Potential Energy
V_{nt}	Volume of Carbon Nanotube Cavity
d	Bond Length
d_{eff}	Effective Carbon Nanotube Diameter
d_{nt}	Carbon Nanotube Diameter
f	Force
f_{ex}	External Force
k_B	Boltzmann Constant
k_r	Harmonic Force Constant
n	Number of Water Molecules being Applied External Force

(n, m)	Chiral Indices
q	Point Charge
$\boldsymbol{r}$	Coordinate Vector
r	Radial Position inside Carbon Nanotube
r_{eff}	Effective Carbon Nanotube Radius
t	Time
u_C	Coulombic Potential
u_{LJ}	Lennard-Jones Potential
$\boldsymbol{v}$	Velocity Vector
w	Potential of Mean Force
ϵ_0	Vacuum Permittivity
ε	Lennard-Jones Energy Parameter
θ	Bond Angle
η	Fluid Viscosity
ξ	Ion Transport Efficiency Parameter
ρ	Particle Number Density
σ	Lennard-Jones Length Parameter
CNT(s)	Carbon Nanotube(s)
GROMACS	Groningen Machine for Chemical Simulations
LINCS	Linear Constraint Solver
LJ	Lennard-Jones
MD	Molecular Dynamics
PME	Particle Mesh Ewald
PMF	Potential of Mean Force
RC	Reduced Charge Model
RP	Reduced Lennard-Jones Parameter Model

SPC/E   Extended Single Point Charge Model

TIP3P   Three-site Transferable Intermolecular Potential Model

TIP4P/2005   Four-site Transferable Intermolecular Potential Model of 2005

WHAM   Weighted Histogram Analysis Method

Acknowledgements

First of all, I would like to express my sincere gratitude to my research supervisor, Professor Gren Patey. I am deeply impressed by his knowledge as a scholar, his diligence as a learner, and his kindness as an instructor. He is like a blazing torch in the murky maze of science, illuminating me the path to the truth. I also appreciate his patient assistance over years in helping me improving writing and presentation skills. I would not have accomplished this degree without his support.

Besides my advisor, I am grateful to my fellow group members for their cooperation, encouragement, and friendship. My thanks go to Dr. Erin Lindenberg, Dr. Jingyi Yan, and Dr. Sarah Overduin who gave me hands at the very beginning of my graduate study. I am also grateful to my committee members and chemistry department staff for all kinds of assistance.

Last but not the least, I would like to express profound gratitude to my parents for their altruistic support through my entire life. A special appreciation goes to Dr. Zhiwen Chen who did me great favors during my study in Tianjin and Vancouver. I also would like to thank my friends all around the world for their warm companionship.

Chapter 1

Introduction

The transport of water and ions through nanoscopic channels occurs commonly in a variety of physical systems. For example, water transport proteins, or aquaporins, are found in biological membranes which can efficiently and exclusively conduct water molecules.[1–4] The molecular structures[5–7] and water conduction mechanisms[4,8,9] of aquaporins have been extensively illuminated by many modern techniques such as molecular dynamics (MD) simulations and X-ray crystallography. Likewise, ion channels are those proteins which selectively convey ions across cell membranes.[10–13] One major advantage of transport proteins is that they conduct one specific particle or certain types of particles,[2,3,10,11,14] avoiding the passage of undesired molecules or ions. Also, growing research efforts demonstrate connections between transport proteins and various diseases.[15–20] Therefore the study of transport proteins and their analogs will remain a topic of interest for decades.

1.1 Molecule Transport through CNTs

Carbon nanotubes (CNTs) are allotropes of carbon. Although CNTs are of much interest for their electrical,[21] mechanical[22] and thermal[23] properties, in this dissertation we concentrate on their ability as conduction pores for water and ions. Conceptually, an open-ended, single-wall CNT can be constructed by "rolling up" a graphene sheet, which is simply one atomic layer of graphite. The synthesis methods of CNTs include arc discharge, laser ablation, chemical vapor deposition (CVD), *et cetera*.[24] The lengths of synthesized nanotubes vary from the order of micrometers to millimeters, and the diameters of cylindrical single-wall nanotubes can be less than 1 nm, while the diameters of multiple-wall nanotubes are commonly several tens

of nanometers.[24] Resembling cavities inside transport proteins, the space surrounded by the carbon scaffold allows the accommodation of molecules with diameters of several Ångströms such as water,[25–31] ethanol,[32,33] and benzene.[34] Nanoscopic compounds, for example, single-stranded deoxyribonucleic acids (DNAs)[35] and Iron(III) oxide nanoparticles,[36] can be situated within even larger CNTs.

Although it is feasible to experimentally confirm the presence of water inside CNTs employing various analysis instruments,[25–31] it is still challenging to decipher complicated molecular structures from spectra. Based on X-ray scattering data, radial density profiles of confined water have been calculated by Paineau *et al.*,[30] indicating the presence of multiple water layers. More recently Bernardina *et al.*,[31] with the help of infrared spectroscopy, have suggested that confined water molecules provide dangling $O-H$ bonds directed towards the carbon walls. Experimental scientists[33,37,38] have also demonstrated that molecule transport through CNTs is enhanced compared to what one would expect based on classical fluid dynamics. Holt *et al.*[37] have reported fast water and gas conduction rates through membranes which were made of CNTs with diameters of less than 2 nm, and Qin *et al.*[38] have discussed the dependence of rate enhancement factors on the nanotube diameter. Moreover, excellent transport efficiency across nanotube membranes is not exclusive to water but common for various liquids, including ethanol and hexane.[33] Efforts have been made on the application of the special dynamical properties of CNTs, for example in the realm of water desalination. A recent study[39] has shown that CNT-embedded polyamide membranes, which are widely used in reverse osmosis, can conduct water more rapidly than traditional, unmodified polymeric membranes.

Furthermore, proof of ionic conductance through uncapped CNTs has been given in recent articles.[35,40–44] Ion transport can be detected by monitoring electric current trace changes.[40–43] Interestingly, the mobilities of alkali cations through isolated single-walled CNTs[41,42] and CNT-doped epoxy membranes[44] have been proved very high, even exceeding their mobilities in bulk liquid. Unlike water, however, ion transport can be easily stopped if nanotube terminals are chemically modified.[45]

1.2 Computational Studies of Molecule Transport through CNTs

Unlike experimental studies, which mostly investigate a large number of widely size-distributed and poorly characterized CNTs, computational studies focus more on a small number of chemically simple nanotubes. The structure of a simple CNT can be described by a set of integers (n,m) which are called chiral indices. The details of chiral indices are presented in Chapter 2.2.

Because of the nature of graphene,[46] it is logical to expect that CNTs can not be wetted by water easily; yet simulation studies[47–53] refute this assumption. An early study carried out by Hummer *et al.*[47] observed that water can automatically enter a short, narrow CNT (with an effective diameter of ~0.5 nm). There is a debate about whether energy or entropy drives the entry of water. Kumar *et al.*[48,49] have claimed that water gains rotational entropy inside CNTs compensating for the increase in energy. Later Pascal *et al.*[50] have concluded that entropy is the primary driving force unless the diameters of CNTs are beyond a critical diameter of ~1.1 nm. Studies[51,52] also have shown that entropy is the driving factor if CNTs are partially occupied, but energy is more favorable when CNTs are fully occupied. However, Waghe *et al.*[53] have concluded that the filling is mainly induced by a decrease in energy, along with a minor increase in entropy.

Unlike in bulk liquid, confined water can form special structures inside CNTs. Due to spatial constraints, in narrow CNTs, for example, a (6,6) nanotube, only a single molecular chain configuration is observed.[47,54–57] Water molecules are aligned one next to the other, connected by hydrogen bonds. Complex configurations develop as the CNT diameter increases. Using MD methods, Koga *et al.*[58,59] applied axial pressure on confined water at low temperature, and proposed a family of polygonal structures, where water molecules cluster as polygonal structures with long-range order in the axial direction of intermediate-size CNTs (with effective diameters of ~1.0 nm). Hydrogen bonds play a fundamental role in stabilizing ring structures. Such quasi-one-dimensional structures were confirmed experimentally.[29,60]

For confined water in the liquid state, molecules can form similar polygonal (single layer) configurations but the axial periodicity vanishes.[29, 55, 61–64] Other patterns have also been reported,[65, 66] where water molecules form helical chains along the CNT axis. Within large CNTs (with effective diameters of ∼1.5 to 2.0 nm) confined water creates multilayer structures,[61, 67–69] but water inside even larger CNTs does not feel the nanotube wall, and the structure resembles that of bulk liquid.[61, 64, 68, 69]

On the macroscopic scale, pressure-driven liquid flow of an incompressible, Newtonian fluid inside a cylindrical pipe is often described as the Poiseuille flow

$$u(r) = \frac{1}{4\eta} \left(\frac{dP}{dz} \right) (r_{\text{eff}}^2 - r^2) \;, \tag{1.1}$$

where u is the flow velocity profile, η is the fluid viscosity, (dP/dz) is the pressure gradient, r_{eff} is the effective radius of pipe, and r is the radial position. The flow meets the no-slip condition where the fluid has zero velocity at the fluid-solid boundary. Note that Equation (1.1) assumes that the fluid is uniform and homogeneous. However, this assumption breaks down at the nanoscopic scale. Water molecules move cooperatively within narrow CNTs.[47, 56] Hanasaki and Nakatani[68] reported that water flow in intermediate-size CNTs has a flat velocity profile rather than a convex velocity profile, which is not compatible with Poiseuille flow. They found that the longer lifetimes of hydrogen bonds between confined water leads to the fast concerted motion of molecular clusters. Other papers[55, 70] support this observation. The flow enhancement hints that the no-slip condition likely does not hold. MD studies[71, 72] predict that the slip lengths of water decrease as CNTs become larger. The relative fast water conduction through CNTs is found to be closely related to the confined structure. Some articles[63, 72] have shown that increasing the curvature of CNTs can significantly reduce the friction at the fluid-solid interface. Joseph and Aluru[73] concluded that the hydrophobic surfaces could influence water molecule orientation in the proximity of CNTs and, therefore, enhance conduction rates.

Several studies have discovered that water flow rates are sensitive to particular features of CNT conduits, for example, the electrical charge.[74–80] Most of the MD simulations mentioned

above adopt the approximation that no carbon atoms have partial charges, yet this is not the case.[81,82] Using *ab initio* MD simulations Won *et al.*[74] and Sahu *et al.*[75] investigated the effect of partial charges on the dynamics of water. They concluded that partially charged CNTs can induce a dipole moment, reorient water molecules, and make them more readily accessible to CNT orifices. Lu[76] proposed that the dipole moment also prevents single-file molecules from flipping, and, therefore, enhances water transport rates. Li *et al.*[77] devised a controllable nanoscopic fluid switch by adjusting the position of external charges. Other factors that influence flow include conduit defects,[83,84] channel hydrophobicity,[85–87] and chemical modification.[75,88,89]

It is intuitively evident that the diameters of CNTs must exceed the diameters of ions in order to allow ion entry and conduction. Using equilibrium MD simulations, Peter and Hummer[90] discovered that narrow CNTs block ions, but intermediate-size CNTs are Na^+ permeable. However, computer simulations[91] suggested that CNTs can reject hydrated F^- whose radius is greater than the ionic radius of F^-. Theories about ion hydration/dehydration are often mentioned to resolve such problems. In bulk solution, water molecules arrange adjacent to ions, composing layers of hydration shells. The effective radius of a hydration shell is determined by the ionic radius and the number of charges an ion bears. Studies[92–94] have demonstrated that the structure of hydration shells is strongly influenced by confinement in CNTs, therefore, to enter narrow CNTs some water molecules have to be removed from the hydration shell, giving rise to free energy penalties.[90,91,95,96] In contrast, within wide CNTs, ions are better stabilized by interacting with more neighboring water molecules.[92] Generally speaking, it is less energetically expensive for ions to move through wide CNTs due to the minor alteration of hydration shells.

Computer simulations have revealed that the CNT diameters strongly influence the dynamics of ion transport through nanotubes. The scaffold of narrow CNTs can hinder the three-dimensional ion diffusion.[97–99] While enhanced ion mobilities in wide CNTs (with effective diameters of ∼2.0 nm), compared to the bulk solution, have been reported,[100] because of the recovery of bulk-like water structure but with less ion pairing. Moreover, other fac-

tors can also influence the ion dynamics, including charge distribution on CNTs,[101–103] ion concentration,[104] and external electric fields.[105]

CNTs have been suggested as a promising material for nano-filtration. As indicated above, narrow nanotubes can naturally exclude ions without obstructing water transport.[90,95,106] Hence nanotubes are promising candidates as nanoscopic filters for desalination of sea water. Although intermediate-size nanotubes permit ions to pass through, computational research[88,89] has demonstrated that chemical modification of such CNTs can optimize the efficiency of nanotubes as filtration systems. Also, it is possible to design nanoscopic devices to select or detect specific ions. For example, the selection between Na^+ and K^+ using CNTs is a topic of interest. Investigations[107–110] have revealed that nanotube preferences for different ions are primarily regulated by the particular hydration shell structures of Na^+ and K^+ (including ion coordination number, the effective radius of hydration shell, and the intensity of which an ion holds surrounding waters) under specific conditions. Gong *et al.*[111] pointed out that charge attraction/repulsion between modified CNTs and ions can improve selection ability as well.

1.3   Water Models

In molecular simulations, a water model is a set of interaction parameters that describe the physical properties of explicit water molecules in the aqueous phase. The first water model was proposed by Bernal and Fowler[112] in 1933. The optimization of water models has been a work in progress for almost a century; several tens of water models have been proposed — the three-site transferable intermolecular potential model (TIP3P),[113] the extended single point charge model (SPC/E),[114] the atomic multipole optimized energetics for biomolecular applications model (AMOEBA),[115] the four-site transferable intermolecular potential model of 2005 (TIP4P/2005),[116] and the six-site simple water model (SWM6),[117] just to name a few.

Unfortunately, there is not a single water model today which can perfectly describe all

physical properties of water in nature. In parameterizing water molecules, many factors must be considered all together, including quantum mechanics, molecular mechanics, and experimental results.[118] A water model is often detailed in three aspects. First, the number of interaction sites. Considering Coulomb interactions, for the most widely used water models such as TIP3P and TIP4P/2005, a point charge approximation is commonly applied, where molecules are described by several sites bearing either positive or negative partial charges. However, a limited number of sites poorly reproduce the actual charge distribution. An earlier study[119] has demonstrated that a water molecule is better approximated by a combination of point charges on nuclei and diffuse spherical charge densities around them. Second, the model can be flexible or not. The use of rigid bonds where distances between interaction sites are fixed to simplify computation complexity is often assumed, but in reality, chemical bonds are constantly vibrating. Models taking molecular flexibility into consideration can give more accurate results for some physical properties of water obtained in simulations, for example, the heat capacity at constant volume.[120] To introduce flexibility in water models, the oscillation of bonds and angle can be described as simple harmonic potentials or more complicated forms.[121–123] Third, the model can be polarizable or not. In empirical models, it is often assumed that molecular polarizability is unaffected by the environment. For nonpolarizable water models, partial charges are specifically parameterized to generate an appropriate dipole moment[114] similar to that of real water in liquid state. However, these models may not be accurate in anisotropic environments, such as the proximity of a water-membrane interface or in the presence of an electric field. When inventing polarizable water models, the induced-dipole technique, the Drude-oscillator technique, and the fluctuating-charge technique are three popular methods to explicitly take molecular polarizability into account.[124]

An all inclusive, complicated water model can certainly enhance the accuracy of simulation results, but can also considerably increase the computational cost. It is important to keep a balance between the efficiency of calculation and the reliability of conclusions. In this case, it is necessary to examine and compare different simplified water models and identify those which will compromise least on simulation accuracy. Additionally, note that almost

all water models are designed to reproduce the physical characteristics of bulk water, and it is likely that such properties can get skewed within confined regions, for instance within CNT cavities. Therefore, deciding the best water model candidates for special anisotropic conditions is important.

Investigations of the influence of different water models were pioneered by Alexiadis and Kassinos.[125–127] They systematically examined some water properties in single-wall CNTs with diameters ranging from 0.7 to 5.5 nm using MD simulation. Two families of three-site water models, TIP3P and SPC,[128] were investigated, including both rigid and flexible models. Although the confined water densities were similar within a (13,5) nanotube, they[126] suggested that the rigid SPC/E model produces an obvious pentagonal configuration, while the structure of the rigid TIP3P model is less ordered. They[127] also discussed the effect of flexibility of water versions. By squeezing H−O−H bond angles, flexible water molecules are packed more densely inside CNTs, and, therefore, greater average numbers of hydrogen bonds were observed in simulations, yet the variances of the numbers from rigid models were less than 10%. The flexible water models showed high similarities on selected physical properties, even though they are from two different families.

Inspired by the early work, other studies have been conducted during the past five years. Nakamura and Ohno[129] investigated the influence with more families of water models: three-site (TIP3P and SPC/E), four-site (the four-site transferable intermolecular potential model, TIP4P[113]), and five-site (the five-site transferable intermolecular potential model for use with Ewald sum, TIP5P-E[130]). They investigated water configurations within (8,8) and (9,9) CNTs. It was shown that the water model employed can strongly influence the water structure. TIP3P water is disordered, as noted in Reference 126; SPC/E water has structures of stacked water clusters; TIP5P-E has complicated single-helix structures running through CNTs. Moreover, the confined configurations of TIP4P water resemble those of SPC/E in the (8,8) CNT but are similar to TIP3P in the (9,9) CNT. Kumar *et al.*[131] evaluated the effects of model flexibility and polarizability. They discovered that the inclusion of polarizability improved the accuracy of results for some dynamical properties (as compared to *ab initio*

simulations), but that the inclusion of flexibility did not. They concluded that the classic SPC/E model appears to be the most excellent candidate for the study of confined water molecules because it leads to sufficiently accurate results with lower computational cost.

1.4 Outline of Dissertation

The overall purpose of this dissertation is to study how and why different water models influence the simulated particle conduction through CNTs. It is interesting to see that both water and ion conduction rates are very sensitive to the water model employed in simulations. For water, we attribute such difference to two factors, bulk fluid diffusivity and molecular structure within nanotubes. For ion transport, we provide evidence that the water structure inside an intermediate-size nanotube also has an impact on ion transport through CNTs.

This dissertation is presented in six chapters. Chapter 1 overviews the background of water and ion conduction through CNTs and points out the necessity of studying water model influences. Chapter 2 describes the molecular models employed, the simulation setup, and various analysis techniques. Chapters 3 and 4 thoroughly investigate, for both narrow and intermediate-size nanotubes, water conduction, confined water structure, and the related thermodynamic and continuum hydrodynamic features that arise from different models. Chapter 5 discusses the influence of water models on water and ion transport through an intermediate-size nanotube. Finally, Chapter 6 summarizes the conclusions and comments on the future outlook in this field.

Chapter 2

Models and Methods

2.1 Modelling of Water

In this dissertation, we examine three widely used water models: the three-site transferable intermolecular potential model (TIP3P),[113] the extended single point charge model (SPC/E),[114] and the four-site transferable intermolecular potential model of 2005 (TIP4P/2005).[116] We select the TIP3P and SPC/E models because they are among the most popular water models in use, and include the TIP4P/2005 model because it best reproduces the properties of ambient bulk water.[132] The first two models are three-site models, including one oxygen atom and two hydrogen atoms, while the third is a four-site model, with an additional virtual site at the bisector of the $H-O-H$ bond angle, representing electron distribution around the oxygen atom. The molecular geometries of the water models are displayed in Figure 2.1, and the geometric parameters are summarized in Table 2.1. Note that all water models investigated are rigid and nonpolarizable.

Water model	d_{O-H} (nm)	d_{O-M} (nm)	θ_{H-O-H} (degree)
TIP4P/2005	0.0957	0.0155	104.5
SPC/E	0.1000	n/a	109.5
TIP3P	0.0957	n/a	104.5

Table 2.1: List of geometric parameters of water models. d represents the distance between sites, and θ represents the bond angle. The oxygen atom, hydrogen atoms, and the virtual site are denoted as O, H, and M, respectively.
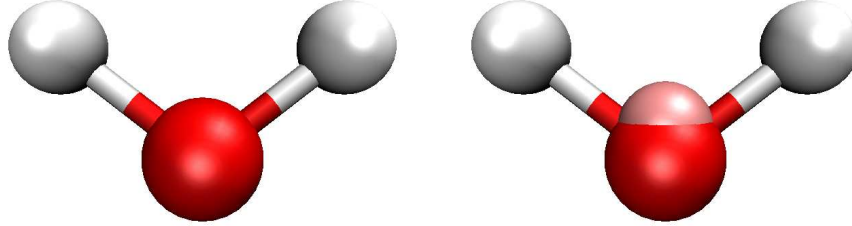
Figure 2.1: Illustrations of three-site (left) and four-site (right) water model geometries. Oxygen atoms are red, hydrogen atoms are gray, and the virtual midpoint site is pink.

2.2 Modelling of CNTs

The structure of a CNT can be described by a set of integers (n,m) which are called chiral indices. The set defines how the nanotube is "rolled up" from a graphene sheet (see Figure 2.2). If $n = m$ the CNTs are called armchair nanotubes, and if $m = 0$ they are called zigzag nanotubes. Otherwise, CNTs are termed chiral. Figure 2.3 illustrates a pristine (6,6) CNT. It is possible to calculate the diameter of a nanotube, d_{nt}, from its chiral indices (n,m)

$$d_{nt} = \frac{a}{\pi}\sqrt{3(n^2 + nm + m^2)} \ , \tag{2.1}$$

where a is 0.142 nm, the length of a carbon-carbon bond. An effective diameter, d_{eff}, can also be calculated if we take the van der Waals radius of a carbon atom, r_{carbon}, into consideration

$$d_{eff} = d_{nt} - 2r_{carbon} \ , \tag{2.2}$$

where d_{nt} is from Equation (2.1) and r_{carbon} is 0.17 nm.[95] Note that in the current investigation we assume that CNTs are rigid with no termination, which is an approximation regularly used in CNT studies.[47,77,88,95,97,107,129] MD research articles investigating the effects of nanotube
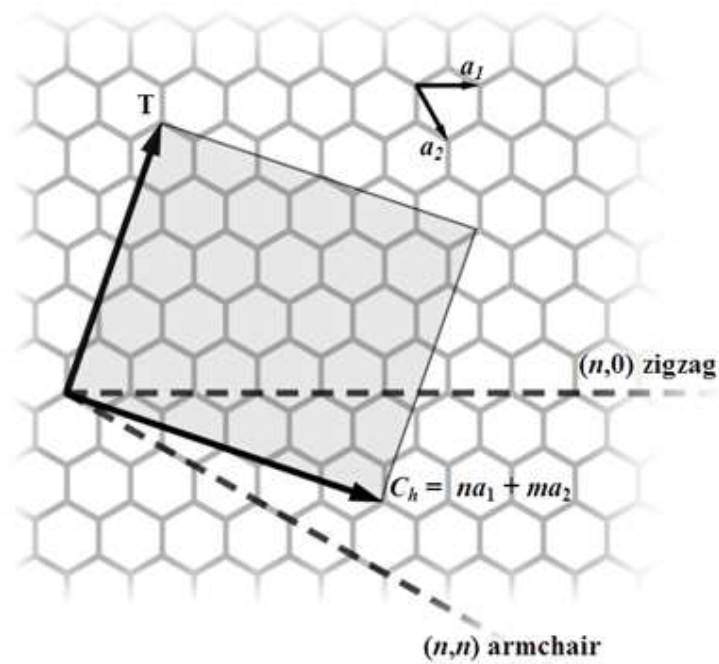
Figure 2.2: Illustration of chiral indices. a_1 and a_2 are unit vectors of the graphene sheet. An (n,m) CNT is conceptually constructed by "rolling up" the graphene plane along the vector $C_h = na_1 + ma_2$; T denotes the CNT axis. This figure is from Wikipedia with permission.
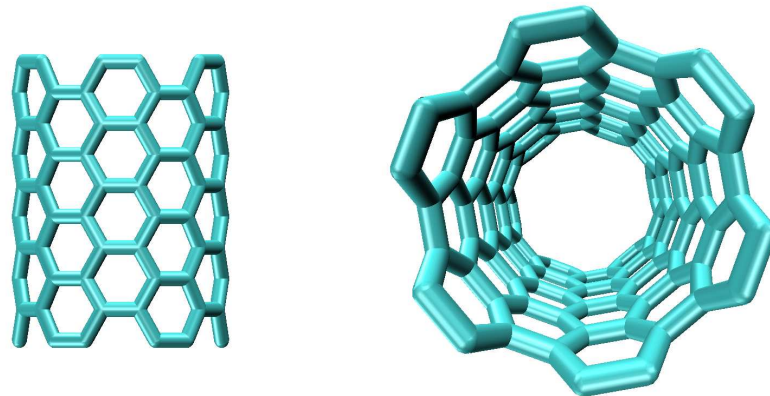
Figure 2.3: Illustrations of a side view (left) and a top view (right) of a pristine (6,6) CNT. Carbon-carbon bonds are depicted as cyan cylindrical segments.

12

flexibility[92, 126, 127, 133] and termination[75, 89] are available.

In this dissertation, the terms *CNT(s)* and *nanotube(s)* are used interchangeably.

2.3 Interaction Potentials

In our models, all site-site interactions involve Lennard-Jones (LJ) and Coulombic terms. The LJ potential is a model to approximate the van der Waals interaction between a pair of atoms. $u_{\text{LJ},ij}$, the LJ potential between atom i and j, has a simple expression

$$u_{\text{LJ},ij} = 4\varepsilon_{ij} \left[\left(\frac{\sigma_{ij}}{|\boldsymbol{r}_{ij}|} \right)^{12} - \left(\frac{\sigma_{ij}}{|\boldsymbol{r}_{ij}|} \right)^{6} \right] , \tag{2.3}$$

where ε_{ij} is the depth of the potential well, σ_{ij} is the distance at which $u_{\text{LJ},ij}$ is exactly zero, and $|\boldsymbol{r}_{ij}|$ is the distance between atoms i and j. The pair LJ parameters (ε_{ij} and σ_{ij}) are computed by the Lorentz-Berthelot combination rule from atomic force field parameters

$$\varepsilon_{ij} = \sqrt{\varepsilon_i \varepsilon_j} , \tag{2.4}$$

$$\sigma_{ij} = \frac{\sigma_i + \sigma_j}{2} . \tag{2.5}$$

In practice, given that $u_{\text{LJ},ij}$ converges to zero quickly, it is reasonable to presume that the long-range $u_{\text{LJ},ij}$ is negligible. The LJ cut-off radius in this dissertation is 1.2 nm, and the total LJ contribution to the potential energy will be simply the sum of all pairwise interactions whose $|\boldsymbol{r}_{ij}|$ is within this arbitrary cut-off radius. The pair electrostatic potential $u_{\text{C},ij}$ of sites i and j who both bear charges is given by Coulomb's Law

$$u_{\text{C},ij} = \frac{q_i q_j}{4\pi\epsilon_0 |\boldsymbol{r}_{ij}|} , \tag{2.6}$$

where q_i and q_j are charges on interaction sites i and j, and ϵ_0 is the vacuum permittivity. However, unlike $u_{\text{LJ},ij}$, $u_{\text{C},ij}$ decays to zero very slowly, which means the long-range $u_{\text{C},ij}$ still

significantly contributes to the total potential. Given that the periodic boundary conditions are used in MD simulations, as a result, we have to consider interactions of a given charge with not only other charges in the same simulation cell but also with all images (including itself) in the periodic cells. In practice, the particle mesh Ewald (PME) method[134, 135] is used to calculate the total electrostatic interactions. In this method, the slowly converging sum can be obtained from two quickly converging terms, one in real space and the other in reciprocal space. The real space PME electrostatics is truncated at 1.2 nm. The reciprocal space PME summation uses more than 85 wave vectors in each direction.

All atomic force field parameters are summarized in Table 2.2. Parameters for a carbon atom are from the AMBER03 force field.[136] Parameters for different water models are from References 113, 114, and 116. Parameters for ions are those proposed by Joung and Cheatham,[137] which are specifically optimized for different water models. Because optimized ion parameters for the TIP4P/2005 model are not available, we use those for the TIP4P-Ew model instead. Furthermore, two arbitrarily modified TIP4P/2005 water models are designed in this dissertation so as to reveal the mechanism by which water transport through nanotubes depends on the water model employed. The revised force field parameters are described in Chapter 4.4.

2.4   Simulation Details

The simulation cell is illustrated in Figure 2.4. The cell is a rectangular hexahedron with Cartesian dimensions (x, y, z) of (5.116 nm, 5.168 nm, 7.569 nm) unless otherwise stated. Two rigid graphene sheets with appropriate openings are located in xy planes, and an open-ended CNT, whose symmetry axis is along the z direction, is embedded within the graphene sheets. In this dissertation, we examine three sizes of armchair CNT: (6,6), (8,8), and (9,9). The length of the nanotube is fixed at 3.561 nm. From Equation (2.2) the effective diameters of (6,6), (8,8) and (9,9) CNTs are 0.474, 0.745, and 0.881 nm, respectively. The skeleton of carbon atoms can be regarded as a permeable membrane, separating the cell into two

Atom	σ (nm)	ε (kJ mol^{-1})	q (e)
	CNT		
C	0.3400	0.3598	0.0000
	Water — TIP4P/2005		
O	0.3159	0.7749	0.0000
H	0.0000	0.0000	+0.5564
M	0.0000	0.0000	−1.1128
	Water — SPC/E		
O	0.3166	0.6502	−0.8476
H	0.0000	0.0000	+0.4238
	Water — TIP3P		
O	0.3151	0.6364	−0.8340
H	0.0000	0.0000	+0.4170
	Ion — TIP4P-Ew		
Na$^+$	0.2184	0.7050	+1.0000
Cl$^-$	0.4918	0.0488	−1.0000
	Ion — SPC/E		
Na$^+$	0.2160	1.4761	+1.0000
Cl$^-$	0.4830	0.0535	−1.0000
	Ion — TIP3P		
Na$^+$	0.2439	0.3660	+1.0000
Cl$^-$	0.4478	0.1490	−1.0000

Table 2.2: A list of the force field parameters used in the present dissertation.
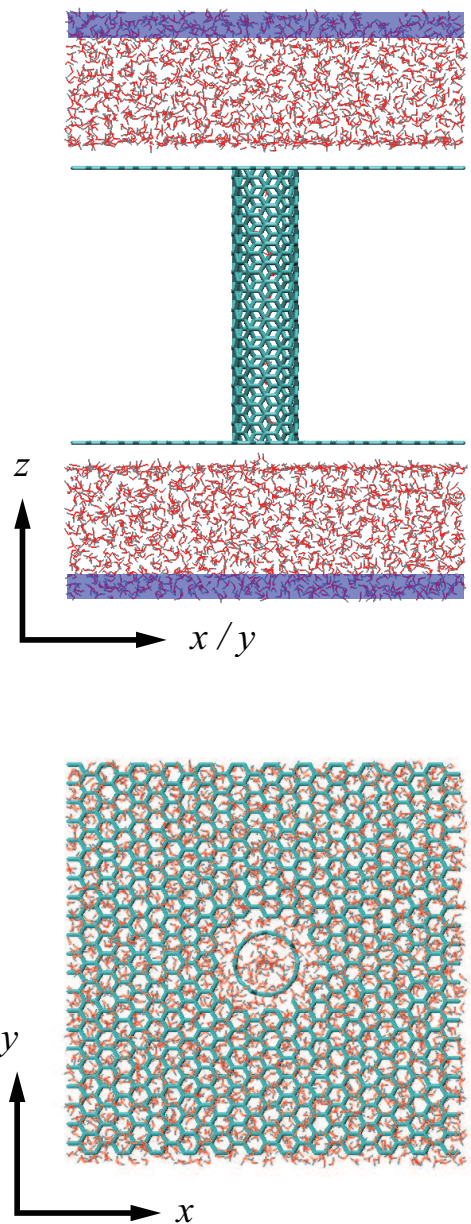
Figure 2.4: Illustrations of a side view (top) and a top view (bottom) of the simulation cell, representing a permeable membrane which contains a (6,6) CNT connecting two water reservoirs. Carbon atoms are cyan, oxygen atoms are red, and hydrogen atoms are gray. The (x, y, z) dimensions of the rectangular hexahedral cell are (5.116 nm, 5.168 nm, 7.569 nm). The region highlighted by blue shadow denotes the region where the external force is applied to water oxygen atoms.

reservoirs. During simulations, all carbon atoms are frozen at the initial positions.

The reservoirs are filled with either water or NaCl solutions of varying concentration. The density of water was set at approximately 1 g cm^{-3}, taking the van der Waals radius of carbon atom into account when calculating the fluid volume. The systems included 3266, 3299, and 3322 water molecules for (6,6), (8,8), and (9,9) CNTs, respectively. NaCl solutions were considered only for the (9,9) nanotube. Initially, identical systems were replicated as previously described for the (9,9) nanotube; then water molecules were randomly substituted with either Na$^+$ or Cl$^-$ ions. The simulations considered contained 15, 60, and 166 ion pairs, giving NaCl solutions of approximately 0.25, 1, and 2.8 mol L^{-1}, respectively.

We employed the GROMACS package[138] (version 4.5.5, double precision) for MD simulations. Periodic boundary conditions were implemented in all three dimension. All MD simulations were carried out in the canonical (NVT) ensemble using a time step of 2 fs. Most simulations were 10 ns in duration, with first 1 ns being sufficient to establish steady state flow, and data were collected from the last 9 ns. For each system, at least five individual simulations with different starting configurations were conducted, and these were used to calculate averages and estimated standard deviations. The system temperature was maintained using the velocity rescaling algorithm of Bussi *et al.*[139] A brief description of the thermostat is given in Appendix A.3. We investigated fluid structural and dynamical properties at four different temperatures: 260, 280, 300, and 320 K.

2.5 Application of Pressure Difference

To maintain a stable fluid flow through a CNT channel, a hydrostatic pressure difference, ΔP, was applied. In this dissertation we used the algorithm proposed by Zhu *et al.*[140] In this method, a constant force along the z axis is applied to a subset of water molecules. Then the pressure difference in z direction is determined by

$$\Delta P = \frac{n f_{\text{ex}}}{A} \ , \tag{2.7}$$

where n is the total number of molecules in the subset, f_{ex} is the constant external force, and A is the area of the membrane.

The original algorithm proposed by Zhu *et al.*[141] uses the same expression as Equation (2.7) to calculate the pressure difference but applies the force to all water molecules in both reservoirs, including those adjacent to the orifice of the CNT conduit. However, this setup may artificially accelerate the rate of water permeating the channel. This drawback can be overcome by applying the external force only to water molecules located at the top and bottom of the periodic simulation cell (see Figure 2.4). Suk and Aluru[142] demonstrated that the revised algorithm could generate the correct pressure difference across the membrane. Only the oxygen atoms of water were subjected to the external force, avoiding instigating additional molecular rotation. In investigating the NaCl solutions, no force was applied to the ions, which prevents the artifact of unequal concentrations between reservoirs. The regions where the force was exerted were 0.2 nm thick, including about 360 water molecules in the subset. The area of the membrane was 26.44 nm^2 (5.116 nm $\times$ 5.168 nm). In implementing this algorithm on the GROMACS platform efficiently, the subset list was updated every 10 ps, rather than at every time step. We verified that within reason altering the thickness of the regions or the period of subset update has no significant qualitative effect, and some supplemented information is presented in Appendix B.3. In our simulations, the target pressure difference was set at 220 MPa, except when otherwise specified. Note that this pressure difference is too high to be physically realistic, but a large value is necessary to ensure efficient samples on simulation time scales.

Other algorithms for providing a pressure gradient include a reflecting particle membrane,[63] a fluidized piston model,[68] a movable piston model.[143]

2.6 Data Analysis

During the production phase of simulations, trajectories and velocities of molecules were periodically recorded. By examining and interpreting these results using programs and scripts

we obtain useful structural and dynamical information.

2.6.1   Flow Rates and Entry Rates

The flow rate, R_{flow}, is defined as the number of particles that pass through the nanotube (entering from one end and leaving the other) per unit time. This definition is widely used in similar investigations.[73,74,85,88,95] Under a pressure difference of hundreds of MPa, transport events are only observed in the direction of the external force.

The entry rate, R_{entry}, is defined as the number of particles that enter from the feed reservoir into the nanotube interior per unit time. By examining the entry rate, we learn how frequently a particle enters the nanotube orifice from the bulk liquid. For calculation purposes, a particle is considered to have entered the nanotube if its center passes the nanotube orifice shown in Figure 2.4. Note that for water the molecular center is taken to be the oxygen atom. Once entered, a particle can continue to traverse the nanotube or be rejected back into the bulk. To avoid overcounting entries due to the same particle "vibrating" back and forth across the plane defining entry, we count only the first entry of any given molecule in the calculation of the entry rate.

2.6.2   Characterization of Confined Configurations

The formation of hydrogen bonds are ubiquitous between water molecules, and is a straightforward property to investigate. We employ the hydrogen bond criteria proposed by Luzar and Chandler.[144] The criteria for a hydrogen bond are twofold: the angle of $O_{\text{acceptor}}-O_{\text{doner}}-H$ must be less than 30 degrees and the distance between O_{acceptor} and O_{doner} less than 0.36 nm. Average numbers of hydrogen bonds for confined molecules were calculated during the data analysis.

As noted in Chapter 1, different polygonal water clusters are commonly observed within intermediate-size nanotubes. We identify just stacked ring structures in our simulations, but no long-range spiral configurations are found inside either (8,8) or (9,9) nanotubes. Here we describe the empirical method used to analyze ring clusters in detail. (1) Sort all oxygen

atoms in ascending z coordinate in the interior of the nanotube. (2) Starting from the top of the list, define cluster boundaries between atoms whose z coordinate gap are greater than 0.1 nm. (3) Calculate the z coordinate distance from the top to the bottom atom of each cluster. In our analysis, water molecules are considered to be part of the same ring configuration if the differences in the z coordinate of their oxygen atoms are all less than 0.15 nm, and those molecules are designated as ring-bound. We assign clusters to different categories, square, pentagonal, and hexagonal corresponding to those having 4, 5, and 6 molecules, respectively. All remaining water molecules are labeled as ring-free. Note that the distance criteria (0.1 and 0.15 nm) employed in the procedure as mentioned earlier are arbitrary, but they are sufficient to ensure that molecules are arranged as rings rather than small coils or random configurations.

2.6.3 Diffusion Coefficient

To better understand the mechanism of model dependence, we investigate bulk self-diffusion coefficients for water and ions (D_{water} and D_{ion}). The MD simulations used for diffusion coefficient calculations were conducted under equilibrium conditions in a fixed cubic cell of length 3.000 nm. For pure water, there were 903 water molecules within the cell, such that the density of bulk liquid was 1.00 g cm^{-3}. For NaCl solutions, random water molecules were replaced by 4, 16, and 45 pairs of Na$^+$ and Cl$^-$ ions, giving 0.25, 1, and 2.8 mol L^{-1} solutions, respectively. Each simulation was run for 100 ns at a constant temperature, the first 5 ns for equilibrium, and the last 95 ns for data collection. The diffusion coefficients, D, are obtained using the Einstein relation via mean square displacements in the usual manner[52, 55]

$$D = \lim_{t \to \infty} \frac{\langle |\boldsymbol{r}(t) - \boldsymbol{r}(0)|^2 \rangle}{6t} \ , \tag{2.8}$$

where $|\boldsymbol{r}(t) - \boldsymbol{r}(0)|$ is the three-dimensional particle displacement during a time period of t, and the angular brackets indicate an average over all particles.

2.6.4   Potential of Mean Force

The calculation of free energy differences is essential in computational science. The potential of mean force (PMF) is helpful in calculating free energy changes along particular reaction coordinates. The basic concepts of PMF are presented in Appendix A.4. In this dissertation, we investigate the free energy profiles of water/ions along the symmetry axis of a CNT. To obtain the PMF profiles, $w(z)$, for water, we use the average densities from equilibrium simulations[95]

$$w(z) = -k_B T ln \left[\frac{\rho(z)}{\rho_0} \right] \; , \tag{2.9}$$

where $\rho(z)$ is the number density profile as a function of z coordinate along the axis, and ρ_0 is the density of bulk water.

Free energy profiles for ions are calculated using umbrella sampling.[145,146] A bias potential function, $U_i^{\text{bias}}(z)$, of the harmonic form, was applied to a selected ion

$$U_i^{\text{bias}}(z) = \frac{1}{2} k_r (z - z_i)^2 \; , \tag{2.10}$$

where k_r is the force constant taken to be 1000 kJ mol^{-1} nm^{-2}, and z_i is the target z coordinates along the central axis. The target positions were moved from 0.5 nm to 3.5 nm with an interval of 0.1 nm. Each window simulation had a duration of 10 ns and a time step of 2 ps. The weighted histogram analysis method (WHAM) algorithm,[147] which calculates PMF profiles, was achieved using the GROMACS built in program *g_wham*.

Chapter 3

Simulated Water Conduction Rates through Intermediate-size CNTs *

3.1   Overview

A previous MD study by Nakamura and Ohno[129] investigated water structure inside (8,8) and (9,9) CNTs and discovered convincing structural differences amongst water models. However, their simulations and model comparisons apply only to equilibrium conditions, and not to the nonequilibrium cases. Motivated by this work, we investigate whether confined water still exhibit model dissimilarities when undergoing pressure-driven flow. We find that the flow rate is significantly influenced by the water model employed. We trace the dynamical discrepancies to the structure taken on by the water molecules inside nanotubes. Two distinct conduction modes are proposed to explain why flow rates through intermediate-size nanotubes are remarkably different for various water models.

3.2   Water Flow Rates through Intermediate-size CNTs

In Figure 3.1 we plot typical cumulative counts of water molecules passing through both (8,8) and (9,9) nanotubes at 300 K as functions of time. At the pressure difference used in our simulations, water only traverses the nanotube in the same direction as the external force. It is interesting to observe that, starting at 1 ns, the counts are essentially linear in time regardless of the size of nanotube or the water model employed in the simulations. Figure 3.1

---

shows that a 1 ns period is sufficiently long to establish steady state flows. The average flow rate R_{flow} is commonly used to describe the conduction ability of CNTs. The different slopes represent the flow rates and are obtained by linearly fitting the cumulative counts curves. From Figure 3.1, it is also obvious that the flow rates are not identical for different water models.

Average flow rates, which means the average number of water molecules passing through the nanotube during a time period of 1 ns, with estimated standard deviations at 300 K, for all three models and different nanotubes are tabulated in Table 3.1. The results show that the water conduction rate is strongly dependent on the type of model employed. The TIP4P/2005 model has the slowest flow rates while the TIP3P model has the fastest; flow rates for SPC/E are intermediate, but closer to those of TIP4P/2005. The rate ratio between the slowest and fastest models is approximately five.

3.3 Water Structure inside Intermediate-size CNTs

Before discussing our results, we briefly review the work of Nakamura and Ohno.[129] Under equilibrium conditions, these authors studied the effect of different water models on molecular structures within armchair CNTs considering a total of four water models: TIP3P, SPC/E, TIP4P, and TIP5P-E. Their MD simulations were conducted at 280 and 300 K. From density profiles, they found that the difference between models is negligible inside narrow nanotubes, but becomes significant inside intermediate-size CNTs. In particular, for (8,8) and (9,9) nanotubes, confined TIP3P water has a lower density, and less ordered structure compared

Water model	$R_{\text{flow},(8,8)}$ (ns^{-1})	$R_{\text{flow},(9,9)}$ (ns^{-1})
TIP4P/2005	51 (4)	107 (6)
SPC/E	111 (4)	134 (14)
TIP3P	287 (5)	492 (15)

Table 3.1: Average flow rates for different water models in (8,8) and (9,9) nanotubes. The simulations were conducted at 300 K. The numbers in parenthesis are estimated standard deviations.
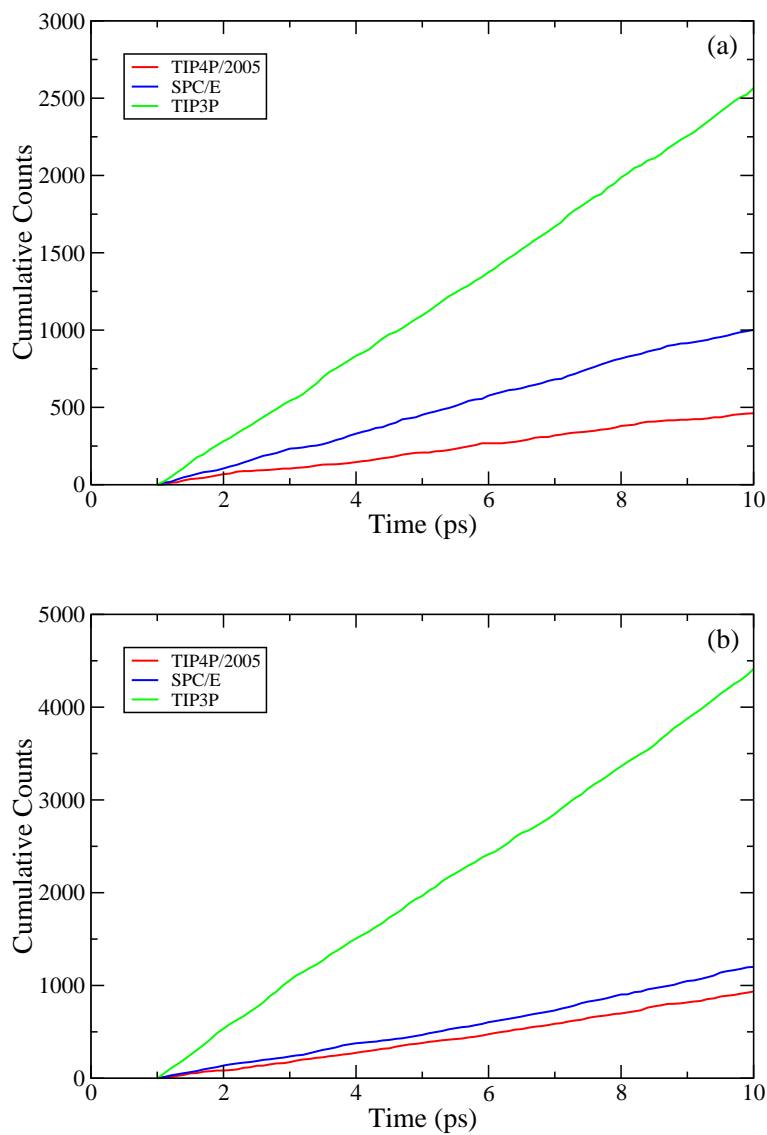
Figure 3.1: Cumulative counts curves showing the number of water molecules that pass through (8,8) [panel (a)] and (9,9) [panel (b)] nanotubes as functions of time. Note that counts during first 1 ns are not displayed because this is the equilibration period. The red, blue, and green curves are for the TIP4P/2005, SPC/E, and TIP3P models, respectively.
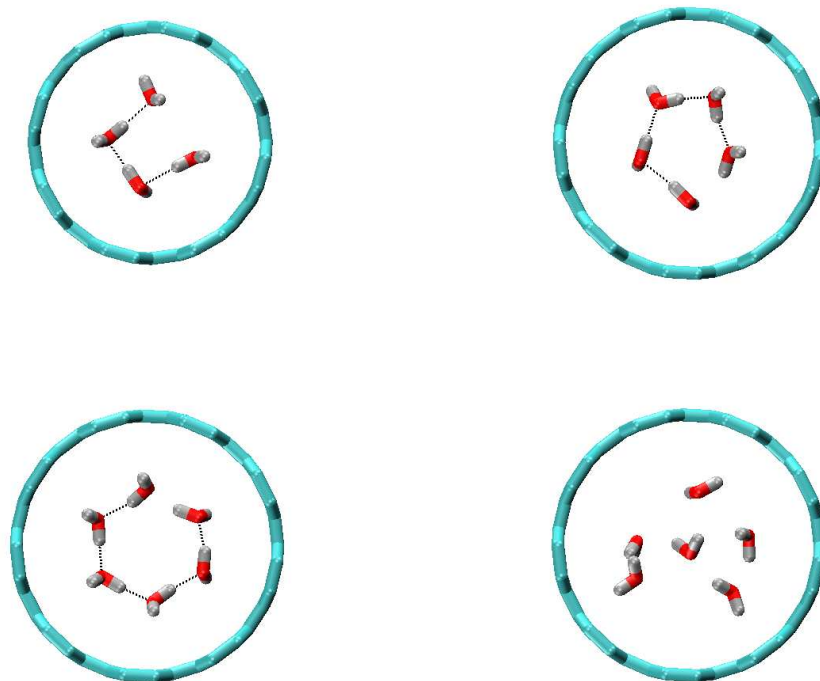
Figure 3.2: Examples of local water configurations inside nanotubes: a square configuration of TIP4P/2005 water in the (8,8) nanotube (top left), a pentagonal configuration of TIP4P/2005 water in the (9,9) nanotube (top right), a hexagonal configuration of SPC/E water in the (9,9) nanotube (bottom left), and a less ordered TIP3P water cluster (bottom right). Carbon atoms are cyan, oxygen atoms are red, and hydrogen atoms are gray. The black dotted lines indicate hydrogen bonds.

to the other water models considered. The SPC/E and TIP4P models result in stacked water rings structures, while TIP5P-E water molecules form a spiral structure running through the nanotube. They investigated confined water orientation as well. For the SPC/E and TIP4P models, they observed antiferroelectric arrangements with the net dipole moment along nanotube axis fluctuating about zero. For the TIP5P-E model, they observed a ferroelectric arrangement with a non-zero dipole moment in the axial direction. Finally, they also predicted that for SPC/E and TIP4P water, ring structures would have to enter/exit nanotubes as a whole. Because of the structural diversity under equilibrium conditions, we were curious as to whether or not such diversity remains under nonequilibrium circumstances.

In Figure 3.2 we illustrate examples of local water structures inside nanotubes, including
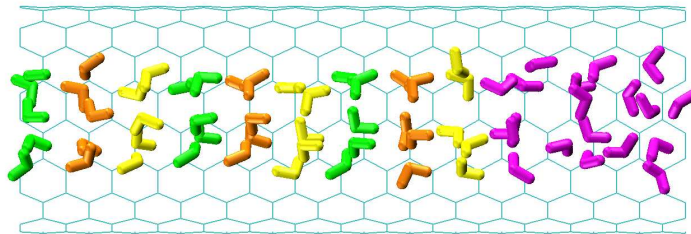
Figure 3.3: A configurational snapshot of TIP4P/2005 water in the (9,9) nanotube. Carbon atoms are cyan, stacked pentagonal ring structures are repeating green, orange and yellow, ring-free water molecules are magenta. Note that part of the carbon nanotube is not displayed for visual clarity.

different ring configurations and less ordered clusters. Water molecules which form a ring configuration ("ring-bound" as defined in Chapter 2.6.2) associate with hydrogen bonds. Owing to spatial constraints, there are very few pentagons, and no hexagons found in the (8,8) nanotube, whereas, all three ring structures do exist in the (9,9) nanotube. Water molecules from less ordered clusters ("ring-free" as defined in Chapter 2.6.2) appear as more randomly positioned and oriented. A configurational snapshot of confined water in a (9,9) nanotube is shown in Figure 3.3. Stacked ring structures are highlighted using repeating green, orange, and yellow color schemes. The disordered molecules are colored magenta. It is also interesting to note that the stacked ring clusters of liquid water, to some extent resemble the ice structures reported in CNTs at lower temperatures.[58, 59] Nevertheless, axial long-range order, as found for ice, does not occur because of the presence of ring-free molecules together with the random molecule orientation of individual clusters. Note that molecules can and do switch between ring-bound and ring-free states as the simulation evolves.

To gain insight into how the water structure varies for different models in (8,8) and (9,9) CNTs, we quantitatively inspected all systems considered for ring-bound and ring-free molecules; to be more specific, we divided the ring-bound molecules into those that are members of square, pentagonal, or hexagonal rings. The method employed is described in Chapter 2.6.2. The results are summarized for both nanotubes in Table 3.2. It is apparent that

Water model	Square (%)	Pentagon (%)	Hexagon (%)	Ring-free (%)
		(8,8) CNT		
TIP4P/2005	96.7	0.2	0	3.1
SPC/E	74.2	0.6	0	25.2
TIP3P	28.7	0.3	0	71.0
		(9,9) CNT		
TIP4P/2005	3.3	49.2	34.9	12.6
SPC/E	2.8	12.3	72.3	12.6
TIP3P	12.9	20.0	3.0	64.1

Table 3.2: The average percentage of water molecules in different structural states inside (8,8) and (9,9) nanotubes.

the fractions of ring-bound and ring-free molecules differ considerably from one model to another. Amongst the three models considered, TIP3P water has the largest number of ring-free molecules, with 71.0% in the (8,8) and 64.1% in the (9,9) nanotube, respectively. Our results quantitatively demonstrate less ordered structures for the confined TIP3P model, consistent with the conclusion of Nakamura and Ohno.[129] For the TIP4P/2005 and SPC/E models, local ring structures are confirmed by relatively large percentages of ring-bound molecules. Within the (8,8) nanotube the square configuration is predominant. Interestingly, within the (9,9) nanotube, TIP4P/2005 favors the pentagonal configuration over the hexagonal (49.2% versus 34.9%), while SPC/E is opposite (12.3% versus 72.3%). The configurational preference of the SPC/E model we obtain again coincides with the observations of Nakamura and Ohno.[129]

It is evident that organized stacked ring structures will yield a notably sharp water radial density distribution profile, $\rho(r)$. Density profiles at 300 K are plotted in Figure 3.4. We see that the TIP3P model has the broadest distributions, especially in the (9,9) nanotube, where the non-zero $\rho(r)$ near the central axis clearly reflects the existence of ring-free molecules. For the (8,8) nanotube, TIP4P/2005 water has a taller and narrower distribution curve than SPC/E, which can be explained by its smaller percentage of ring-free molecules (3.1% versus 25.2%). For the (9,9) nanotube, the TIP4P/2005 model favors smaller pentagonal rings rather than hexagon rings in contrast with SPC/E. Therefore, it is reasonable that the distribution

curve of TIP4P/2005 shifts inward, and has a lower peak than SPC/E.

We also considered the number of water molecules, N_{nt}, confined inside CNTs. Model differences are also evident in probability distribution functions, $P(N_{nt})$, as shown in Figure 3.5. First, we considered the (8,8) nanotube. For the SPC/E and TIP3P models, we note that the $P(N_{nt})$ distributions are unimodal, whereas for the TIP4P/2005 model the distribution is bimodal, with quite sharp peaks at 48 and 52 molecules. As 96.7% of the TIP4P/2005 water molecules within the nanotube are in square ring configurations, the two peaks likely correspond to 12 and 13 square rings, respectively, stacked along the nanotube axis. Because the SPC/E model has the largest fraction (72.3%) of hexagonal rings in the (9,9) nanotube, we believe that the peak in $P(N_{nt})$ at 72 molecules comes from the contribution of 12 hexagonal rings. The TIP4P/2005 model has significant numbers of both pentagonal and hexagonal rings (49.2% and 34.9%), as well as ring-free molecules, hence the number distribution for TIP4P/2005 is broad with a major peak at 64 molecules, implying mixed structures, and a minor peak at 72 molecules, which again suggests 12 hexagons. Moreover, inside both nanotubes the TIP3P model generally contains the fewest numbers of molecules, which suggests that TIP3P water is the most loosely packed within the nanotubes.

On account of the distinctive structures observed for the different models, it is interesting to investigate the average number of hydrogen bonds per water molecule (hydrogen bond number) within the nanotubes. Analogous to ice structure inside nanotubes,[58,59] if stacked ring configurations are prevailing, we would expect both intra-ring hydrogen bonds gather molecules together, and inter-ring hydrogen bonds connect neighboring rings. In contrast, if the water molecules are more loosely packed, we would predict on average fewer hydrogen bonds per molecule. The method of determining hydrogen bonds is described in Chapter 2.6.2. The results are listed in Table 3.3 and are in agreement with our expectations. In both nanotubes, TIP3P water has the smallest hydrogen bond numbers, in accord with its having the most substantial fraction of ring-free molecules. TIP4P/2005 water has on average more hydrogen bonds within the (8,8) nanotube than SPC/E (3.28 versus 3.02 per molecule), which can be explained by its higher fraction of ring-bound molecules (96.9% versus 74.8%). In the
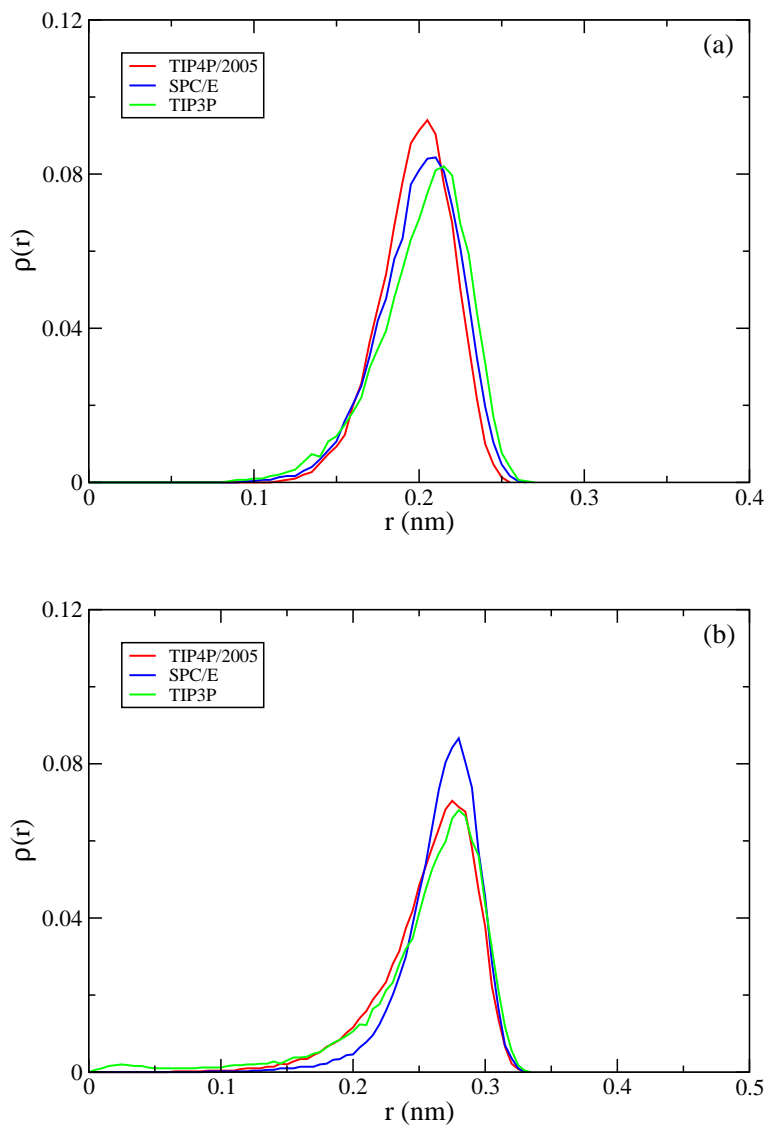
Figure 3.4: Water radial density profiles measured from the nanotube symmetry axes ($r = 0$) at 300 K inside (8,8) [panel (a)] and (9,9) [panel (b)] nanotubes. The water models are indicated in the legends.
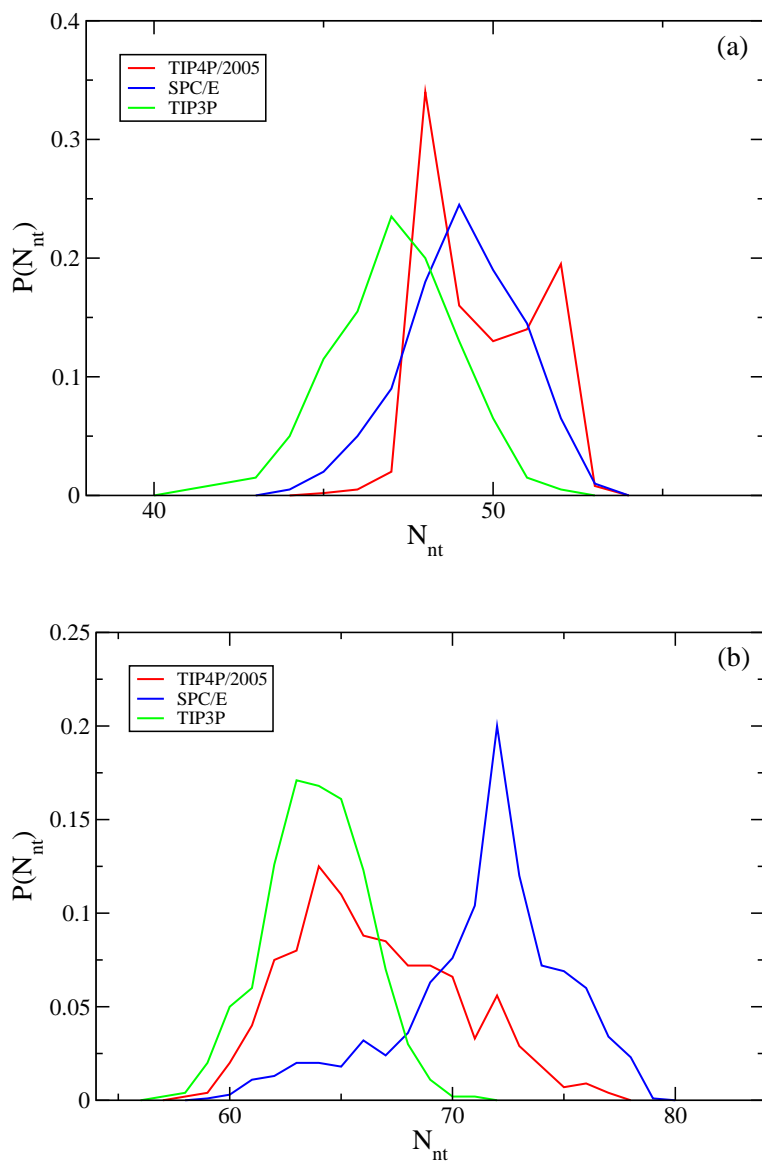
Figure 3.5: Probability distributions for the number of confined water molecules within (8,8) [panel (a)] and (9,9) [panel (b)] nanotubes. The water models are indicated in the legends.

Water model	(8,8) CNT	(9,9) CNT
TIP4P/2005	3.28	3.22
SPC/E	3.02	3.28
TIP3P	2.66	2.75

Table 3.3: Average numbers of hydrogen bonds per water molecule (hydrogen bond numbers) inside the CNTs.

(9,9) nanotube both TIP4P/2005 and SPC/E have the same fraction of ring-free molecules (12.6%), and therefore similar hydrogen bond numbers.

3.4   Water Transport Mechanisms

The results shown in Tables 3.1 and 3.2 indicate a clear correlation between the flow rate and the percent of ring-free molecules. In both nanotubes, TIP3P has the largest faction of ring-free molecules (71.0% and 64.1%) as well as the highest flow rates (287 and 492 ns^{-1}). TIP4P/2005 water has fewer ring-free molecules (3.1%) for the (8,8) nanotube than SPC/E (25.2%) and a slower flow rate (51 versus 111 ns^{-1}). For the (9,9) nanotube TIP4P/2005 and SPC/E have similar flow rates (107 versus 134 ns^{-1}) consistent with identical fractions of ring-free molecules (12.6%). We do note that although the fraction of ring-bound molecules is the same for both these models, the ring configuration distributions differ, indicating differences in the structure of the confined water. However, these structural differences appear to have, if any, a minor effect on the flow rates.

By carefully investigating simulation trajectories of water flow through nanotubes, we can indentify two conduction modes. The first mode is a "cluster-by-cluster" mode, which is best represented by the TIP4P/2005 model. In this mode, water molecules aggregate into clusters (square, pentagonal or hexagonal rings) which move together through the nanotube, one cluster following the other. The cluster-by-cluster mode is depicted by simulation snapshots for TIP4P/2005 water in the (8,8) nanotube in Figure 3.6. From Figure 3.6 we can clearly identify multiple square ring configurations as discussed in Chapter 3.3. We point out that, in this particular example, the highlighted rings existing at $t = 0$ ps remain intact as they travel

through the nanotube. We observe that the ring-bound and ring-free molecules may switch from one type to the other, therefore, rings do not always remain intact, and sometimes clusters do break apart as they flow through the nanotube. Still, this conduction mode is validated by many simulation trajectories, which show a significant amount of cluster motion.

The second mode is a "diffusive" mode, which is the primary mode for the TIP3P model. In this case, there are fewer ring structures (Table 3.2), and those that do occur are fragile and tend to break up during transport, partially because of fewer hydrogen bonds (Table 3.3). Therefore, water molecules pass through the nanotube more independently and freely, rather than as part of a cluster or group. The diffusive mode is illustrated in Figures 3.7 with snapshots from simulations of TIP3P water in the (8,8) nanotube. Here we note that the apparent three square rings present at $t = 0$ completely break apart as they traverse the nanotube. We do not observe TIP3P clusters pass through the entire nanotube intact, suggesting that distinct cluster motion for TIP3P is very rare.

Based on this analysis, we conclude that the formation of relatively stable stacked ring structures for the TIP4P/2005 and SPC/E models leads to flow rates that are much slower than those observed for TIP3P water. The cluster-by-cluster mode requires concerted motion of molecules from several clusters, while the diffusive mode allows individual molecules to move forward without substantial restriction. The different time scales also illustrate the different flow rates of the two conduction modes in Figures 3.6 and 3.7. Of course, both conduction modes can and do happen to some extent for all three models, but TIP4P/2005 and SPC/E favor the slower cluster-by-cluster mode, where molecules are likely to assemble into ring configurations, and TIP3P favors the faster diffusive mode, where there is a higher percentage of ring-free molecules.

It is perhaps worth mentioning that density differences alone can not account for the observed differences in flow rates. This factor is most evident in the (9,9) case, where the most probable nanotube densities are similar for TIP4P/2005 and TIP3P models, as shown in Figure 3.5, which have very different flow rates, and significantly different for TIP4P/2005 and SPC/E models, which have similar flow rates.

(a) $t = 0$ ps

(b) $t = 50$ ps

(c) $t = 100$ ps
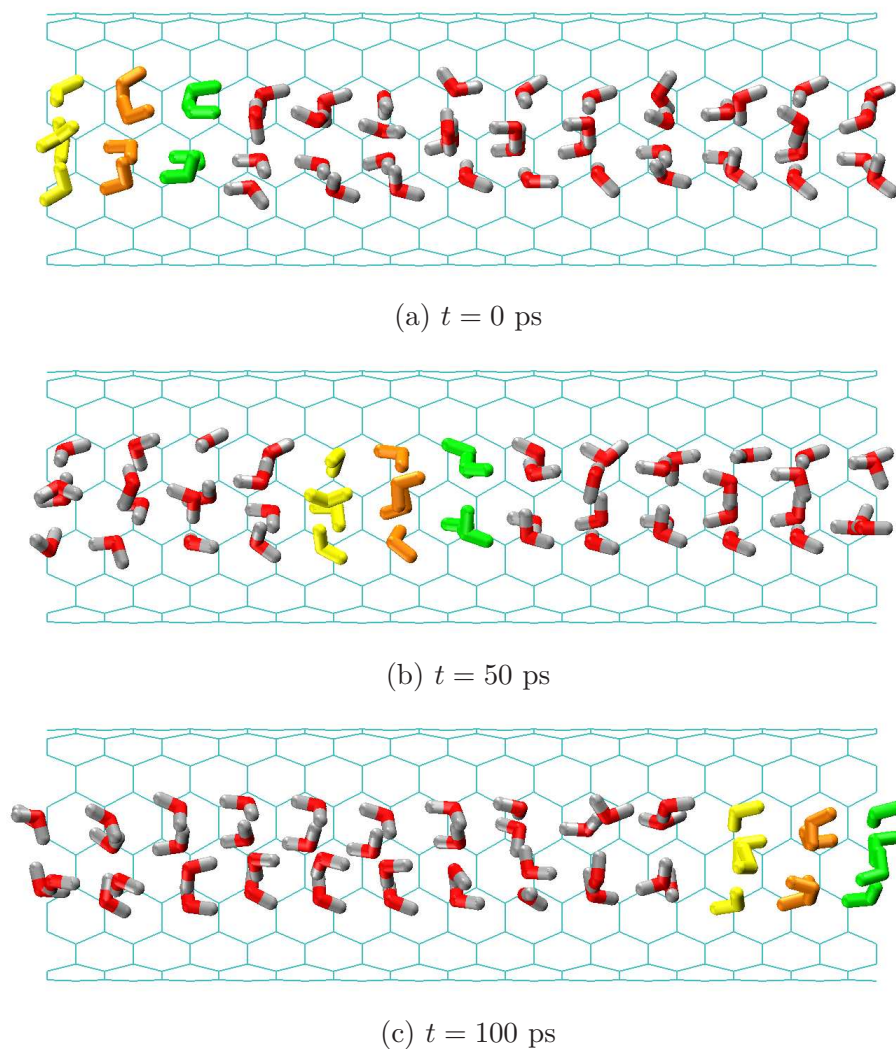
Figure 3.6: Illustrations of the cluster-by-cluster conduction mode for TIP4P/2005 water in the (8,8) nanotube. Carbon atoms are cyan, oxygen atoms are red, and hydrogen atoms are gray, except for three square ring configurations highlighted in yellow, orange, and green. We remark that the highlighted ring structures pass intact across the nanotube. Note that part of the carbon nanotube is not displayed for visual clarity.

(a) $t = 0$ ps

(b) $t = 5$ ps

(c) $t = 10$ ps
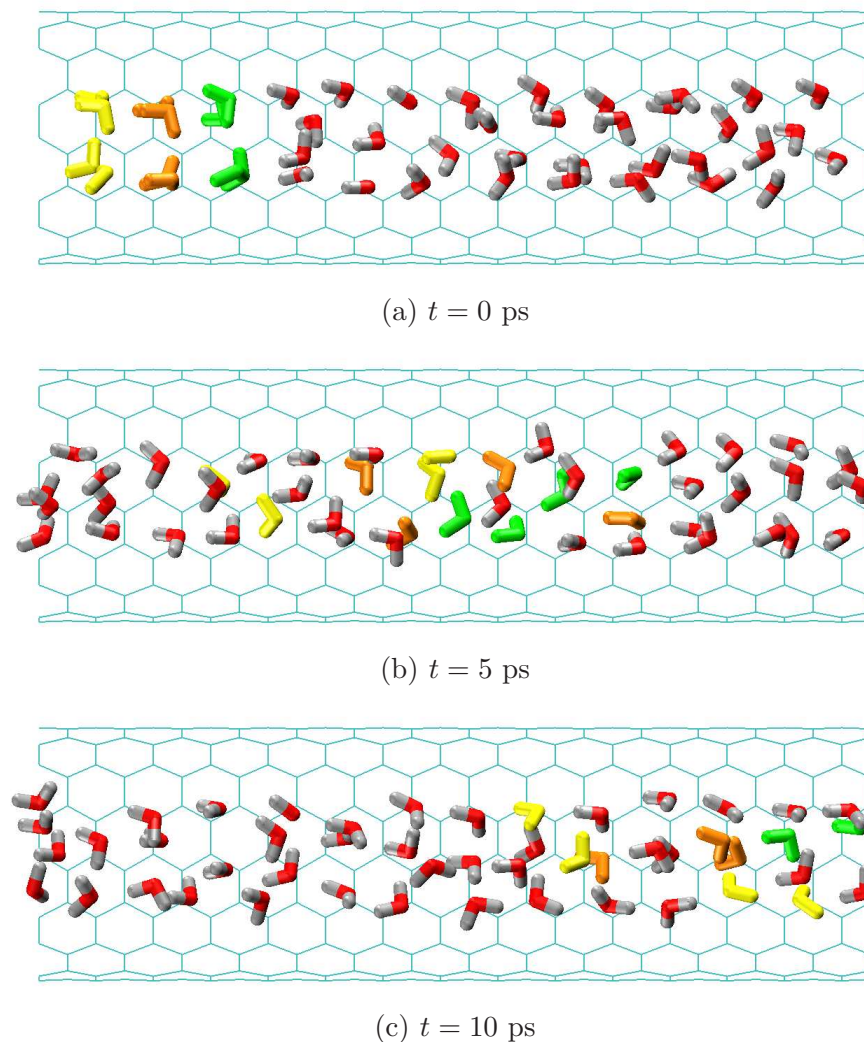
Figure 3.7: Illustrations of the diffusive conduction mode for TIP3P water in the (8,8) nanotube. Carbon atoms are cyan, oxygen atoms are red, and hydrogen atoms are gray, except for three square ring configurations highlighted in yellow, orange, and green. We remark that the highlighted ring structures existing at $t = 0$ ps break up completely as the water molecules pass through the nanotube. Note that part of the carbon nanotube is not displayed for visual clarity.

3.5 Summary

We have investigated pressure-driven water transport through (8,8) and (9,9) CNTs using MD simulations. Among the three water models examined, TIP3P water has the highest transport rates in both nanotubes, which are about five times faster than those of the slowest model, TIP4P/2005. Next, we trace the strikingly different flow rates to the varying amounts of water occurring as ring-bound and ring-free molecules. The TIP4P/2005 model tends to construct stacked ring configurations, giving rise to a cluster-by-cluster conduction mode with many ring clusters traveling as single units through the nanotube. This is also true for the SPC/E model, but to a lesser extent. In contrast, the TIP3P model favors a diffusive conduction mode, where ring structures occur less frequently and are likely to break apart as water passes through the nanotube. The diffusive mode is faster than the cluster-by-cluster mode because water molecules move as individual particles in the diffusive mode rather than as parts of larger molecular groups. Our simulations also support the conjecture of Nakamura and Ohno[129] who suggested that water rings could be regarded as a whole in terms of hydrodynamics.

Chapter 4

How Water Conduction Rates through CNTs Is Related to Bulk Properties for Different Water Models[*]

4.1 Overview

It is interesting to notice that water conduction rates through intermediate-size CNTs are strongly influenced by the water model employed.[148] In Chapter 3 we traced such differences to confined water structures and proposed two distinct transport modes to explain our observations. It is important to emphasize that the results for intermediate-size nanotubes discussed above can not be presumptuously extended to smaller nanotubes. For example, in a (6,6) nanotube, only simple single-file conduction with no complex ring configurations is observed.[47,70,95] However, we show that the flow rate discrepancies for different water models remain in the (6,6) case. By carrying out simulations at various temperatures and carefully analyzing the water dynamics, we show that the discrepancies, in fact, reflect the different mobilities of the bulk liquids. Also, our results are consistent with continuum hydrodynamic analysis. We revisit water flow rates through a (9,9) nanotube. Our work illuminates how flow rates through narrow and intermediate-size nanotubes are related to bulk properties, and

---

[*]A version of this chapter has been published. L. Liu and G. N. Patey, J. Chem. Phys., **144**, 184502 (2016).[149]

can vary significantly for different water models, even when conduction occurs by the same mechanism.

4.2 Water Flow Rates through a (6,6) CNT

In Figure 4.1 we plot typical cumulative counts of water molecules traveling through a (6,6) nanotube as functions of time. Because high pressures are applied in our simulations, molecules pass through the nanotube in a single direction from the high to low pressure reservoir. Here we investigate water dynamics at four different temperatures: 260, 280, 300, and 320 K. As for (8,8) and (9,9) nanotubes, the curves in Figure 4.1 are generally linear against time regardless of the temperature or the water model employed. As long as steady state flows have been established, average flow rates can be easily obtained from linear fits of the cumulative counts curves. It is apparent that the flow rates are not identical for different water models, nor for the same model at different temperatures.

The average flow rate is defined as the average numbers of water molecules traversing either a (6,6) or a (9,9) nanotube during a period of 1 ns. The results of flow rates, along with estimated standard deviations are summarized in Table 4.1 for all three model (note that RC and RP models will be discussed in Chapter 4.4). The table includes flow rates measured at four different temperatures as mentioned above, with the external pressure maintained at 220 MPa. For both sizes of nanotube, the results demonstrate that the water transport rate can be strikingly influenced by the water model employed. If the size of the nanotube and the temperature are fixed, TIP4P/2005 is always the slowest case, and TIP3P is always the fastest. The SPC/E model has intermediate flow rates, but in general, the SPC/E flow rates are closer to those of TIP4P/2005. Moreover, flow rates are positively correlated with temperature for both (6,6) and (9,9) nanotubes. Interestingly, we find that $ln(R_{\text{flow}})$ has a clear linear dependence on T^{-1}, where T is the absolute temperature, indicating that water conduction is an activated process following an Arrhenius type equation
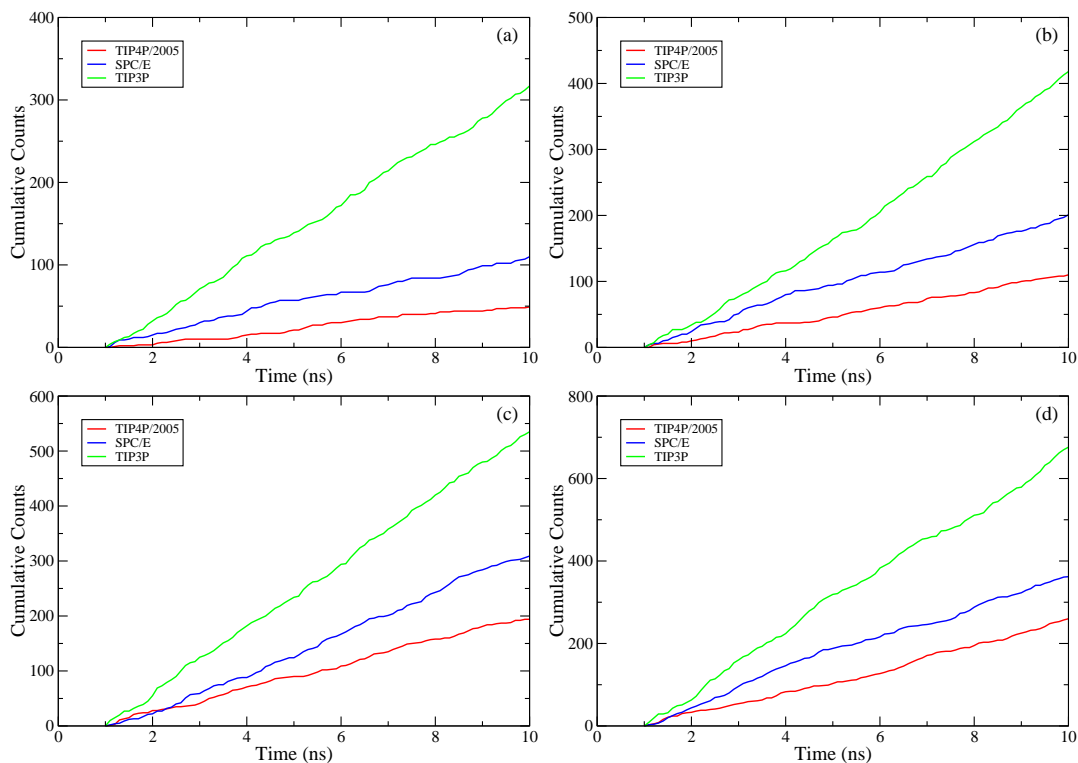
Figure 4.1: Cumulative counts curves showing the number of water molecules that pass through a (9,9) nanotube as functions of time at different temperatures: 260 K (top left), 280 K (top right), 300 K (bottom left), and 320 K (bottom right). Note that counts during first 1 ns are not displayed because this is the equilibration period. The red, blue, and green curves are for the TIP4P/2005, SPC/E, and TIP3P models, respectively.

$$ln(R_{\text{flow}}) = -\frac{E_a}{RT} + C \; , \qquad\qquad (4.1)$$

where E_a is an activation energy, R is the gas constant, and C is effectively constant over the temperature range considered. The calculated activation energies are also listed in Table 4.1. Additionally, for the TIP4P/2005 model we conducted simulations and calculated flow rates with the external pressure fixed at 110 MPa, which is achieved by halving the external force f_{ex} in Equation (2.7). From Table 4.1, we note that the simulated flow rate is roughly proportional to the external pressure, which is consistent with previous simulation results.[140, 150, 151] For the (6,6) nanotube, the activation energies obtained at 220 and 110 MPa agree within the estimated standard deviations, implying that the barrier to flow is not strongly dependent on the driving pressure. For the (9,9) nanotube, the activation energy of TIP4P/2005 at 110 MPa is significantly greater than that at 220 MPa, suggesting that the flow rate influences the barrier.

4.3 Explanation of the Model-dependent Water Transport Rates

In Chapter 3 we discussed why water conduction through (8,8) and (9,9) CNTs is dependent on the water model employed in simulations. Our argument was that the flow rate diversity stems from different ring-like structures formed by the different water models inside the nanotubes. As a consequence, two distinctive conduction modes were proposed to explain the different flow rates. However, in the (6,6) nanotube, the spatial restriction is such that each water molecule can have at most two near neighbors, which results in the formation of a single hydrogen-bonded chain. A snapshot of a typical molecular chain is shown in Figure 4.2. The single hydrogen-bonded chain structure is a common feature of all three water models in the (6,6) nanotube and gives rise to a so-called single-file conduction mode.[47, 70, 95] This basic structural feature and conduction mode are present at all temperatures considered. Therefore, unlike (8,8) and (9,9) cases, it is not possible to simply explain the different conduction rates

Pressure (MPa)	Water model	Temperature				Activation energy (kJ mol^{-1})
		260 K	280 K	300 K	320 K	
	Flow rates through a (6,6) CNT (ns^{-1})					
	TIP4P/2005	6 (1)	12 (1)	22 (3)	28 (2)	18.2 (2.0)
	SPC/E	12 (1)	21 (2)	34 (2)	42 (3)	14.8 (1.2)
220	TIP3P	37 (3)	48 (2)	59 (2)	75 (3)	8.0 (1.0)
	RC	22 (1)	34 (1)	47 (2)	61 (3)	11.8 (0.7)
	RP	7 (1)	14 (1)	22 (2)	32 (2)	17.4 (1.7)
110	TIP4P/2005	3 (1)	7 (2)	11 (1)	16 (3)	19.1 (4.2)
	Entry rates into a (6,6) CNT (ns^{-1})					
	TIP4P/2005	10 (1)	19 (1)	30 (3)	44 (1)	17.0 (1.2)
	SPC/E	18 (1)	30 (2)	45 (3)	59 (2)	13.8 (0.8)
220	TIP3P	46 (2)	62 (3)	75 (2)	95 (2)	8.2 (0.5)
	RC	27 (2)	43 (1)	59 (2)	77 (4)	12.0 (1.0)
	RP	10 (1)	20 (1)	31 (1)	44 (2)	17.0 (1.2)
110	TIP4P/2005	7 (1)	14 (2)	22 (2)	33 (1)	17.7 (2.8)
	Flow rates through a (9,9) CNT (ns^{-1})					
	TIP4P/2005	16 (4)	44 (4)	107 (6)	223 (7)	30.5 (2.7)
220	SPC/E	31 (5)	67 (7)	134 (14)	292 (10)	25.6 (1.9)
	TIP3P	175 (10)	356 (6)	492 (15)	606 (11)	14.2 (0.7)
110	TIP4P/2005	4 (2)	18 (4)	52 (5)	106 (3)	37.9 (5.5)
	Entry rates into a (9,9) CNT (ns^{-1})					
	TIP4P/2005	47 (6)	87 (4)	157 (7)	287 (7)	20.8 (1.4)
220	SPC/E	66 (6)	108 (5)	187 (20)	359 (10)	19.3 (1.1)
	TIP3P	226 (11)	412 (6)	552 (10)	669 (8)	12.4 (0.5)
110	TIP4P/2005	37 (8)	55 (5)	110 (9)	198 (3)	19.6 (2.4)

Table 4.1: Summary of flow rates, entry rates, and their calculated activation energies for different water models. The numbers in brackets are estimated standard deviations.
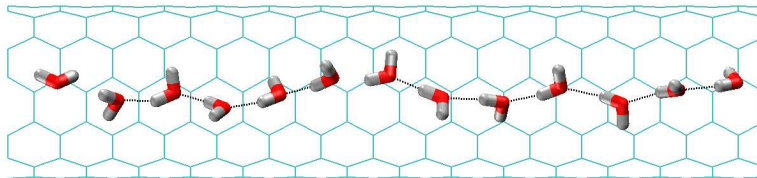
Figure 4.2: A configurational snapshot of TIP4P/2005 water in the (6,6) nanotube. Carbon atoms are cyan, oxygen atoms are red, and hydrogen atoms are gray. The black dotted lines indicate hydrogen bonds. Note that part of carbon nanotube is not displayed for visual clarity.

by invoking obvious structural differences within the (6,6) nanotube.

To explain the mechanism of the model-dependent conduction and activation energy observed in the (6,6) case, we quantitatively examined properties of confined water that could account for such differences. In particular, we calculated the average number of hydrogen bonds per water molecule, and the radial pressure exerted on the nanotube wall.

Hydrogen bonds are defined using geometric criteria as described in Chapter 2.6.2, and for different models and temperatures, the average numbers of hydrogen bonds per water molecule (hydrogen bond numbers) are tabulated in Table 4.2. The hydrogen bond number decreases with increasing temperature for all water models, implying that the chain structure becomes less rigid at higher temperatures. TIP3P has notably smaller hydrogen bond numbers than the other two models, which suggests that the degree of hydrogen bonding might be an aspect influencing the conduction rate. The TIP4P/2005 and SPC/E models have approximately identical hydrogen bond numbers at all temperatures simulated, yet at 260 K, TIP4P/2005 has half as many conduction counts as SPC/E (6 versus 12 ns^{-1}), and the TIP4P/2005 counts remain significantly smaller at higher temperatures. For this reason, the hydrogen bond number does not appear to determine the flow rate directly. From Table 4.2, we can also conclude that the hydrogen bond number is in general independent of the magnitude of the external pressure.

The pressure in the radial direction implicitly depends on water structural properties within a CNT.[152,153] One would expect the radial pressure to influence the "friction" with

Pressure (MPa)	Water model	Temperature			
		260 K	280 K	300 K	320 K
	Hydrogen bond number				
	TIP4P/2005	1.79	1.75	1.72	1.70
	SPC/E	1.78	1.76	1.73	1.71
220	TIP3P	1.65	1.62	1.59	1.55
	RC	1.73	1.70	1.66	1.62
	RP	1.77	1.75	1.72	1.68
110	TIP4P/2005	1.79	1.75	1.72	1.69

Table 4.2: Average numbers of hydrogen bonds per water molecule (hydrogen bond numbers) within the (6,6) nanotube for different water models.

the nanotube wall and hence possibly affect the flow rate. We estimated the radial pressure, P_{radial}, assuming that the equilibrium expression[153]

$$
\begin{aligned}
P_{\text{radial}} = \frac{k_B T \langle N_{\text{nt}} \rangle}{V_{nt}} + \frac{1}{2V_{nt}} \Bigg[\Bigg\langle \sum_i \sum_{j>i} f_{ij}^{(x)} x_{ij} \Bigg\rangle \\
+ \Bigg\langle \sum_i \sum_{j>i} f_{ij}^{(y)} y_{ij} \Bigg\rangle + \Bigg\langle \sum_i f_{\text{nanotube}}^{(i)} (r_{\text{eff}} - r_i) \Bigg\rangle \Bigg]
\end{aligned}
\tag{4.2}
$$

holds, where k_B is the Boltzmann constant, T is the absolute temperature, $\langle N_{\text{nt}} \rangle$ is the average number of water molecules within the nanotube, V is the volume of nanotube cavity, $f_{ij}^{(k)}$ is the k component of the force exerted by particle j on particle i, k_{ij} is the k component of the vector from j to i, $f_{\text{nanotube}}^{(i)}$ is the force exerted by particle i on the nanotube wall, r_{eff} is the effective radius of the nanotube, and r_i is the distance of particle i from the symmetry axis of the nanotube.

The calculated radial pressures are listed in Table 4.3. The pressure magnitudes are large and consistent with earlier equilibrium calculations.[153] Given that for the TIP4P/2005 model the radial pressure obtained does not have a strong dependence on the flow rate, the equilibrium assumption mentioned above appears reasonable. Also, the pressure exerted on

Pressure (MPa)	Water model	Temperature			
		260 K	280 K	300 K	320 K
		Radial pressure (MPa)			
	TIP4P/2005	205 (7)	208 (4)	216 (6)	227 (12)
	SPC/E	208 (5)	216 (3)	222 (4)	229 (7)
220	TIP3P	179 (6)	190 (6)	199 (6)	204 (4)
	RC	202 (4)	205 (9)	217 (9)	224 (11)
	RP	213 (10)	216 (7)	226 (13)	237 (14)
110	TIP4P/2005	208 (6)	218 (8)	228 (9)	233 (4)

Table 4.3: Radial pressures exerted on the (6,6) nanotube by different water models. The numbers in brackets are estimated standard deviations.

the nanotube wall increases with increasing temperature as expected. We note that the largest contribution to the radial pressure ($\sim$75%) comes from the LJ part of the water-nanotube interaction. The TIP3P radial pressures are obviously lower than those for TIP4P/2005 and SPC/E, possibly accounting for some of the faster flow rates. However, the radial pressures are similar between TIP4P/2005 and SPC/E, with the SPC/E values even slightly larger. Thus the radial pressure can not account for why SPC/E has faster flow rates than TIP4P/2005.

4.4 Water Hydrodynamics and Bulk Fluid Properties

Failing to find a satisfactory explanation for the different flow rates considering only water properties within the (6,6) CNT, we asked whether the entry of water molecules into the nanotube might be an important model-dependent factor. One will guess that the different water model employed determines the entry rate of water molecules if the radius of the nanotube is fixed. To investigate this idea we calculated water entry rates, R_{entry}, for different water models. The method for calculating the entry rate is described in Chapter 2.6.1. The entry rates are tabulated in Table 4.1. We see that for both (6,6) and (9,9) nanotubes, the entry rates for the three water models differ just as the flow rates do, with TIP3P being the fastest and TIP4P/2005 the slowest. Also, the entry rate becomes higher as the simulation temperature

rises. Unlike the flow rate, which is generally proportional to the external pressure difference, the entry rate decreases to a lesser extent (only 30% change on average) when the external pressure difference drops from 220 to 110 MPa.

Moreover, we find that the temperature dependence of not only the flow rate but also of the entry rate follows an Arrhenius-like equation. Arrhenius plots for $ln(R_{\text{flow}})$ and $ln(R_{\text{entry}})$ are shown in Figures 4.3 and 4.4, respectively. We can draw several interesting conclusions from the estimated activation energies. For the (6,6) nanotube, the TIP4P/2005 model has largest activation energies for both flow and entry rates while the TIP3P model has the smallest activation energies. The same trends are also apparent in the case of the (9,9) nanotube. Most interestingly, in the (6,6) nanotube the activation energies associated with flow and entry agree within the standard deviations, regardless of the external pressure difference used in simulations. However, in the (9,9) nanotube the activation energy similarity is not true, particularly for TIP4P/2005 and SPC/E, where the flow activation energies are notably higher than the entry values.

Based on the results in Table 4.1, we hypothesize that for the (6,6) case the different flow rates primarily come from different entry rates, and, therefore, the flow activation energy is essentially the corresponding entry activation energy. For the (9,9) case, this observation is not correct. In Chapter 3, we showed that TIP4P/2005 and SPC/E are more likely to form polygonal ring structures within the (9,9) CNT, in contrast with the TIP3P model. A useful graphical illustration is given in Figure 4.5, where we plot the rate ratios $R_{\text{flow}}/R_{\text{entry}}$ as functions of temperature. We note that for the (6,6) nanotube, this ratio is approximately constant within the temperature range investigated, which is consistent with nearly equal flow and entry activation energies. Whereas for the (9,9) nanotube, the ratios for all three models are dependent on temperature to a certain extend, as might be expected if the flow and entry activation energies are different. Note that the profiles of TIP4P/2005 and SPC/E show strong temperature dependence, while the profile of TIP3P only shows slight dependence.

To identify the origin of the energy barrier to entry, we calculated the average potential energy of water (including both water-water and water-nanotube interactions) as a function
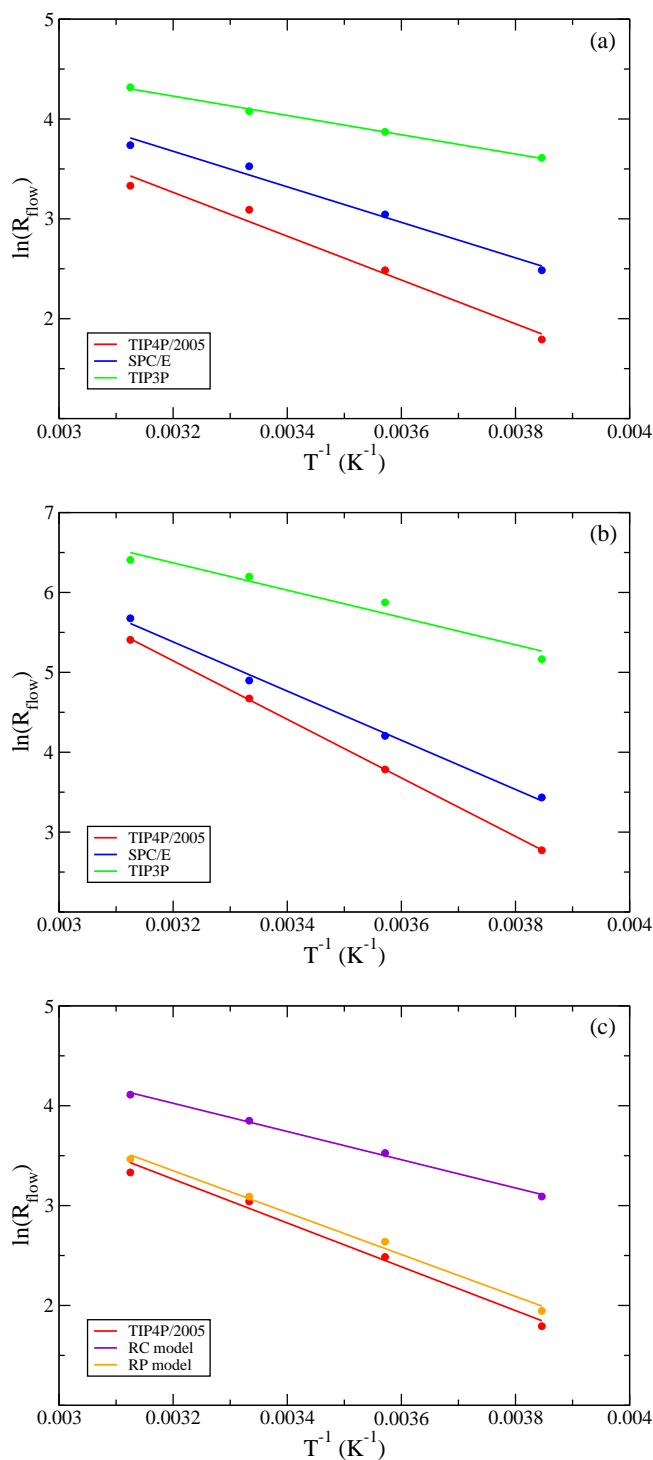
Figure 4.3: The dependence of $ln(R_{\text{flow}})$ on T^{-1}. Results for the (6,6) nanotube [panels (a) and (c)], and for the (9,9) nanotube [panel (b)] are shown. The water models are indicated in the legends. Note that RC and RP refer to modified TIP4P/2005 models as described in the text.
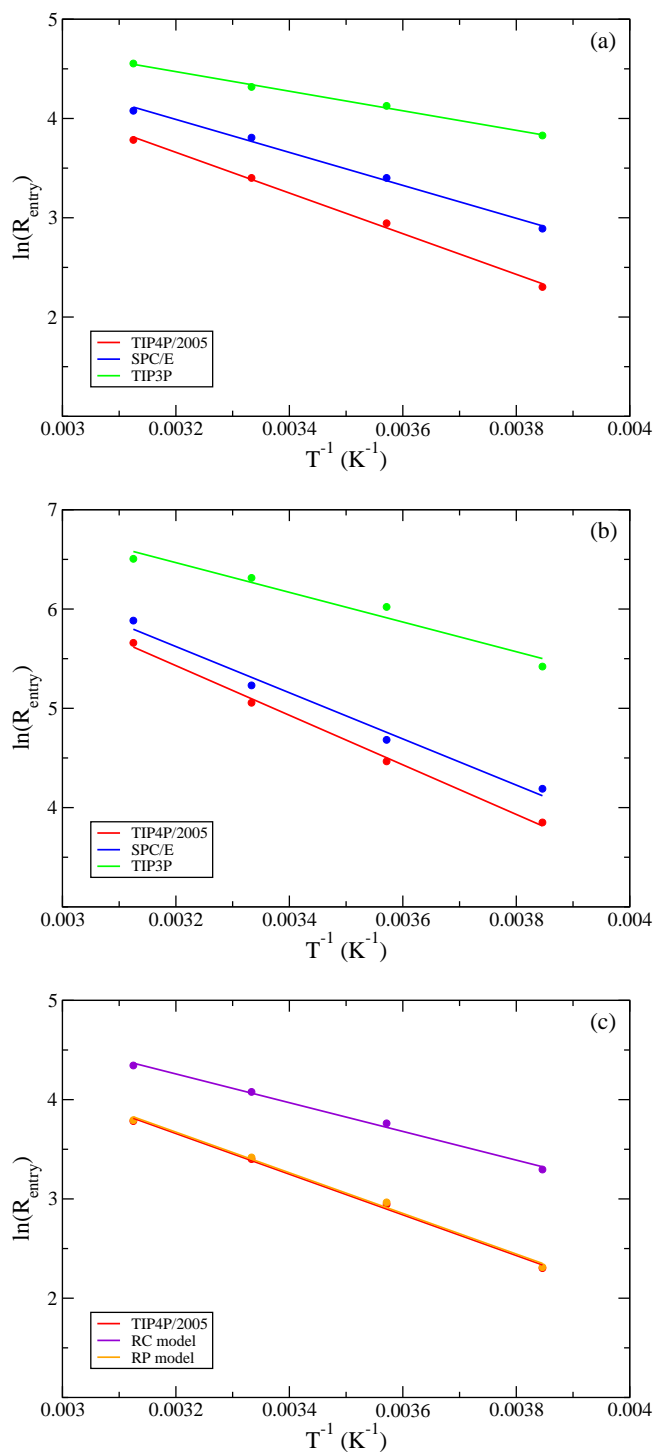
Figure 4.4: The dependence of $ln(R_{\text{entry}})$ on T^{-1}. Results for the (6,6) nanotube [panels (a) and (c)], and for the (9,9) nanotube [panel (b)] are shown. The water models are indicated in the legends. Note that RC and RP refer to modified TIP4P/2005 models as described in the text.
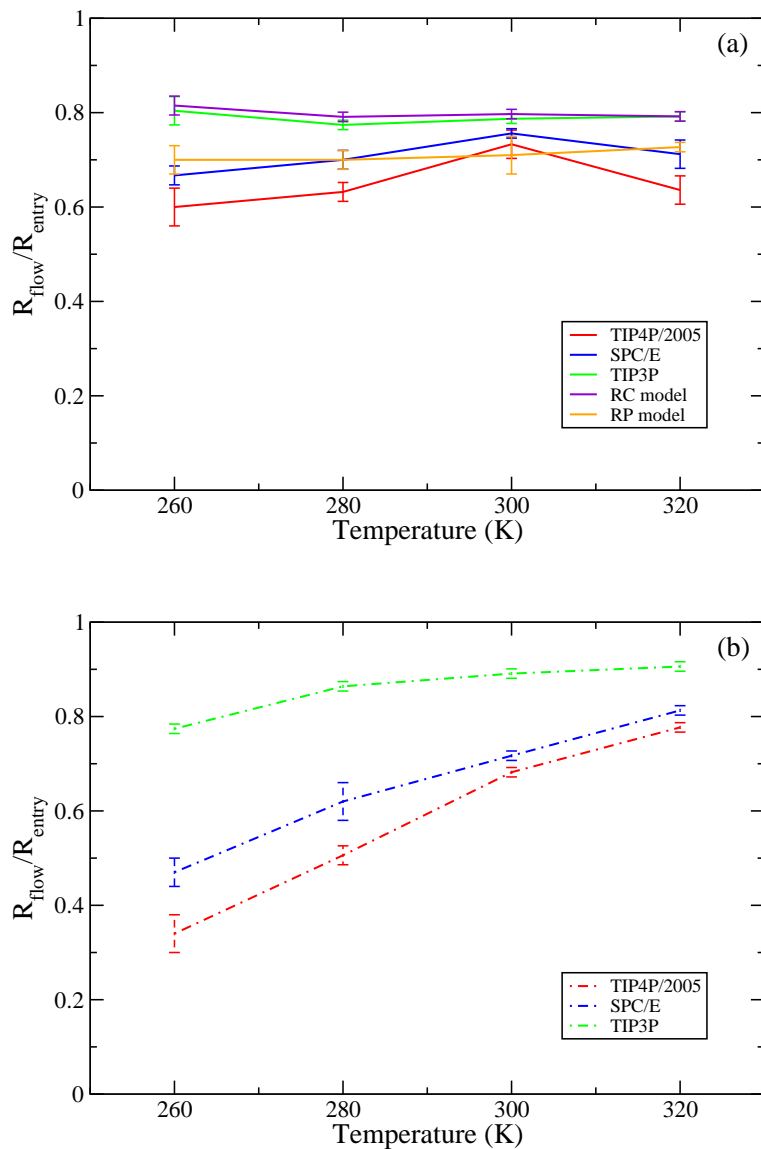
Figure 4.5: Temperature dependence of the ratio $R_{\mathrm{flow}}/R_{\mathrm{entry}}$ for the (6,6) [panel (a)] and (9,9) [panel (b)] nanotubes. The water models are indicated in the legends. Note that RC and RP refer to modified TIP4P/2005 models as described in the text.

of position along the z coordinate. Consider a cylinder centered on the symmetry axis of the (6,6) CNT, whose radius is equal to that of the nanotube, and which includes both the nanotube cavity and an extended region into the bulk. The cylinder is divided into bins each 0.2 nm wide. Using equilibrium NVT simulations at 300 K, the average potential energy is determined for every bin. Corresponding potentials of mean force (PMF) for water along the z coordinate are also obtained as described in Chapter 2.6.4. Both thermodynamic profiles are obtained using five independent simulations each 100 ns long. The potential energy and the PMF curves for all three water models are shown in Figures 4.6 and 4.7, respectively.

We note that as a water molecule enters the nanotube, its interaction with other water molecules decreases, but water-nanotube interactions can at least partially compensate such effect. From Figure 4.6 we note that the TIP3P model has almost no energy barrier to entry. The energy difference for TIP3P, defined as $\Delta U = U_{\text{CNT}} - U_{\text{bulk}}$, is ~ -6.2 kJ mol^{-1}. This observation agrees well with the result (~ -5.8 kJ mol^{-1}) obtained by Waghe *et al.*[53] for TIP3P water and a completely submerged (6,6) nanotube of similar length. The TIP4P/2005 and SPC/E models have small energy barriers to entry ($\sim$2.9 and $\sim$0.9 kJ mol^{-1}). However, these values are not sufficient to account for the activation energies of R_{entry} ($\sim$17.0 and $\sim$13.8 kJ mol^{-1}) even if we consider the substantial uncertainties at the nanotube orifice.

The PMF profiles for all three water models shown in Figure 4.7 are qualitatively similar. However, the TIP4P/2005 and SPC/E models have considerable oscillation along the (6,6) nanotube symmetry axis, which we believe comes from increased hydrogen bonding within the nanotube (Table 4.2). The free energy barrier to entry for TIP3P we obtained ($\sim$2.6 kJ mol^{-1}) is close to the value ($\sim$2.1 kJ mol^{-1}) reported by Corry.[95] The free energy barriers are larger ($\sim$3.0 kJ mol^{-1}) for the TIP4P/2005 and SPC/E models, but again these energies are too small to justify the observed differences in entry rate satisfactorily.

Since both equilibrium potential energy and potential of mean force profiles fail to explain the apparent barriers to entry, we focus our attention on another factor, the bulk diffusivity for different water models. The method of determining self-diffusion coefficients has been described in Chapter 2.6.3. The diffusion coefficients, which agree well with literature values,[132]
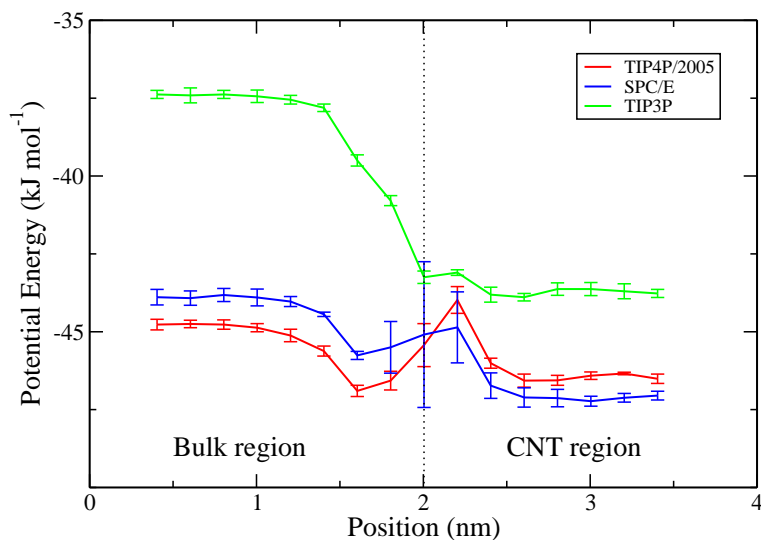
Figure 4.6: Water potential energy profiles along the nanotube axis as described in the text. The water models are indicated in the legends. The error bars represent one standard deviation. The black vertical dotted line indicates the position of the (6,6) nanotube orifice.
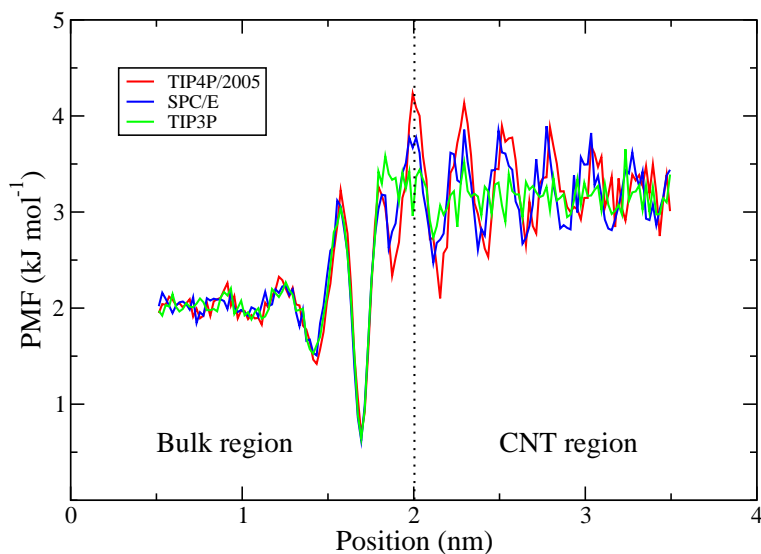
Figure 4.7: Water potential of mean force profiles along the nanotube axis as described in the text. The water models are indicated in the legends. The black vertical dotted line indicates the position of the (6,6) nanotube orifice.
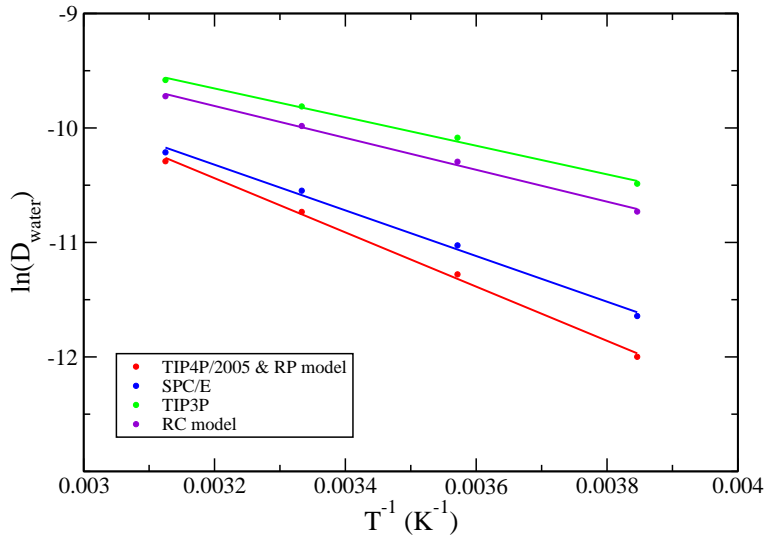
Figure 4.8: The dependence of $ln(D_{\text{water}})$ on T^{-1}. Self-diffusion coefficients are in cm^2 s^{-1}. The water models are indicated in the legends.

together with the associated activation energies are presented in Table 4.4. Arrhenius plots for the bulk diffusion coefficients are given in Figure 4.8. It is interesting to observe that the activation energies of diffusion coincide in magnitude with those estimated from entry rates for all three water models, and display the same trend. TIP3P gives the lowest activation energy of diffusion ($\sim$10.4 kJ mol^{-1}), and TIP4P/2005 has the highest ($\sim$19.6 kJ mol^{-1}). Although the activation energies obtained from entry rates and self-diffusion coefficients are not exactly equal, they suggest that the entry rates are closely related to bulk fluid dynamics. Hence, even for single file conduction, different water models can feature different flow rates related to their different bulk mobilities. In the (6,6) nanotube case, the bulk diffusivity appears to be much more important than any other factor in determining the flow rate. We suppose that we should take such factor into account in interpreting different flow rates obtained from different water models, and when attempting to compare simulation results with those of real water.

Several papers[142, 154–156] have discussed entrance effect on nanotube flow rates. Most interestingly, Gravelle *et al.*[156] demonstrated good agreement between MD simulation results and continuum hydrodynamics even for a nanotube undergoing single-file water conduction.

Water model	Temperature				Activation Energy (kJ mol^{-1})
	260 K	280 K	300 K	320 K	
Self-diffusion coefficient (10^{-5} cm^{2}s^{-1})					
TIP4P/2005 and RP	0.62 (0.03)	1.26 (0.02)	2.18 (0.10)	3.39 (0.04)	19.6 (0.6)
SPC/E	0.88 (0.04)	1.63 (0.06)	2.62 (0.12)	3.67 (0.09)	16.5 (0.6)
TIP3P	2.79 (0.07)	4.17 (0.07)	5.48 (0.25)	6.90 (0.06)	10.4 (0.3)
RC	2.19 (0.07)	3.38 (0.09)	4.62 (0.21)	5.99 (0.29)	11.6 (0.6)

Table 4.4: Water self-diffusion coefficients and their calculated activation energies for different water model. The numbers in brackets are estimated standard deviations.

Therefore it is interesting to examine our data given continuum hydrodynamics.

Sampson[157] considered liquid flowing through a circular hole in an infinitely thin membrane and proposed the relationship

$$R = \frac{\Delta P r_{\text{eff}}^3}{3\eta} \ ,$$
(4.3)

where R is either the fluid flow rate or entry rate, ΔP is the pressure difference, r_{eff} is the effective radius of the hole, and η is the fluid shear viscosity. Note that in this case, the flow and entry rates are equivalent. Gravelle *et al.*[156] even considered the hydrodynamic resistance of a cylindrical pore. They concluded that the rates are inversely proportional to the shear viscosity. Also, using the criteria proposed by Gravelle *et al.*,[156] the resistance of the nanotube in our specific case is negligible, therefore, Equation (4.3) remains valid. The Stokes-Einstein equation gives the connection between the diffusion coefficient, D_{water}, and the shear viscosity η

$$D_{\text{water}} = \frac{k_B T}{6\pi \eta R_{\text{Stokes}}} \ ,$$
(4.4)

where R_{Stokes} is the Stokes radius (of water). From Equations (4.3) and (4.4), we easily obtain

$$\frac{RT}{D_{\text{water}}} = \frac{2\pi r_{\text{eff}}^3 R_{\text{Stokes}}}{k_B \Delta P} \ .$$
(4.5)

Water model	σ_{O-C} (nm)	ε_{O-C} (kJ mol^{-1})	q_H (e)	q_O (e)	q_M (e)
TIP4P/2005	3.2793	0.5280	+0.5564	0	−1.1128
RC	3.2793	0.5280	+0.5286	0	−1.0572
RP	3.2793	0.5016	+0.5564	0	−1.1128

Table 4.5: Force field parameters of the original TIP4P/2005, along with the modified RC and RP models.

Thus, assuming that the R_{Stokes} is approximately the same for the different water models, the left-hand side, RT/D_{water}, should be constant regardless of the water model employed in MD simulations.

We plot the ratios $R_{\text{flow}}T/D_{\text{water}}$ and $R_{\text{entry}}T/D_{\text{water}}$ (in arbitrary units) against temperature in Figure 4.9. It is apparent that for both (6,6) and (9,9) CNTs the $R_{\text{entry}}T/D_{\text{water}}$, although slight differences amongst the models exist, remains nearly constant as the temperature varies for all models considered, which indicates that the entry rates are primarily determined by the hydrodynamics of the bulk liquid. For the (6,6) nanotube, $R_{\text{flow}}T/D_{\text{water}}$ behaves much like $R_{\text{entry}}T/D_{\text{water}}$ for all models, which is consistent with our conclusion that the entry rate largely decides the flow rate in this case. For the (9,9) nanotube, $R_{\text{flow}}T/D_{\text{water}}$ behaves as $R_{\text{entry}}T/D_{\text{water}}$ only for the TIP3P model. For the TIP4P/2005 and SPC/E models, $R_{\text{flow}}T/D_{\text{water}}$ differs with temperature and displays model dependence, which is again consistent with our observation that water structures within the (9,9) nanotube have a strong influence on the flow rate.

To further test the relationship between the flow rate and the bulk mobility, we conducted simulations for two modified versions of the TIP4P/2005 model. In one modified model (denoted as RC), all charges in TIP4P/2005 water are reduced by 5%. In the other model (denoted as RP), the oxygen-carbon LJ energy parameter (ε_{O-C}) is reduced by 5%. Note that in the RP model, only the water-nanotube interactions are altered, and the water-water interactions remain unchanged. The relevant force field parameters of the original TIP4P/2005, RC, and RP models are given in Table 4.5.
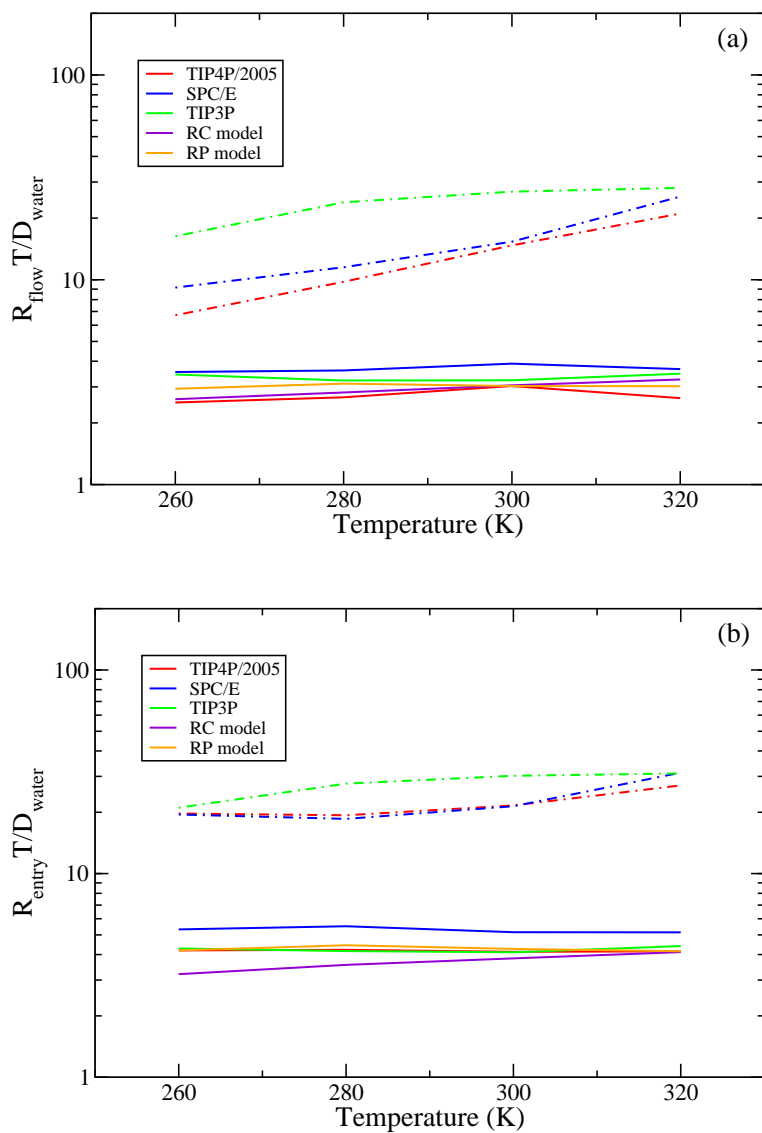
Figure 4.9: Temperature dependence of the ratio $R_{\text{flow}}T/D_{\text{water}}$ [panel (a)] and $R_{\text{entry}}T/D_{\text{water}}$ [panel (b)] in arbitrary units. Results for the (6,6) and (9,9) nanotubes are plotted as solid and dashed-dotted lines. The water models are indicated in the legends. Note that a logarithmic scale is used on the vertical axis.

Results and analysis for the RC and RP models are included in Tables 4.1, 4.2, 4.3, 4.4, and in Figures 4.3, 4.4, 4.5, 4.8, 4.9. We observe that the RC model has faster flow and entry rates than those of the original TIP4P/2005 model, with correspondingly lower activation energies. Besides, by reducing the partial charges on interaction sites and therefore weakening the overall water-water interactions, the bulk self-diffusion coefficients of RC are greater than that of TIP4P/2005. Moreover, the associated activation energy of RC is lower. Generally speaking, the results of the RC model are quite analogous to those of TIP3P, supporting our view that bulk transport essentially explains the different flow rates through the (6,6) CNT. Also, we see that the flow and entry rates of the RP model are almost identical to corresponding rates of unmodified TIP4P/2005, even though the RP water interacts more weakly with carbon atoms. This is also true of the activation energies. We remark that our flow rate results agree with a previous study[85] which mainly discussed the influence of the water-nanotube interaction on the flow rate. Finally, although there are substantial differences in the flow and entry rates between the two modified models, we see from Figure 4.9 that the results again reasonably match the continuum hydrodynamic predictions.

By investigating the dynamics of the two modified models, we demonstrate that the bulk fluid properties have a much greater impact on the water flow rate through the (6,6) nanotube than details of the water-nanotube interaction.

4.5 Summary

In this chapter, we have shown that water conduction rates through a (6,6) CNT are dependent on the water model employed in MD simulations. This observation is consistent with our earlier results for (8,8) and (9,9) nanotubes described in Chapter 3. However, unlike intermediate-size nanotubes in which confined water has special structures that influence conduction rates, in the (6,6) nanotube all three models examined have similar single-string configurations.

We show that neither the different water structures within a (6,6) nanotube nor different

water-carbon interactions can account for the model dependence of the flow rate. We discover that both the water flow rate through and the entry rate into the (6,6) nanotube are activated processes. Moreover, the temperature dependences of both rates are well described by an Arrhenius-like equation. Based on estimated activation energies, we reason that the flow rates are closely related to the entry rates, which in turn are strongly influenced by the bulk mobilities of the different water models. Continuum hydrodynamics calculations, as well as MD simulation results employing modified water models, support this conclusion.

Our results unequivocally demonstrate that the water flow rate through even a (6,6) nanotube can be strikingly model dependent. We trace this somewhat unexpected observation to the different diffusion abilities of bulk water. Given the present observations, it would be desirable to select a water model such as TIP4P/2005, which has a self-diffusion coefficient close to that of real water, when attempting to simulate water transport through CNTs or other nanoscopic channels.

Chapter 5

How Different Water Models Affect Simulated Ion Transport Rates through a (9,9) CNT*

5.1 Overview

In previous chapters, we showed that different water models can have strikingly different flow rates through CNTs. To be more specific, for intermediate-size nanotubes such as the (9,9) nanotube, not only the bulk mobility but also the structure of water confined within the nanotube determines the flow rate. In this chapter, we consider NaCl solutions with concentrations varying from $\sim$0.25 to $\sim$2.8 mol L^{-1} and investigate water and ion conduction through a finite-length (9,9) nanotube. We observe that water and ion flow rates still differ sharply for the TIP4P/2005 and TIP3P models. We note that the flow rate dependence on temperature fits an Arrhenius-type equation. Also, for the TIP3P model, simulated water transport rates in solution agree well with expectations based on continuum hydrodynamics. Most importantly, we confirm that both factors, bulk fluid diffusivity and confined molecular structure, again can account for ion transport differences between models. Our results demonstrate that ion conduction through nanotubes is sensitive to factors other than ion itself, in particular, the structure of the confined water molecules.

---

*A version of this chapter has been published. L. Liu and G. N. Patey, J. Chem. Phys., **146**, 074502 (2017).[158]

5.2 Water and Ion Flow Rates through a (9,9) CNT

Here we focus on only two water models: TIP4P/2005 and TIP3P. In Chapters 3 and 4 we showed that these two models have the most significant differences. Although the TIP4P/2005 model has been rarely studied in simulations of water transport, it is probably the most realistic rigid water model available.[132] The TIP3P model, which has less accurate bulk transport properties, has been more widely used in water transport studies.[88, 90, 95, 107, 111, 151, 159]

In Figure 5.1 we plot typical cumulative counts for water molecules and ions in NaCl solution passing through a (9,9) nanotube as functions of time. The results shown are for a 1 mol L^{-1} solution at 320 K, and we note that the counts curves are generally linear against time for both water models, and at all solution concentrations and temperatures. Note that for ions, especially the TIP4P/2005 solution, the flow is rather slow resulting in jagged curves, nevertheless, an increasing trend is clear with essentially a constant rate. The average flow rates, R_{flow}, for both water and ions can be estimated by linearly fitting the cumulative counts curves after a steady state is completely established. These rates, as well as standard deviations, are tabulated in Table 5.1.

We first considered water flow rates. We see immediately from Table 5.1 that the water flow rate significantly depends on the water model employed, with TIP3P having much faster flow rates than TIP4P/2005 at the same temperature and salt concentration. This is especially true at the lower temperatures. With increasing temperature, faster water flow rates are observed for both models. This observation is not surprising given our earlier discussions in Chapters 3 and 4, showing that both the fluid viscosity and water structure inside the nanotube can play important roles in determining water conduction. Moreover, the water flow rate generally decreases with ion concentration by much more than the small decrease in the number of water molecules in the MD simulations. We believe that the decrease can be at least partially explained by the decreasing diffusion coefficients of bulk water with increasing salt concentration. For example, at 300 K the diffusion coefficients of TIP4P/2005 water are 2.18×10^{-5}, 2.05×10^{-5}, 1.73×10^{-5}, and 1.10×10^{-5} cm^2 s^{-1}, for pure water and NaCl solutions
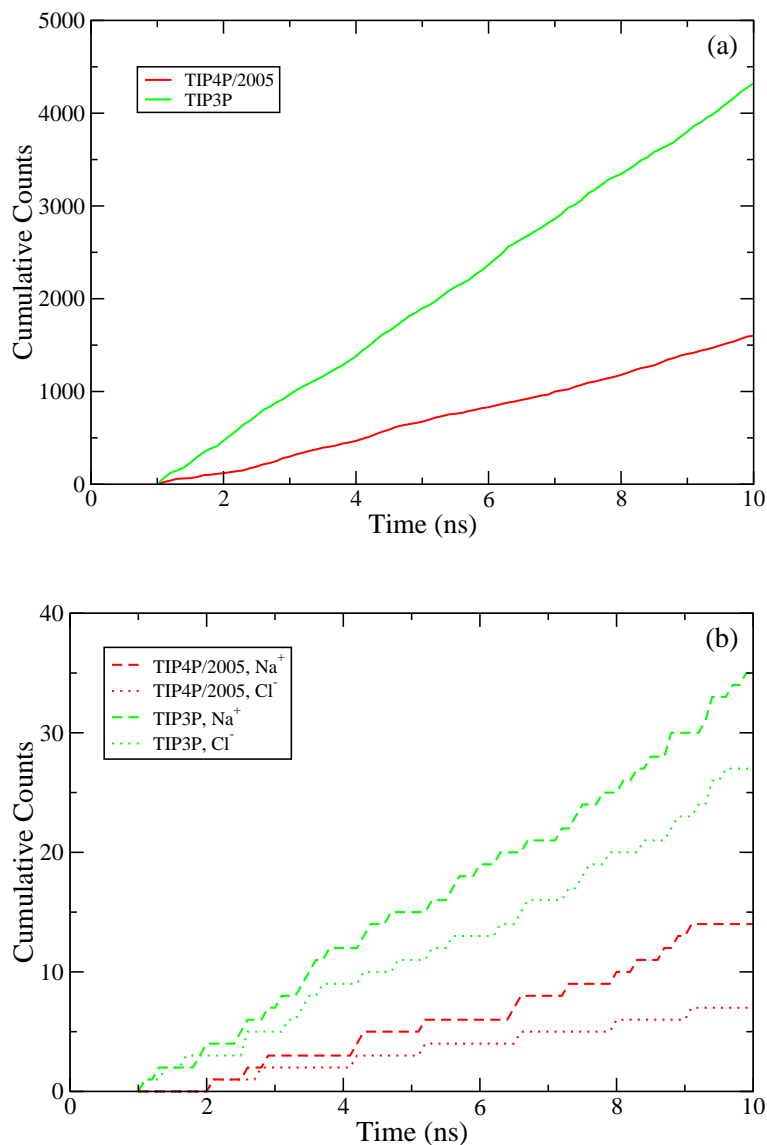
Figure 5.1: Cumulative counts curves showing the number of water molecules [panel (a)] and ions [panel (b)] that pass through a (9,9) nanotube as functions of time. Results for water are shown as in solid curves, and sodium and chloride ions are represented by dashed and dotted curves, respectively. Note that counts during first 1 ns are not displayed because this is the equilibration period. The red and green curves are for the TIP4P/2005 and TIP3P models, respectively.

Water model	Particle	Temperature				Activation energy (kJ mol^{-1})
		260 K	280 K	300 K	320 K	
Flow rates (ns^{-1}), 0.25 mol L^{-1} NaCl solution						
TIP4P /2005	H$_2$O	10.1 (2.8)	37.3 (4.4)	102.1 (2.9)	206.3 (8.4)	35.0 (3.1)
	Na$^+$	< 0.1	< 0.1	0.1 (0.2)	0.3 (0.1)	n/a
	Cl$^-$	< 0.1	< 0.1	0.1 (0.1)	0.2 (0.2)	
TIP3P	H$_2$O	174.6 (6.6)	331.0 (9.2)	452.9 (11.9)	570.9 (9.0)	13.5 (0.5)
	Na$^+$	0.4 (0.2)	0.8 (0.4)	1.1 (0.3)	1.4 (0.4)	14.3 (6.4)
	Cl$^-$	0.2 (0.1)	0.4 (0.2)	0.5 (0.3)	0.6 (0.2)	12.4 (6.9)
Flow rates (ns^{-1}), 1 mol L^{-1} NaCl solution						
TIP4P /2005	H$_2$O	8.6 (4.2)	34.3 (3.0)	89.8 (5.9)	179.8 (5.6)	35.1 (5.3)
	Na$^+$	< 0.1	< 0.1	0.4 (0.2)	1.3 (0.4)	n/a
	Cl$^-$	< 0.1	< 0.1	0.2 (0.2)	0.8 (0.1)	
TIP3P	H$_2$O	175.6 (6.8)	283.5 (17.9)	389.7 (7.6)	488.0 (9.4)	11.8 (0.5)
	Na$^+$	1.3 (0.2)	2.3 (0.3)	3.1 (0.4)	4.1 (0.6)	13.1 (2.3)
	Cl$^-$	1.0 (0.4)	1.7 (0.5)	2.2 (0.5)	2.9 (0.2)	12.0 (4.6)
Flow rates (ns^{-1}), 2.8 mol L^{-1} NaCl solution						
TIP4P /2005	H$_2$O	7.4 (1.5)	27.2 (7.5)	81.3 (4.1)	145.2 (7.3)	34.9 (2.4)
	Na$^+$	< 0.1	0.2 (0.2)	1.3 (0.2)	2.8 (0.5)	n/a
	Cl$^-$	< 0.1	0.2 (0.2)	1.0 (0.3)	2.2 (0.3)	
TIP3P	H$_2$O	108.5 (15.9)	196.4 (6.4)	297.5 (10.8)	372.8 (10.6)	14.4 (1.6)
	Na$^+$	2.0 (0.6)	3.9 (0.6)	5.5 (0.5)	7.0 (0.7)	14.4 (3.4)
	Cl$^-$	1.8 (0.7)	3.0 (0.7)	4.8 (0.4)	5.9 (0.8)	14.0 (4.5)

Table 5.1: Summary of flow rates for water molecules and ions as well as the calculated activation energies for different water models. The numbers in brackets are estimated standard deviations.
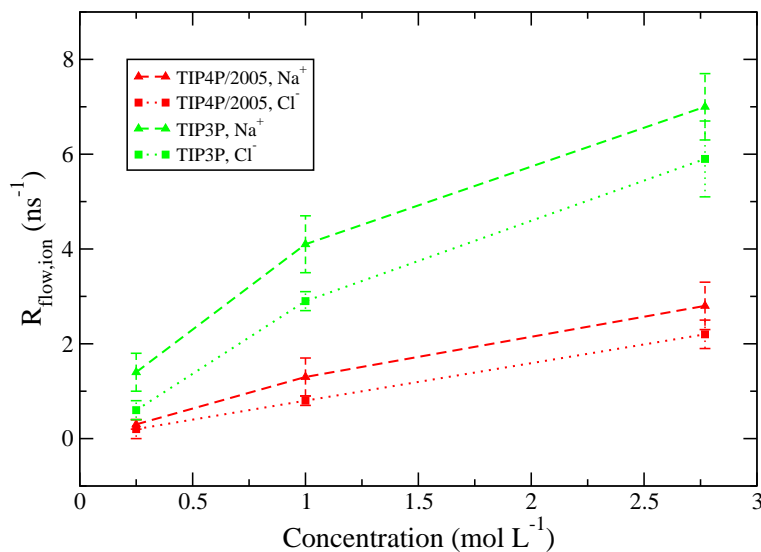
Figure 5.2: Ion flow rates as functions of the NaCl concentration. Results are obtained from simulations conducted at 320 K. The water models and specific particles are indicated in the legend.

at 0.25, 1, and 2.8 mol L^{-1}, respectively. The corresponding diffusion coefficients for TIP3P are 5.48×10^{-5}, 5.35×10^{-5}, 4.64×10^{-5}, and 3.23×10^{-5} cm^2 s^{-1}, displaying the same trend.

While water flow rates remain measurable at low temperatures, the ion flow rates are sometimes too slow to be determined in 10 ns simulations, especially for the TIP4P/2005 model. For example, at 260 K it required on average 20 ns in order to observe a single ion conduction event for the TIP4P/2005 model. In general, ion flow rates for TIP3P solutions are much faster than those for TIP4P/2005. We also note that Na$^+$ has faster transport rates than Cl$^-$ for both water models. The ion flow rate is also sensitive to temperature, increasing as the temperature increases. Additionally, the ion flow rate increases with the salt concentration of the feed reservoir, as illustrated in Figure 5.2.

We would expect the ion flow rate to be strongly influenced by the water flow rate and the ion concentration. Therefore, in order to control for these influences and isolate other factors affecting ion conduction, it is useful to introduce an ion transport efficiency parameter, ξ_{ion}, defined as

$$\xi_{\text{ion}} = \frac{R_{\text{flow,ion}}/\rho_{\text{ion}}}{R_{\text{flow,water}}/\rho_{\text{water}}} \ , \tag{5.1}$$

where ρ_{water} and ρ_{ion} are particle number densities for water molecules and either ion, respectively. Note that if the ion and water flow rates normalized by the particle densities were equal, then ion transport efficiency parameters would be one. Parameters less than one indicate that ion transport is less efficient than water transport. It is worth mentioning that a somewhat similar quantity, called "the percentage salt rejection", was defined by Corry and co-workers[88, 95, 159] to quantify the resistance to ion conduction through a membrane constructed of nanotubes.

Results for the ion transport efficiency parameter from MD simulations are summarized in Table 5.2. For both water models, the parameters are always significantly less than one, suggesting that ions experience more hindrance than water during transport. Also, the sodium ion parameters are larger than or equal to those of chloride ion, as is obvious from the relative ion flow rate values given in Table 5.1. However, apart from these common features, the parameters for TIP4P/2005 and TIP3P solutions are strikingly different. At 260 and 280 K, the parameters of both sodium and chloride ions for the TIP4P/2005 model are too small to accurately measure even in our longest simulation runs, whereas, for the TIP3P model the parameters are significant and readily accessible at these temperatures. Also, the ion transport efficiency parameter is approximately constant for TIP3P but strongly influenced by temperature for TIP4P/2005.

5.3 Why Water and Ion Conduction Is Dependent on the Water Model Employed

In earlier chapters, we demonstrated that for the (9,9) CNT, pure water transport is dependent on two factors: the bulk fluid shear viscosity and the structure of confined water. Based on these observations, a logical speculation is that the model dependence of the ion flow rate is of similar origin. We argue that there are two potential explanations. It is possible that

Water model	Particle	Temperature			
		260 K	280 K	300 K	320 K
Ion transport efficiency parameter, 0.25 mol L^{-1} NaCl solution					
TIP4P/2005	Na$^+$	n/a	n/a	0.22 (0.42)	0.32 (0.09)
	Cl$^-$			0.22 (0.21)	0.21 (0.20)
TIP3P	Na$^+$	0.50 (0.23)	0.53 (0.25)	0.53 (0.13)	0.54 (0.15)
	Cl$^-$	0.25 (0.12)	0.26 (0.19)	0.24 (0.14)	0.23 (0.07)
Ion transport efficiency parameter, 1 mol L^{-1} NaCl solution					
TIP4P/2005	Na$^+$	n/a	n/a	0.24 (0.10)	0.39 (0.11)
	Cl$^-$			0.18 (0.11)	0.24 (0.02)
TIP3P	Na$^+$	0.40 (0.05)	0.43 (0.03)	0.42 (0.05)	0.45 (0.03)
	Cl$^-$	0.30 (0.08)	0.32 (0.07)	0.30 (0.06)	0.32 (0.02)
Ion transport efficiency parameter, 2.8 mol L^{-1} NaCl solution					
TIP4P/2005	Na$^+$	n/a	0.13 (0.10)	0.29 (0.03)	0.35 (0.04)
	Cl$^-$		0.13 (0.16)	0.22 (0.06)	0.27 (0.02)
TIP3P	Na$^+$	0.33 (0.05)	0.36 (0.04)	0.33 (0.02)	0.34 (0.02)
	Cl$^-$	0.30 (0.07)	0.28 (0.06)	0.29 (0.01)	0.29 (0.03)

Table 5.2: Ion transport efficiency parameters ξ_{ion} for different water models. The numbers in brackets are estimated standard deviations.

the ion flow rate is closely connected with the mobility of the bulk solution, and the ring-like structures occurring with TIP4P/2005 impede not only water but also ion conduction. To further explore the mechanism of ion conduction and its dependence on the water model employed, in the following analysis we focus on the 1 mol L^{-1} system.

We find that flow rate results of water again follow the Arrhenius relationship (Equation (4.1)), as plotted in Figure 5.3. The estimated activation energies are included in Table 5.1. As with pure water, TIP4P/2005 has a much higher activation energy than TIP3P ($\sim$35.1 versus $\sim$11.8 kJ mol^{-1}) in salt solutions. For both TIP4P/2005 and TIP3P, the activation energies do not strongly depend on the solution concentration. Note that the activation energy for TIP4P/2005 obtained from 1 mol L^{-1} simulations is higher than that of pure water simulations ($\sim$35.1 versus $\sim$30.5 kJ mol^{-1}). We believe that both activation energies agree with each other if we allow for the large standard deviations of activation energies (5.3 and 2.7 kJ mol^{-1}). The ion flow rates for TIP3P are well fit by the Arrhenius relationship, as plotted in Figure 5.4. But for the TIP4P/2005 model the very low flow rates of ions and associated large uncertainties at 260 and 280 K do not allow meaningful fits to the Arrhenius equation.

Entry rate results, R_{entry}, together with activation energies are presented in Table 5.3. We observe that for TIP4P/2005, the estimated activation energy of the water entry rate obtained from the 1 mol L^{-1} solution agrees with that from the pure water system within the error estimates. Whereas for TIP3P, such activation energies are close with a difference of $\sim$2.0 kJ mol^{-1}. For TIP4P/2005 ion entry rates are not too small to be accurately measured in our simulations. It is interesting to compare ion entry rates with ion flow rates. For TIP3P the entry rates for chloride ions are faster or, taking account of error estimates, at least equal to those of sodium ions, whereas the chloride flow rates are lower than those of sodium. For the TIP4P/2005 model, the entry rates for both ions are indistinguishable within the error estimates, but, at least at 320 K, the sodium ion conduction rate is faster than the chloride ion. It suggests that sodium ions experience less resistance than chloride ions, which is likely due to the smaller "size" of the sodium ion.[160]
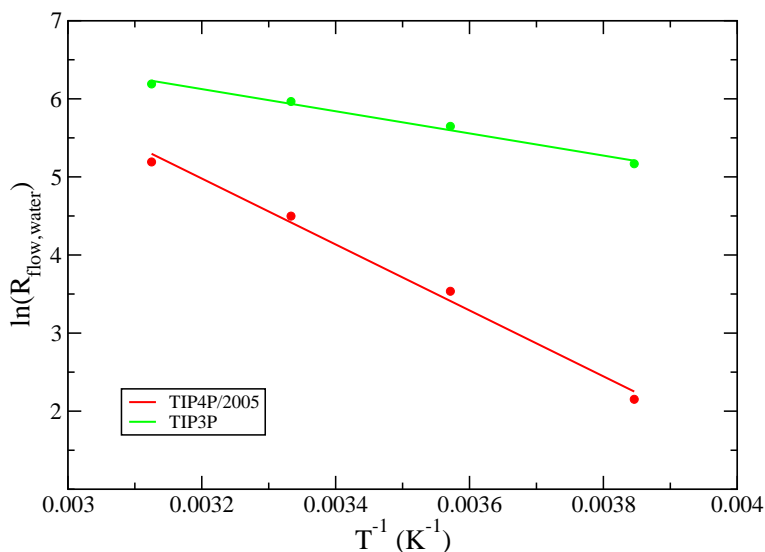
Figure 5.3: The dependence of $ln(R_{\mathrm{flow,water}})$ on T^{-1}. The results are obtained from simulations of 1 mol L^{-1} NaCl solution; results at other concentrations show similar behavior. The water models are indicated in the legends.
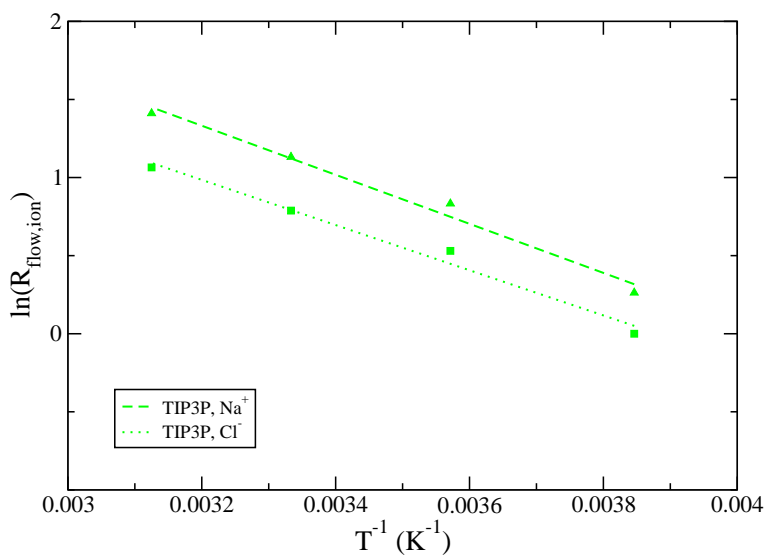
Figure 5.4: The dependence of $ln(R_{\mathrm{flow,ion}})$ on T^{-1}. The results are obtained from simulations of 1 mol L^{-1} NaCl solution; results at other concentrations show similar behavior. The water model and specific particles are indicated in the legends.

Diffusion coefficients of all three particles are summarized results in Table 5.4. The results obtained for sodium and chloride ions with the TIP3P model at 300 K are close to those (2.28×10^{-5} cm^2 s^{-1} for sodium and 2.90×10^{-5} for chloride) reported by Joung and Cheatham.[137] Joung and Cheatham[137] also pointed out the large discrepancies in the ion diffusion coefficients obtained with different water models. The activation energies included in Table 5.4 are calculated from fits to the Arrhenius equation. Activation energies of ion diffusion coefficients are relatively close to those of ion entry rates, demonstrating that again the entry rates are strongly influenced by the bulk viscosity.

Plots of the rate ratios $R_{\text{flow}}/R_{\text{entry}}$ for water and ions are given in Figure 5.5. For water, the pattern is the same as in our pure water simulations. The ratio for TIP3P is $\sim$0.8 and shows little dependence on temperature, suggesting that the flow and entry rates are closely connected at all temperatures investigated. In contrast, the ratio for TIP4P/2005 is $\sim$0.2 at 260 K and increases to $\sim$0.7 at 320 K. For TIP4P/2005, we believe that the entry and flow rates do not strongly correlate at lower temperatures, where the water structure within the nanotube slows down the conduction, but the importance of the entry rate increases at higher temperatures where confined water is less structured. To confirm this reasoning, we again analyze the water structure inside the CNT as described in Chapter 2.6.2. In particular, it is useful to determine the average percentage of water molecules within the nanotube that are not part of any ring-like configuration, or ring-free molecules. The average number of hydrogen bonds per water molecule (hydrogen bond number) is useful as well given that ring-free molecules often associate with a smaller hydrogen bond number. The results given in Table 5.5 are obtained from MD simulations of 1 mol L^{-1} NaCl solution. Note that we used only frames where no ions were present within the nanotube in calculating the averages. From Table 5.5 we see that there are far fewer ring-free molecules for TIP4P/2005 than for TIP3P, indeed for TIP4P/2005 ring free molecules are very rare at the lower temperatures. For both water models, the percentage of ring-free molecules increases with temperature, but the growth is much more dramatic for TIP4P/2005 (2.5% at 260 K to 41.9% at 320 K) than for TIP3P (32.5% to 65.6%, correspondingly). Consistently, hydrogen bond numbers for the

Water model	Particle	Temperature				Activation energy (kJ mol^{-1})
		260 K	280 K	300 K	320 K	
Entry rates (ns^{-1}), 1 mol L^{-1} NaCl solution						
TIP4P /2005	H$_2$O	44.7 (2.7)	84.6 (4.2)	153.5 (6.4)	257.3 (5.4)	20.2 (0.7)
	Na$^+$	< 0.1	0.3 (0.3)	1.0 (0.2)	2.3 (0.5)	n/a
	Cl$^-$	< 0.1	0.2 (0.1)	0.8 (0.4)	2.4 (0.4)	
TIP3P	H$_2$O	235.9 (3.8)	355.1 (13.9)	470.6 (5.3)	579.7 (4.9)	10.4 (0.2)
	Na$^+$	2.0 (0.2)	3.1 (0.4)	3.9 (0.3)	4.9 (0.6)	10.2 (1.7)
	Cl$^-$	2.2 (0.3)	3.5 (0.4)	4.1 (0.3)	5.2 (0.3)	9.6 (1.6)

Table 5.3: Summary of entry rates for water molecules and ions in addition to the calculated activation energies. The numbers in brackets are estimated standard deviations.

Water model	Particle	Temperature				Activation energy (kJ mol^{-1})
		260 K	280 K	300 K	320 K	
Diffusion coefficient (10^{-5} cm^2·s^{-1}), 1 mol L^{-1} NaCl solution						
TIP4P /2005	H$_2$O	0.43 (0.02)	0.95 (0.04)	1.73 (0.07)	2.67 (0.08)	21.1 (0.6)
	Na$^+$	0.11 (0.01)	0.38 (0.02)	0.69 (0.07)	1.16 (0.17)	26.8 (1.8)
	Cl$^-$	0.27 (0.08)	0.53 (0.05)	0.88 (0.07)	1.36 (0.46)	18.6 (4.7)
TIP3P	H$_2$O	2.29 (0.06)	3.33 (0.16)	4.64 (0.16)	5.99 (0.10)	11.1 (0.4)
	Na$^+$	0.80 (0.27)	1.51 (0.28)	2.18 (0.57)	2.73 (0.29)	14.2 (4.0)
	Cl$^-$	1.38 (0.54)	1.76 (0.26)	2.74 (0.59)	3.12 (0.49)	10.0 (4.6)

Table 5.4: Summary of diffusion coefficients for water molecules and ions together with the calculated activation energies. The numbers in brackets are estimated standard deviations.
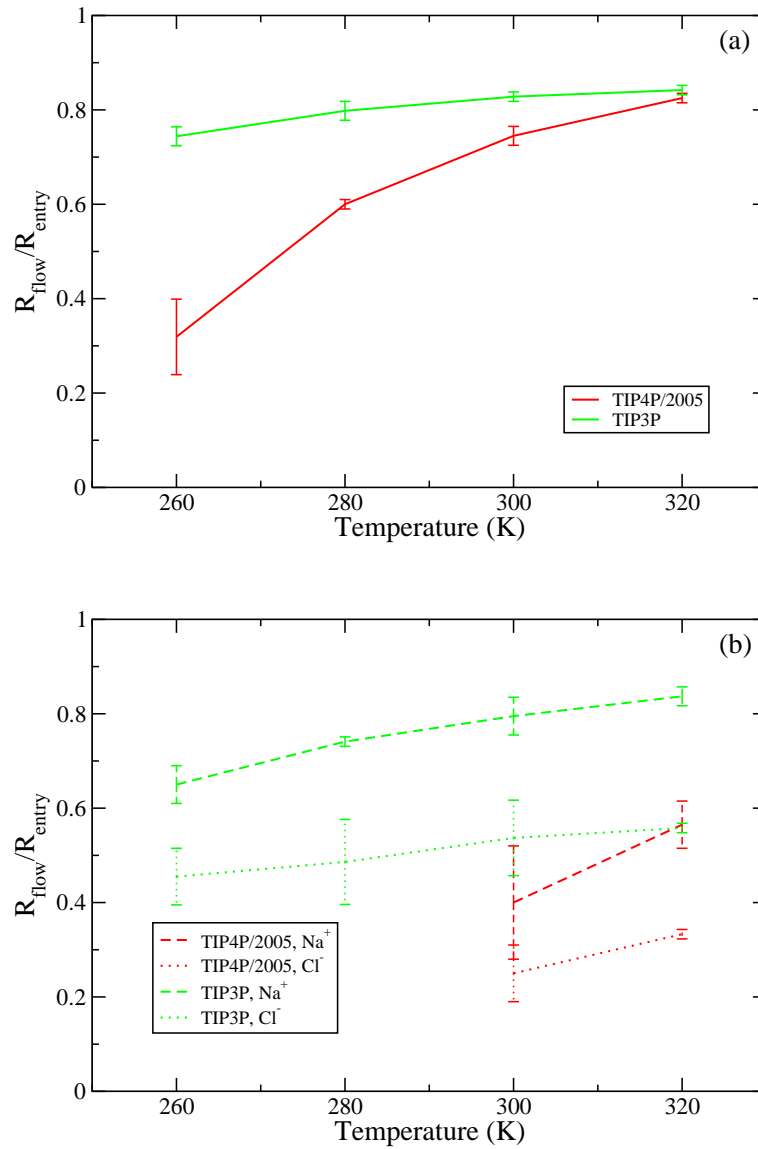
Figure 5.5: Temperature dependence of the ratio $R_{\text{flow}}/R_{\text{entry}}$ for water [panel (a)] and ions [panel (b)]. The water models and specific particles are indicated in the legends.

Water model	Temperature			
	260 K	280 K	300 K	320 K
Ring-free molecules (%)				
TIP4P/2005	2.5	5.3	14.8	41.9
TIP3P	32.5	57.4	61.8	65.6
Hydrogen bond number				
TIP4P/2005	3.39	3.33	3.22	3.01
TIP3P	3.26	2.88	2.75	2.66

Table 5.5: Selected structural properties of water molecules confined within the nanotube.

TIP4P/2005 model are larger at all four temperatures.

Considering $R_{\text{flow}}/R_{\text{entry}}$ for ions shown in Figure 5.5 we see a similar picture. For TIP3P the ratios for sodium ions vary from ~0.65 to ~0.84 as the temperature rises from 260 to 320 K, while the ratios of chloride ion over the same temperature range vary from ~0.45 to ~0.56, which are remarkably smaller. We attribute this observation to the relative ion size.[160] The larger size of the chloride somewhat impedes its transport through the nanotube. For TIP4P/2005 ratios of both ions are too small to be determined at 260 and 280 K, but at 300 and 320 K, ratios for both ions are noticeably smaller than the TIP3P results, consistent with water structure acting to reduce ion conduction.

By inspecting configurational snapshots that show the ion environment within the CNT we can gain additional insight on this issue. Typical snapshots of 1 mol L^{-1} systems at 300 K are displayed in Figure 5.6. We notice that an ion is usually surrounded by ring-free molecules within the nanotube. The snapshots also support our previous results (Table 5.5) which show that TIP4P/2005 has fewer ring-free molecules than TIP3P. Also, we see that for TIP4P/2005, the fraction of ring-free molecules and the ion transport efficiency parameters are both strongly temperature dependent, however, for TIP3P the temperature dependence is much weaker. These results suggest that an ion can more easily enter the nanotube if the molecules near the orifice are ring-free, or in other words if any ring-like structures are broken down before or during the entry process. Perhaps this is also true for ion passage through the

nanotube.

Equilibrium ion potential of mean force (PMF) curves for 1 mol L^{-1} systems at 300 K are plotted in Figure 5.7. The PMF results provide some support for the argument given above. For the TIP3P model, the free energy barriers for sodium and chloride ions are ~9.9 and ~10.6 kJ mol^{-1}, which are in accord with earlier results obtained by Beu.[97] We note that the higher free energy barrier for chloride agrees well with its slightly smaller flow rate compared with sodium, although the chloride ion does have a somewhat faster entry rate. For the TIP4P/2005 model, the equilibrium free energy barriers are obviously larger, ~15 kJ mol^{-1} for sodium and ~20 kJ mol^{-1} for chloride ion, consistent with the much slower entry and flow rates observed for this water model. Moreover, the PMF curves for the TIP4P/2005 solution increase as the ion moves towards the center of the nanotube, possibly suggesting additional friction during the conduction process.

We have already discussed entrance effects on water conduction through CNTs in Chapter 4.4. It is natural to question whether such effects influence ion conduction as well. It has been shown that continuum hydrodynamics can, at least in some cases, give a good description of water entry into (and sometimes flow through) nanotubes. For the (9,9) nanotube, we showed that the ratio RT/D_{water} of the TIP3P model is approximately constant for both entry and flow rates. For the TIP4P/2005 model, the relationship is roughly correct for the entry rate but does not hold for the flow rate. We attributed this failure to the more complex molecular structure formed within the (9,9) nanotube, which creates an additional resistance to flow. Here we considered RT/D_{water} for both water and ions in the 1 mol L^{-1} solution. Provided that R_{Stokes} is not strongly temperature dependent (which is reasonably anticipated), we would expect the ratio to be approximately constant regardless of the simulated temperature.

Plots of $R_{\text{flow,water}}T/D_{\text{water}}$ and $R_{\text{entry,water}}T/D_{\text{water}}$ are given in Figure 5.8. We note that $R_{\text{entry,water}}T/D_{\text{water}}$ shows little variation with temperature for both water models. $R_{\text{flow,water}}T/D_{\text{water}}$ for TIP3P is also generally constant, but not for TIP4P/2005 where the ratio increases with temperature. We see that the behavior pattern is much as we previously observed for pure water for 1 mol L^{-1} solutions.
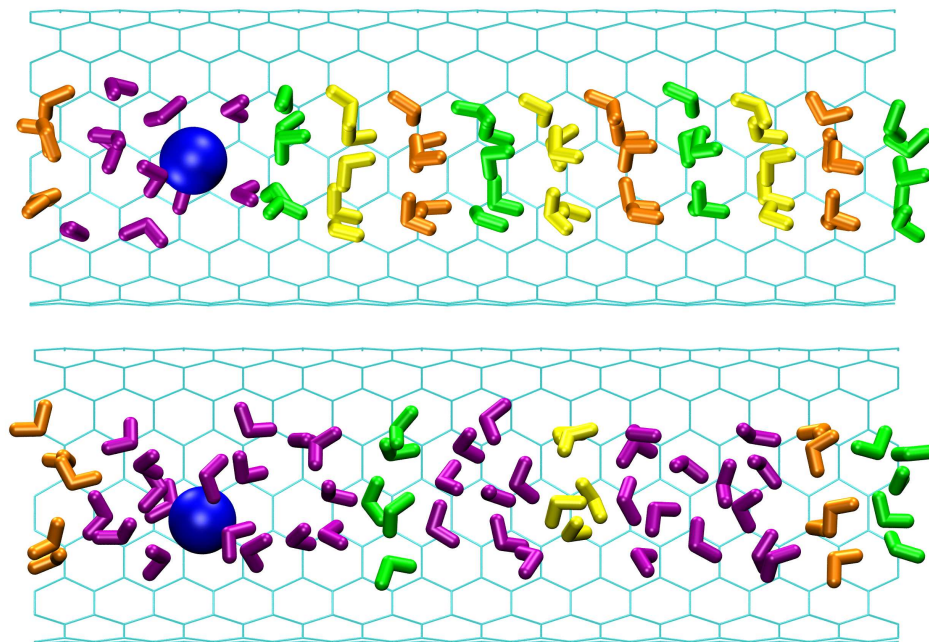
Figure 5.6: Configurational snapshots of the ion environment with TIP4P/2005 (top) and TIP3P (bottom) water inside the nanotube at 300 K. Carbon atoms are cyan, the sodium ion is blue, the stacked ring structures are repeating green, orange and yellow, and ring-free water molecules are magenta. Note that part of the carbon nanotube is not displayed for visual clarity.
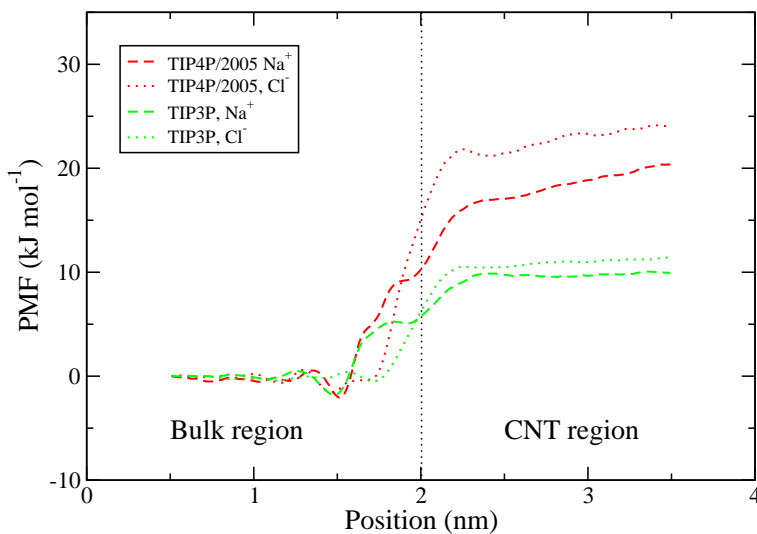
Figure 5.7: Sodium and chloride ion potential of mean force profiles along the nanotube axis as described in the text. The water models and specific particles are indicated in the legends. The black vertical dotted line indicates the position of the (9,9) nanotube orifice.
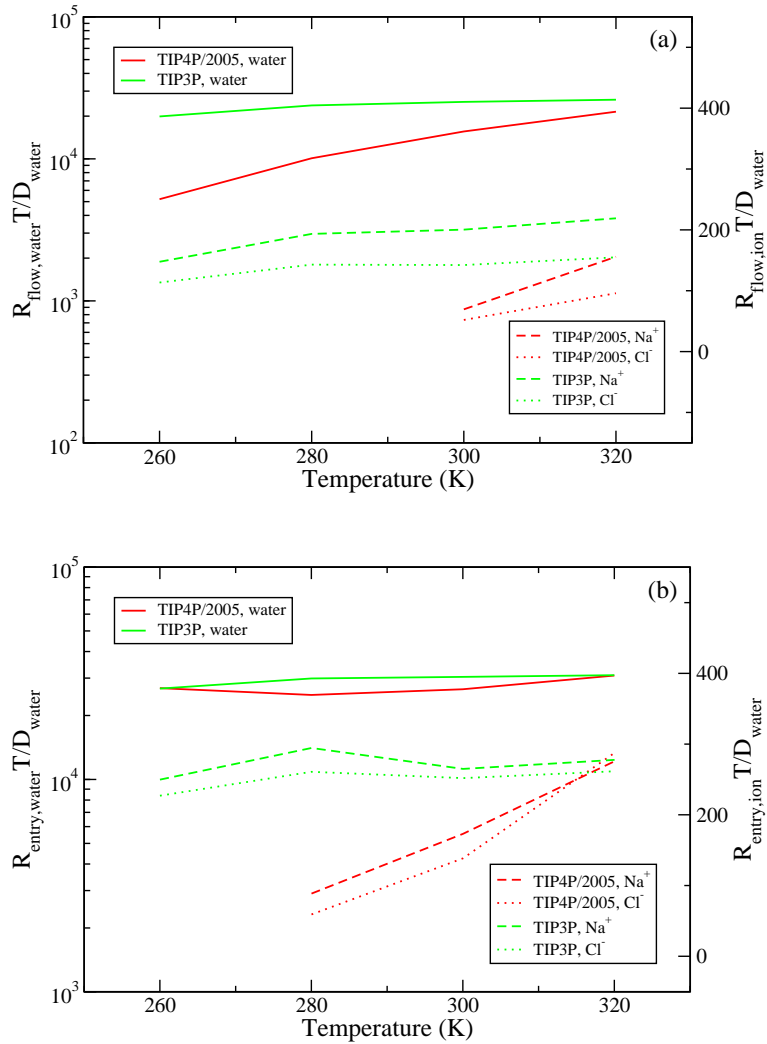
Figure 5.8: Temperature dependence of the ratio $R_{\mathrm{flow}}T/D_{\mathrm{water}}$ [panel (a)] and $R_{\mathrm{entry}}T/D_{\mathrm{water}}$ [panel (b)] in arbitrary units. The water models and specific particles are indicated in the legends. The scale on the left-hand y axis is for water, and the scale on the right-hand y axis is for ions.

Plots of $R_{\text{flow,ion}}T/D_{\text{water}}$ and $R_{\text{entry,ion}}T/D_{\text{water}}$ are also included in Figure 5.8. We note that for the TIP3P model, although $R_{\text{flow,ion}}T/D_{\text{water}}$ does appear to show a small increase with temperature, $R_{\text{entry,ion}}T/D_{\text{water}}$ is again almost constant from 260 to 320 K. The ratio of sodium ions is greater than that of chloride ions. It is reasonable given that a hydrated sodium ion is larger than a hydrated chloride ion.[160] For the TIP4P/2005 model, however, neither ratio remains constant as the temperature increases, indicating that for this model the hydrodynamic description is not adequate even for the entry rate. The ratio values give large uncertainties (not shown in Figure 5.8). One possible explanation of the fact that $R_{\text{entry,ion}}T/D_{\text{water}}$ has a strong temperature dependence is that the number of ring-free water molecules near the orifice of the nanotube increases with increasing temperature, thus reducing a possible barrier to entry. We would not expect continuum hydrodynamics to capture such structural effects. It is worth noting that if the ratio is calculated using D_{ion} rather than D_{water}, similar plots are obtained.

5.4   Summary

We have examined pressure-driven conduction of water and ions through a (9,9) CNT. Results are presented for two common water models, TIP3P and TIP4P/2005, with NaCl concentrations ranging from 0.25 to 2.8 mol L^{-1}, and temperatures from 260 to 320 K. Not surprisingly, our results for water conduction closely parallel our previous findings for pure water transport. For the TIP4P/2005 model, the entry rates are well described by continuum hydrodynamics, but the much slower flow rates are significantly impacted by the water structure within the nanotube, especially at lower temperatures. While for the TIP3P model, both water flow and entry rates are highly connected, which can be largely understood by continuum hydrodynamics.

Ion conduction exhibits similar model dependence. We find that the ion transport efficiency parameters are much smaller for TIP4P/2005 than for TIP3P. In other words, ion conduction experiences stronger resistance with TIP4P/2005 solutions than with TIP3P. It

is particularly true at lower temperatures where the flow rates are too low to be accurately measured in our simulations. We provide evidence that the extra resistance results from the enhanced water structure that occurs with the TIP4P/2005 model within the nanotube. We note that the ion entry rates for the TIP3P model are approximately consistent with continuum hydrodynamics, but that is not true for TIP4P/2005 solutions.

Our results have shown that water structure acts to impede the ion transport, while still allowing water to flow at a significant rate. It is important because, as we demonstrate, it can result in strong model dependence, and this should be kept in mind whenever molecular simulations are being used to investigate ion flow through nanoscopic channels. Additionally, assuming that TIP4P/2005 is a reasonably good water model, our results indicate that reducing the temperature will increase water structure, and strongly reduce ion transport efficiency.

Chapter 6

Conclusions and Perspective

6.1 Simulation Results of Water and Ion Transport through CNTs

With the help of MD simulations, this dissertation investigates water and ion conduction through CNTs under external pressures. We are particularly interested in the influence of water models employed in simulations. Surprisingly, we have shown that the flow rates of both water and ions are remarkably sensitive to the water model employed through both narrow and intermediate-size nanotubes. To seek explanations, we conducted an analysis, investigating the bulk fluid dynamics, the confined water structure, and other potentially relevant factors.

In Chapter 3, we focus on water conduction across intermediate-size CNTs, specifically (8,8) and (9,9) nanotubes, which allow water molecules to form certain ordered arrangements, for example, stacked polygonal configurations, within their cavities. We find that different water models can have distinctive structural features, which can influence the mode of water conduction. Generally speaking, a water model which forms ring-like configurations (represented by TIP4P/2005) tends to adopt a slower cluster-by-cluster conduction mode with many ring clusters moving as single units through the nanotube. In contrast, a water model which forms less ordered structure (represented by TIP3P) is likely to choose a faster diffusive conduction mode with molecules moving as separate particles, rather than as parts of larger clusters.

Within narrow CNTs, such as a (6,6) nanotube, water forms only single-strand, hydrogen-

bonded chains for all three water models considered. Because characteristic structural features, which are observed in intermediate-size nanotubes, do not occur in the (6,6) case, our previous arguments explaining the different water flow rates do not hold. Thus, in Chapter 4 we look for an explanation which can account for the model dependence observed for a narrow nanotube. We discover that the water flow rate strongly correlates with the water entry rate. Both the water entry rate into, and flow rate through, CNTs are activated processes. An Arrhenius-type equation well describes the temperature dependences of both rates. Also, the entry rate appears closely related to the self-diffusion coefficient (or equivalently the shear viscosity) of the particular water model employed.

For the (6,6) CNT, both the flow and entry rates for all water models examined are approximately inversely proportional to the shear viscosity of the bulk liquid, as predicted by continuum hydrodynamics. Therefore, the differences in bulk mobility are reflected in the different flow rates, and this accounts for the strong model dependence. For the (9,9) CNT, these observations also apply to a water model (represented by TIP3P) which has less ordered water structure within the nanotube. However, although the entry rate again agrees with the continuum hydrodynamics predictions for a water model (represented by TIP4P/2005) which has more ordered water structure within the nanotube, this does not apply to the flow rate. In all likelihood, the flow rate is strongly influenced by the water structure within the intermediate-size nanotubes.

In Chapter 5 we investigate water and ion transport through a (9,9) CNT using NaCl solutions of different concentrations. We observe that the flow rates of water, sodium, and chloride ions through the nanotube are not only strongly model dependent but temperature dependent as well. The water conduction rates can be explained as in the pure water simulations. We examine ion conduction in view of the two factors noted above. We show that the ion mobilities in solution can have some influence on the ion conduction rate. In addition, we conclude that highly hydrogen-bonded water structure within the nanotube can greatly increase the resistance to ion conduction. Our results demonstrate that increasing the water structure within the CNT by decreasing the temperature strongly inhibits ion conduction,

Water model	Temperature				Activation energy (kJ mol^{-1})
	278 K	298 K	318 K	373 K	
Self-diffusion coefficient (10^{-5} cm^{2}s^{-1})					
Experimental	1.31	2.30	3.57	n/a	18.4
TIP4P/2005	1.27	2.06	3.07	n/a	16.2
SPC/E	1.54	2.54	3.57	n/a	15.4
TIP3P	3.72	5.49	6.31	n/a	9.7
Shear viscosity, 1 bar (10^{-4} Pa s)					
Experimental	n/a	8.96	n/a	2.84	n/a
TIP4P/2005	n/a	8.55	n/a	2.89	n/a
SPC/E	n/a	7.29	n/a	2.69	n/a
TIP3P	n/a	3.21	n/a	1.65	n/a

Table 6.1: Experimental data of real water and simulation results for different water models. The numbers are obtain from Reference 132.

while still permitting significant water transport. It is particularly true for water models such as the TIP4P/2005 model, which have highly ordered structures at lower temperatures but less ordered at higher temperatures.

We have demonstrated that the simulated water and ion transport rates through various CNTs can exhibit strong water model dependences. This observation should be kept in mind whenever MD simulations are used to investigate water and ion flow through nanoscopic channels. A good water model should simulate real water properties as accurately as possible. Recently, Vega and Abascal[132] proposed a test in which many properties of water are taken into account to evaluate the performance of a water model. All three water models (TIP4P/2005, SPC/E, and TIP3P) present in this dissertation were subjected to their test. Experimental data of real water and simulation results for different water models are tabulated in Table 6.1. The TIP4P/2005 model achieves the highest score in reproducing overall water properties, especially the self-diffusion coefficient and the shear viscosity. Moreover, the

experiments[29, 60] have identified quasi-one-dimensional water structures within intermediate-size nanotubes. Our simulation results (Tables 3.2, 5.5, and Figures 3.6, 3.7, 5.6) show that the TIP4P/2005 model tends to form stacked ring configurations, even at room temperature. Therefore, taken together, our results suggest that it would be desirable to select a water model such as TIP4P/2005 in future simulation studies of water and ion transport through nanoscopic channels.

6.2 Future Work

The work in Chapter 5 generates a question: why do continuum hydrodynamic predictions of ion entry rates agree well with the TIP3P model but fail with the TIP4P/2005 model? We proposed that the water structure near the orifice of the nanotube could be a potential explanation; however, this has not been justified by simulations. Studying this question might give further insight into entrance effect on ion conduction.

As described in Chapter 1.2, the water flow rates through CNTs are observed to be faster than those predicted by the classical hydrodynamic equation of Poiseuille flow (Equation (1.1)). A recent paper[71] summarized the results of water flow enhancement through nanotubes from various simulation studies. It is astonishing that these results differ by one to five orders of magnitude. The present dissertation at least provides some plausible explanations, including the liquid diffusivity in bulk, and the confined molecular structure of the water. In future work one could conduct MD simulations using appropriate water models, for example, the TIP4P/2005 model as we suggest, so as to improve the accuracy of simulation results through CNTs. Additionally, it would be interesting to investigate whether the water model dependence exists for other types of nanoscopic channels, such as boron-nitride nanotubes (BNNTs) and aquaporins.

Being effective water conduits, CNTs are regarded as a promising candidate for nano-filtration. Many studies[88, 89, 107–111] have made significant efforts on modifying nanotube properties to make them more efficient in excluding or selecting certain ions. Because the

water structure inside nanotubes makes a substantial difference in water and ion flow rates, our results suggest that inducing the formation of polygonal ring configurations might be an important attribute to consider, which could be achieved by designing or even synthesizing nanoscopic channels with desired diameters. We predict that stacked ring-like structures within channels should improve the separation efficiency of water from ions.

Water and ion conduction through nanoscopic channels of different geometric shape is a subject of board interest. Intriguing examples are channels with the hourglass shape,[156,161,162] which have larger orifices than simple cylindrical nanotubes. Given the fact that entrance effects are important, as demonstrated in the current dissertation, one might expect that the overall resistance will decrease because water and ions can more easily enter the channel, however, the potential influence of structural differences between the orifices and the central nanotube is unclear. Slablike channels are another interesting example.[163] Algara-Siller *et al.*[163] experimentally observed a "square ice" phase for water confined between two graphene sheets, and further confirmed their observations using MD simulation results. Considering that ordered structures within nanotubes can impede the flow of water and ions, it would be interesting to learn whether this conclusion can be extrapolated to the case of slablike channels.

Bibliography

[1] P. Agre, L. S. King, M. Yasui, W. B. Guggino, O. P. Ottersen, Y. Fujiyoshi, A. Engel, and S. Nielsen, J. Physiol., **542**, 3 (2002).

[2] P. Agre, Angew. Chem. Int. Ed., **43**, 4278 (2004).

[3] T. Zeuthen, J. Membr. Biol., **234**, 57 (2010).

[4] A. S. Verkman, J. Cell Sci., **124**, 2107 (2011).

[5] T. Gonen and T. Walz, Quart. Rev. Biophys., **39**, 4 (2006).

[6] C. Zhao, H. Shao, and L. Chu, Colloids Surf. B, **62**, 163 (2008).

[7] D. F. Savage, J. D. O'Connell III, L. J. W. Miercke, J. Finer-Moore, and R. M. Stroud, Proc. Natl. Acad. Sci. U. S. A., **107**, 17164 (2010).

[8] Y. Wang and E. Tajkhorshid, J. Nutr., **137**, 1509S (2007).

[9] A. J. Yool and E. M. Campbell, Mol. Aspects Med., **33**, 553 (2012).

[10] B. Roux, Annu. Rev. Biophys. Biomol. Struct., **34**, 153 (2005).

[11] B. Corry and M. Thomas, J. Am. Chem. Soc., **134**, 1840 (2012).

[12] S. B. Long, E. B. Campbell, and R. MacKinnon, Science, **309**, 897 (2005).

[13] H. Berkefeld, B. Fakler, and U. Schulte, Physiol. Rev., **90**, 1437 (2010).

[14] C. Tang, Y. Zhao, R. Wang, C. Hélix-Nielsen, and A. G. Fane, Desalination, **308**, 34 (2013).

[15] T. J. Jentsch, V. Stein, F. Weinreich, and A. A. Zdebik, Physiol. Rev., **82**, 503 (2002).

[16] S. Nielsen, J. Frøkiær, D. Marples, T. Kwon, P. Agre, and M. A. Knepper, Physiol. Rev., **82**, 205 (2002).

[17] A. L. George Jr., J. Clin. Invest., **115**, 1990 (2005).

[18] J. J. Kasianowicz, Chem. Rev., **112**, 6215 (2012).

[19] A. S. Verkman, Annu. Rev. Med., **63**, 303 (2012).

[20] A. S. Verkman, M. O. Anderson, and M. C. Papadopoulos, Nat. Rev. Drug Discov., **13**, 259 (2014).

[21] P. R. Bandaru, J. Nanosci. Nanotechnol., **7**, 1239 (2007).

[22] K. Liew, Z. Lei, and L. Zhang, Compos. Struct., **120**, 90 (2015).

[23] Z. Han and A. Fina, Prog. Polym. Sci., **36**, 914 (2011).

[24] J. Prasek, J. Drbohlavova, J. Chomoucka, J. Hubalek, O. Jasek, V. Adam, and R. Kizek, J. Mater. Chem., **21**, 15872 (2011).

[25] A. I. Kolesnikov, J. Zanotti, C. Loong, P. Thiyagarajan, A. P. Moravsky, R. O. Loutfy, and C. J. Burnham, Phys. Rev. Lett., **93**, 035503 (2004).

[26] N. Naguib, H. Ye, Y. Gogotsi, A. G. Yazicioglu, C. M. Megaridis, and M. Yoshimura, Nano Lett., **4**, 2237 (2004).

[27] Q. Chen, J. L. Herberg, G. Mogilevsky, H. Wang, M. Stadermann, J. K. Holt, Y. Wu, Nano Lett., **8**, 1902 (2008).

[28] A. Das, S. Jayanthi, H. S. M. V. Deepak, K. V. Ramanathan, A. Kumar, C. Dasgupta, and A. K. Sood, ACS Nano, **4**, 1687 (2010).

[29] H. Kyakuno, K. Matsuda, H. Yahiro, Y. Inami, T. Fukuoka, Y. Miyata, K. Yanagi, Y. Maniwa, H. Kataura, T. Saito, M. Yumura, and S. Iijima, J. Chem. Phys., **134**, 244501 (2011).

[30] E. Paineau, P. Albouy, S. Rouzière, A. Orecchini, S. Rols, and P. Launois, Nano Lett., **13**, 1751 (2013).

[31] S. D. Bernardina, E. Paineau, J.-B. Brubach, P. Judeinstein, S. Rouzière, P. Launois, P. Roy, J. Am. Chem. Soc., **138**, 10437 (2016).

[32] X. Pan, Z. Fan, W. Chen, Y. Ding, H. Luo, and X. Bao, Nat. Mater., **6**, 507 (2007).

[33] F. Du, L. Qu, Z. Xia, L. Feng, and L. Dai, Langmuir, **27**, 8437 (2011).

[34] H. Zhang, X. Pan, X. Han, X. Liu, X. Wang, W. Shen, and X. Bao, Chem. Sci., **4**, 1075 (2013).

[35] J. Geng, K. Kim, J. Zhang, A. Escalada, R. Tunuguntla, L. R. Comolli, F. I. Allen, A. V. Shnyrova, K. Cho, D. Munoz, Y. M. Wang, C. P. Grigoropoulos, C. M. Ajo-Franklin, V. A. Frolov, and A. Noy, Nature, **514**, 612 (2014).

[36] W. Yu, P. Hou, F. Li, and C. Liu, J. Mater. Chem., **22**, 13756 (2012).

[37] J. K. Holt, H. G. Park, Y. Wang, M. Stadermann, A. B. Artyukhin, C. P. Grigoropoulos, A. Noy, and O. Bakajin, Science, **312**, 1034 (2006).

[38] X. Qin, Q. Yuan, Y. Zhao, S. Xie, and Z. Liu, Nano Lett., **11**, 2173 (2011).

[39] H. Lee, H. Kim, Y. Cho, and H. Park, Small, **10**, 2653 (2014).

[40] P. Pang, J. He, J. Park, P. S. Krstić, and S. Lindsay, ACS Nano, **5**, 7277 (2011).

[41] W. Choi, C. L, M. Ham, S. Shimizu, and M. S. Strano, J. Am. Chem. Soc., **133**, 203 (2011).

[42] W. Choi, Z. W. Ulissi, S. F. E. Shimizu, D. O. Bellisario, M. D. Ellison, and M. S. Strabo, Nat. Commun., **4**, 2397 (2013).

[43] L. Liu, C. Yang, K. Zhao, J. Li, and H. Wu, Nat. Commum., **4**, 2989 (2013).

[44] J. Wu, K. Gerstandt, H. Zhang, J. Liu, and B. J. Hinds, Nat. Nanotechnol., **7**, 133 (2012).

[45] F. Fornasiero, H. Park, J. K. Holt, M. Stadermann, C. P. Grigoropoulos, A. Noy, and O. Bakajin, Proc. Natl. Acad. Sci. U. S. A., **105**, 17250 (2008).

[46] F. Taherian, V. Marcon, and N. F. A. van der Vegt, Langmuir, **29**, 1457 (2013).

[47] G. Hummer, J. C. Rasaiah, and J. P. Noworyta, Nature, **414**, 188 (2001).

[48] H. Kumar, B. Mukherjee, S. Lin, C. Dasgupta, A. K. Sood, and P. K. Maiti, J. Chem. Phys., **134**, 124105 (2011).

[49] H. Kumar, C. Dasgupta, and P. K. Maiti, Mol. Simul. **41**, 504 (2015).

[50] T. A. Pascal, W. A. Goddard, and Y. Jung, Proc. Natl. Acad. Sci. U. S. A., **108**, 11794 (2011).

[51] S. Vaitheeswaran, J. C. Rasaiah, and G. Hummer, J. Chem. Phys., **121**, 7955 (2004).

[52] J. A. Garate, T. Perez-Acle, and C. Oostenbrink, Phys. Chem. Chem. Phys., **16**, 5119 (2014).

[53] A. Waghe, J. C. Rasaiah, and G. Hummer, J. Chem. Phys., **137**, 044709 (2012).

[54] A. Waghe, J. C. Rasaiah, and G. Hummer, J. Chem. Phys., **117**, 10789 (2002).

[55] A. Striolo, Nano Lett., **6**, 633 (2006).

[56] H. Fang, R. Wan, X. Gong, H. Lu, and S. Li, J. Phys. D: Appl. Phys., **41**, 103002 (2008).

[57] J. Köfinger, G. Hummer, and C. Dellago, Phys. Chem. Chem. Phys., **13**, 15403 (2011).

[58] K. Koga, R. D. Parra, H. Tanaka, X. C. Zeng, J. Chem. Phys., 113, 5037 (2000).

[59] K. Koga, G. Gao, H. Tamaka, and X. Zeng, Nature, **412**, 802 (2001).

[60] Y. Maniwa, H. Kataura, M. Abe, A. Udaka, S. Suzuki, Y. Achiba, H. Kira, K. Matsuda, H. Kadowaki, and Y. Okabe, Chem. Phys. Lett., **401**, 534 (2005).

[61] A. Striolo, A. A. Chialvo, K. E. Gubbins, and P. T. Cummings, J. Chem. Phys., **122**, 234712 (2005).

[62] D. Takaiwa, I. Hatano, K. Koga, and H. Tanaka, Proc. Natl. Acad. Sci. U. S. A., **105**, 39 (2008).

[63] J. A. Thomas and A. J. H. McGaughey, Phys. Rev. Lett., **102**, 184502 (2009).

[64] T. Ohba, Angew. Chem. Int. Ed., **53**, 8032 (2014).

[65] Y. Liu, Q. Wang, T. Wu, and L. Zhang, J. Chem. Phys., **123**, 234701 (2005).

[66] S. Li and B. Schmidt, Phys. Chem. Chem. Phys., **17**, 7303 (2015).

[67] M. C. Gordillo and J. Martí, Chem. Phys. Lett., **329**, 341 (2000).

[68] I. Hanasaki and A. Nakatani, J. Chem. Phys., **124**, 144708 (2006).

[69] I. Hanasaki and A. Nakatani, J. Chem. Phys., **124**, 174714 (2006).

[70] Q. Chen, Q. Wang, Y. Liu, and T. Wu, J. Chem. Phys., **140**, 214507 (2014).

[71] S. K. Kannam, B. D. Todd, J. S. Hansen, and P. J. Daivis, J. Chem. Phys., **138**, 094701 (2013).

[72] K. Falk, F. Sedlmeler, L. Joly, R. R. Netz, and L. Bocquet, Nano Lett., **10**, 4067 (2010).

[73] S. Joseph and N. R. Aluru, Nano Lett., **8**, 452 (2008).

[74] C. Won, S. Joseph, and N. R. Aluru, J. Chem. Phys., **125**, 114701 (2006).

[75] P. Sahu and S. M. Ali, J. Chem. Phys., **143**, 184503 (2015).

[76] D. Lu, Phys. Chem. Chem. Phys., **15**, 14447 (2013).

[77] J. Li, X. Gong, H. Lu, D. Li, H. Fang, and R. Zhou, Proc. Natl. Acad. Sci. U. S. A., **104**, 3687 (2007).

[78] X. Gong, J. Li, H. Lu, R. Wan, J. Li, J. Hu, and H. Fang, Nat. Nanotechnol., **2**, 709 (2007).

[79] L. Liu, Y. Qiao, and X. Chen, Appl. Phys. Lett., **92**, 101927 (2008).

[80] X. Li, Y. Shi, Y. Yang, H. Du, R. Zhou, and Y. Zhao, J. Chem. Phys., **136**, 175101 (2012).

[81] S. Hou, Z. Shen, X. Zhao, and Z. Xue, Chem. Phys. Lett., **373**, 308 (2003).

[82] D. Lu, Y. Li, U. Ravaioli, and K. Schulten, J. Phys. Chem. B, **109**, 11461 (2005).

[83] R. Wan, J. Li, H. Lu, and H. Fang, J. Am. Chem. Soc., **127**, 7166 (2005).

[84] L. Wu, F. Wu, J. Kou, and H. Lu, Phys. Rev. E, **83**, 061913 (2011).

[85] M. Melillo, F. Zhu, M. A. Snyder, and J. Mittal, J. Phys. Chem. Lett., **2**, 2978 (2011).

[86] I. Moskowitz, M. A. Snyder, and J. Mittal, J. Chem. Phys., **141**, 18C532 (2014).

[87] F. Ranazani and F. Ebrahimi, J. Phys. Chem. C, **120**, 12871 (2016).

[88] B. Corry, Energy Environ. Sci., **4**, 751 (2011).

[89] Z. E. Hughes, C. J. Shearer, J. Shapter, and J. D. Gale, J. Phys. Chem. C, **116**, 24943 (2012).

[90] C. Peter and G. Hummer, Biophys. J., **89**, 2222 (2005).

[91] L. A. Richards, A. I. Schäfer, B. S. Richards, and B. Corry, Small, **8**, 1701 (2012).

[92] H. Liu, S. Murad, and C. J. Jameson, J. Chem. Phys., **125**, 084713 (2006).

[93] Q. Shao, L. Huang, J. Zhou, L. Lu, L. Zhang, X. Lu, S. Jiang, K. E. Gubbins, and W. Shen, Phys. Chem. Chem. Phys., **10**, 1896 (2008).

[94] E. I. Calixte, O. N. Samoylova, and K. L. Shuford, Phys. Chem. Chem. Phys., **18**, 12204 (2016).

[95] B. Corry, J. Phys. Chem. B, **112**, 1427 (2008).

[96] O. N. Samoylova, E. I. Calixte, and K. L. Shuford, J. Phys. Chem. C, **119**, 1659 (2015).

[97] T. A. Beu, J. Chem. Phys., **132**, 164513 (2010).

[98] Z. He, B. Corry, X. Lu, and J. Zhou, Nanoscale, **6**, 3686 (2014).

[99] J. Liu, G. Shi, P. Guo, J. Yang, and H. Fang, Phys. Rev. Lett., **115**, 164502 (2015).

[100] M. C. F. Wander and K. L. Shuford, J. Phys. Chem. C, **114**, 20539 (2010).

[101] R. Qiao and N. R. Aluru, Nano Lett., **3**, 1013 (2003).

[102] T. Sumikama, S. Saito, and I. Ohmine, J. Phys. Chem. B, **110**, 20671 (2006).

[103] T. Sumikama, S. Saito, and I. Ohmine, J. Chem. Phys., **139**, 165106 (2013).

[104] J. Su and D. Huang, J. Phys. Chem. C, **120**, 11245 (2016).

[105] T. A. Beu, J. Chem. Phys., **135**, 044516 (2011).

[106] J. Azamat, A. Khataee, and S. Joo, RSC Adv. **5**, 25097 (2015).

[107] C. Song and B. Corry, J. Phys. Chem. B, **113**, 7642 (2009).

[108] H. Liu, C. J. Jameson, and S. Murad, Mol. Simul., **34**, 169 (2008).

[109] Q. Shao, J. Zhou, L. Lu, X. Lu, Y. Zhu, and S. Jiang, Nano Lett., **9**, 989 (2009).

[110] D. Tang and D. Kim, Chem. Phys., **428**, 14 (2014).

[111] X. Gong, J. Li, K. Xu, J. Wang, and H. Yang, J. Am. Chem. Soc., **132**, 1873 (2010).

[112] J. D. Bernal and R. H. Fowler, J. Phys. Chem., **1**, 515 (1933).

[113] W. L. Jorgensen, J. Chandrasekhar, J. D. Madura, R. W. Impey, and M. L. Klein, J. Chem. Phys. **79**, 926 (1983).

[114] H. J. C. Berendsen, J. R. Grigera, and T. P. Straatsma, J. Phys. Chem. **91**, 6269 (1987).

[115] P. Ren and J. W. Ponder, J. Phys. Chem. B, **107**, 5933 (2003).

[116] J. L. F. Abascal and C. Vega, J. Chem. Phys. **123**, 234505 (2005).

[117] W. Yu, P. E. M. Lopes, B. Roux, and A. D. MacKerell, Jr., J. Chem. Phys., **138**, 034508 (2013).

[118] B. Guillot, J. Mol. Liq., **101**, 219 (2002).

[119] S. Tanizaki, J. Mavri, H. Partridge, and P. C. Jordan, Chem. Phys., **246**, 37 (1999).

[120] S. Zhu and C. F. Wong, J. Chem. Phys., **98**, 8892 (1993).

[121] D. M. Ferguson, J. Comput. Chem., **16**, 501 (1995).

[122] Y. Wu, H. L. Tepper, and G. A. Voth, J. Chem. Phys., **124**, 024503 (2006).

[123] M. A. González and J. L. F. Abascal, J. Chem. Phys., **135**, 224516 (2011).

[124] J. Wang, P. Cieplak, Q. Cai, M. Hsieh, J. Wang, Y. Duan, and R. Luo, J. Phys. Chem. B, **116**, 7999 (2012).

[125] A. Alexiadis and S. Kassinos, Chem. Rev., **108**, 5014 (2008).

[126] A. Alexiadis and S. Kassinos, Chem. Eng. Sci., **63**, 2793 (2008).

[127] A. Alexiadis and S. Kassinos, Mol. Simul., **34**, 671 (2008).

[128] H. J. C. Berendsen, J. P. M. Postma, W. F. van Gunsteren, and J. Hermans, *Intermolecular Forces* (Reidel, Dordrecht, 1981), p. 331.

[129] Y. Nakamura and T. Ohno, Mater. Chem. Phys., **132**, 682 (2012).

[130] S. W. Rick, J. Chem. Phys., **120**, 6085 (2004).

[131] H. Kumar, C. Dasgupta, and P. K. Maiti, RSC Adv., **5**, 1893 (2015).

[132] C. Vega and J. L. F. Abascal, Phys. Chem. Chem. Phys., **13**, 19663 (2011).

[133] S. Andreev, D. R. Reichman, and G. Hummer, J. Chem. Phys., **123**, 194502 (2005).

[134] T. Darden, D. York, and L. Pedersen, J. Chem. Phys., **98**, 10089 (1993).

[135] U. Essmann, L. Perera, M. L. Berkowitz, T. Darden, H. Lee, and L. G. Pedersen, J. Chem. Phys., **103**, 8577 (1995).

[136] Y. Duan, C. Wu, S. Chowdhury, M. C. Lee, G. Xiong, W. Zhang, R. Yang, P. Cieplak, R. Luo, T. Lee, J. Caldwell, J. Wang, and P. Kollman, J. Comput. Chem. **24**, 1999 (2003).

[137] I. Joung and T. E. Cheatham, III, J. Phys. Chem. B, **112**, 9020 (2008).

[138] D. van der Spoel, E. Lindahl, B. Hess, G. Groenhof, A. E. Mark, and H. J. C. Berendsen, J. Comput. Chem., **26**, 1701 (2005).

[139] G. Bussi, D. Donadio, and M. Parrinello, J. Chem. Phys., **126**, 014101 (2007).

[140] F. Zhu, E. Tajkhorshid, and K. Schulten, Biophys. J., **86**, 50 (2004).

[141] F. Zhu, E. Tajkhorshid, and K. Schulten, Biophys. J., **83**, 154 (2002).

[142] M. E. Suk and N. R. Aluru, J. Phys. Chem. Lett., **1**, 1590 (2010).

[143] L. Wang, R. S. Dumont, and J. M. Dickson, J. Chem. Phys., **137**, 044102 (2012).

[144] A. Luzar and D. Chandler, J. Chem. Phys., **98**, 8160 (1993).

[145] G. M. Torrie and J. P. Valleau, J. Comput. Phys., **23**, 187 (1977).

[146] J. Kästner, WIREs Comput. Mol. Sci., **1**, 932 (2011).

[147] B. Roux, Comput. Phys. Comm., **91**, 275 (1995).

[148] L. Liu and G. N. Patey, J. Chem. Phys., **141**, 18C518 (2014).

[149] L. Liu and G. N. Patey, J. Chem. Phys., **144**, 184502 (2016).

[150] T. A. Hilder, D. Gordon, and S. Chung, Small, **5**, 2183 (2009).

[151] J. Goldsmith and C. C. Martens, J. Phys. Chem. Lett., **1**, 528 (2010).

[152] R. M. Lynden-Bell and J. C. Rasaiah, J. Chem. Phys., **105**, 9266 (1996).

[153] G. Lakatos and G. N. Patey, J. Chem. Phys., **126**, 024703 (2007).

[154] T. B. Sisan and S. Lichter, Microfluid. Nanofluid., **11**, 787 (2011).

[155] J. H. Walther, K. Ritos, E. R. Cruz-Chu, C. M. Megaridis, and P. Koumoutsakos, Nano Lett., **13**, 1910 (2013).

[156] S. Gravelle, L. Joly, C. Ybert, and L. Bocquet, J. Chem. Phys., **141**, 18C526 (2014).

[157] R. A. Sampson, Phil. Trans. R. Soc. Lond. A, **182**, 449 (1891).

[158] L. Liu and G. N. Patey, J. Chem. Phys., **146**, 074502 (2017).

[159] M. Thomas and B. Corry, Phil. Trans. R. Soc. A, **374**, 20150220 (2016).

[160] R. Mancinelli, A. Botti, F. Bruni, M. A. Ricci, and A. K. Soper, J. Phys. Chem. B, **111**, 13570 (2007).

[161] D. Tang, L. Li, M. Shahbabaei, Y. Yoo, and D. Kim, Materials, **8**, 7257 (2015).

[162] M. Shahbabaei and D. Kim, Chem. Phys., **477**, 24 (2016).

[163] G. Algara-Siller, O. Lehtinen, F. Wang, R. R. Nair, U. Kaiser, H. Wu, A. K. Geim, and I. V. Grigorieva, Nature, **519**, 443 (2015).

[164] P. Ewald, Ann. Phys., **369**, 253 (1921).

[165] A. Y. Toukmaji and J. A. Board Jr., Comput. Phys. Comm., **95**, 73 (1996).

[166] R. W. Hockney, S. P. Goel, J. W. Eastwood, J. Comput. Phys., **14**, 148 (1974).

[167] B. Hess, H. Bekker, H. J. C. Berendsen, J. G. E. M. Fraaije, J. Comput. Chem., **18**, 1463 (1997).

[168] J. G. Kirkwood, J. Chem. Phys., **3**, 300 (1935).

[169] A. Kalra, S. Garde, G. Hummer, Proc. Natl. Acad. Sci. U. S. A., **100**, 10175 (2003).

[170] W. D. Nicholls, M. K. Borg, D. A. Lockerby, and J. M. Reese, Microfluid Nanofluid, **12**, 257 (2012).

[171] M. Thomas and B. Corry, Microfluid. Nanofluid., **18**, 41 (2015).

[172] H. J. C. Berendsen, J. P. M. Postma, W. F. Vangunsteren, A. Dinola, and J. R. Haak, J. Chem. Phys., **81**, 3684 (1984).

Appendix A

Molecular Dynamics

A.1 Ewald Summation

As described in Chapter 2.3, the pair electrostatic potential, $u_{\mathrm{C},ij}$, falls off slowly, such that the contributions of long-range interactions to the total potential energy are not negligible. With the application of the periodic boundary conditions, the total Coulombic potential energy of point charges can be expressed as

$$U_{\mathrm{C,total}} = \frac{1}{8\pi\epsilon_0} \sum_i \sum_j \sum_{\boldsymbol{n}'} \frac{q_i q_j}{|\boldsymbol{r}_{ij} + \boldsymbol{n}L|} \ , \tag{A.1}$$

where $\boldsymbol{r}_{ij}$ is the vector from site i to j, $\boldsymbol{n}$ is a vector (n_x, n_y, n_z) specifying the translational index of the image cell, L is a set of coefficients defining the dimensions of the simulation cell (x, y, z), and the prime indicates that the $i = j$ terms for $\boldsymbol{n} = (0,0,0)$ are omitted to avoid calculating self interactions. However, this direct sum is not only slowly but also conditionally convergent.

Ewald summation[164, 165] is introduced to calculate electrostatic interactions. Unlike the direct summation method, which uses discrete Dirac delta functions to describe the charge distributions, the Ewald summation method adds a Gaussian charge distribution of different sign to the original charge distributions, and then subtracts the same Gaussian distribution, with a form of

$$\rho_i(r) = \frac{q_i \alpha^3}{\pi^{\frac{3}{2}}} e^{-\alpha^2 r^2} \ , \tag{A.2}$$

where r is the position relative to the central point charge, and α, which is called the Ewald

convergence parameter, is a positive parameter that determines the width of the distribution. Thereafter, the conditionally convergent sum in Equation (A.1), is reconstructed into three components, two quickly convergent series, and a constant term

$$U_{\text{C,total}} = U_{\text{real}} + U_{\text{rec}} + U_{\text{const}} . \tag{A.3}$$

The two series, U_{real} and U_{rec}, are calculated in real space

$$U_{\text{real}} = \frac{1}{8\pi\epsilon_0} \sum_i \sum_j \sum_{\boldsymbol{n}'} \frac{q_i q_j \text{erfc}(\alpha|\boldsymbol{r}_{ij} + \boldsymbol{n}L|)}{|\boldsymbol{r}_{ij} + \boldsymbol{n}L|} , \tag{A.4}$$

and reciprocal space

$$U_{\text{rec}} = \frac{1}{2\pi V} \sum_i \sum_j q_i q_j \sum_{\boldsymbol{n}'} \frac{\exp\left(-(\pi\boldsymbol{n}/\alpha)^2 + 2\pi i \boldsymbol{n} \boldsymbol{r}_{ij}\right)}{\boldsymbol{n}^2} , \tag{A.5}$$

respectively, where "erfc" indicates the complementary error function. Note that in Equation (A.4), a large value of α makes the real space series converge more rapidly, whereas in Equation (A.5), a small value of α makes the reciprocal space series converge more rapidly. It is important that the simulation cell should be exactly neutral. Otherwise, the series will not be convergent. The constant term U_{const} is a correction term

$$U_{\text{const}} = -\frac{\alpha}{4\pi\epsilon_0\sqrt{\pi}} \sum_i \sum_\alpha q_{i\alpha}^2 , \tag{A.6}$$

which cancels out the interactions of each of introduced artificial charge distributions with itself. The computer time required for the sum of the reciprocal component in the traditional Ewald method increases as N^2, where N is the number of point charges in a simulation cell, therefore, it is not realistic for large systems.

In GROMACS, the particle mesh Ewald (PME) method,[134, 135] which is based on fast Fourier transform (FFT), is used to accelerate the summation of the reciprocal part. In this method, U_{real} in Equation (A.4) is treated as in the traditional Ewald method. U_{rec} in Equation (A.5) is handled by a particle-mesh technique, which converts point charges

into a mesh of density values. The electrostatic potentials are calculated by solving Poisson equations using FFT techniques from the mesh field, and so are the forces on point charges. The computer time required for the PME method increases as $Nlog(N)$, which is much faster than the traditional Ewald method when N is large.

A.2 System Evolution

In our simulations, we employ the leap-frog algorithm[166] as the MD integrator. This algorithm uses atom coordinates $\boldsymbol{r}$ at time t and atom velocities $\boldsymbol{v}$ at time $t - \delta t/2$. The method updates velocities and coordinates using the equations of motion

$$\boldsymbol{v}(t + \frac{\delta t}{2}) = \boldsymbol{v}(t - \frac{\delta t}{2}) + \delta t \boldsymbol{M}^{-1} \boldsymbol{f}(t) \ , \tag{A.7}$$

$$\boldsymbol{r}(t + \delta t) = \boldsymbol{r}(t) + \delta t \boldsymbol{v}(t + \frac{\delta t}{2}) \ , \tag{A.8}$$

where $\boldsymbol{M}$ is a diagonal matrix containing the masses of the particles, and $\boldsymbol{f}(t)$ is the force vector, which is given by

$$\boldsymbol{f}(t) = -\nabla(u_{\mathrm{LJ}}(t) + u_{\mathrm{C}}(t)) \ . \tag{A.9}$$

With rigid models, the distances between pairs of atoms which form chemical bonds are constrained to definite bond lengths d_1, d_2, ... d_i. Therefore, a linear constraint solver (LINCS) algorithm[167] is implemented in GROMACS. This algorithm corrects unconstrained velocities and coordinates using a two-step method. First, taking constraints into consideration, the constrained equations of motion are

$$\boldsymbol{v}(t + \frac{\delta t}{2}) = \big(\boldsymbol{I} - \boldsymbol{T}(t)\boldsymbol{B}(t)\big)\big(\boldsymbol{v}(t - \frac{\delta t}{2}) + \delta t \boldsymbol{M}^{-1}\boldsymbol{f}(t)\big) - \frac{\boldsymbol{T}(t)\big(\boldsymbol{B}(t)\boldsymbol{r}(t) - \boldsymbol{d}\big)}{\delta t} \ , \tag{A.10}$$

$$\boldsymbol{r}'(t + \delta t) = \big(\boldsymbol{I} - \boldsymbol{T}(t)\boldsymbol{B}(t)\big)\big(\boldsymbol{r}(t) + \delta t \boldsymbol{v}(t - \frac{\delta t}{2}) + \delta t^2 \boldsymbol{M}^{-1}\boldsymbol{f}(t)\big) + \boldsymbol{T}(t)\boldsymbol{d} \ , \tag{A.11}$$

where $\boldsymbol{I}$ is the identity matrix, $\boldsymbol{B}(t)$ is a matrix containing the directions of the constraints, $\boldsymbol{d}$ is a vector containing the prescribed bond lengths, and $\boldsymbol{T}(t)$ is a matrix defined by the expression $\boldsymbol{M}^{-1}\boldsymbol{B}(t)^{\boldsymbol{T}}\left(\boldsymbol{B}(t)\boldsymbol{M}^{-1}\boldsymbol{B}(t)^{\boldsymbol{T}}\right)^{-1}$. However, Equation (A.11) sets the projections of new bonds onto the directions of old bonds to the prescribed lengths, instead of setting the lengths of new bonds l_1, l_2, ... l_i themselves. Therefore, a second step

$$\boldsymbol{r}(t+\delta t) = \left(\boldsymbol{I} - \boldsymbol{T}(t)\boldsymbol{B}(t)\right)\boldsymbol{r}'(t+\delta t) + \boldsymbol{T}(t)\boldsymbol{p}(t) \ , \tag{A.12}$$

is required to update coordinates, where $\boldsymbol{p}(t)$ is a projection vector for the correction. The elements of $\boldsymbol{p}(t)$ are given by

$$p_i = \sqrt{2d_i^2 - l_i^2} \ . \tag{A.13}$$

A.3   Thermostat

In this dissertation, we used a refined velocity rescaling algorithm proposed by Bussi *et al.*[139] for sampling the canonical distribution. It has a general procedure as follows:

(1) Evolve the system for a single time step, as described in A.2.

(2) Calculate the system kinetic energy.

(3) Evolve the kinetic energy for a single time step using an auxiliary stochastic dynamics. The auxiliary dynamics obeys the expression

$$dK = (K_0 - K)\frac{dt}{\tau} + 2\sqrt{\frac{KK_0}{N_f}}\frac{dW}{\sqrt{\tau}} \ , \tag{A.14}$$

where K is the system kinetic energy, K_0 is the desired kinetic energy, dt is the time step, τ is an arbitrary parameter with the dimension of time, N_f is the number of degrees of freedom, and dW is a stochastic Wiener process (a random number). The parameter τ, sometimes called the relaxation time, defines the intensity of temperature coupling. A larger τ means it takes longer to achieve the given kinetic energy. In our simulations, a τ of 0.1 ps was used.

(4) Rescale velocities in the manner of

$$\left(\boldsymbol{v}(t + \frac{\delta t}{2})\right)^2 = \left(\boldsymbol{v}'(t + \frac{\delta t}{2})\right)^2 + 2\boldsymbol{M}^{-1}dK \;, \tag{A.15}$$

so as to update the kinetic energy, where $\boldsymbol{v}'(t + \frac{\delta t}{2})$ and $\boldsymbol{v}(t + \frac{\delta t}{2})$ are velocities before and after rescaling.

A.4 Potential of Mean Force

The potential of mean force (PMF) of a system with N particles is the potential, if a set of particles $1 \ldots n$ keeps a fixed configuration, that gives the average force over all configurations of all remaining $n + 1 \ldots N$ particles acting on a particle i,[168]

$$-\nabla_i w = \frac{\int (-\nabla_j U) e^{-\frac{U(\boldsymbol{r})}{k_B T}} d\boldsymbol{r}_{n+1} \ldots d\boldsymbol{r}_N}{\int e^{-\frac{U(\boldsymbol{r})}{k_B T}} d\boldsymbol{r}_{n+1} \ldots d\boldsymbol{r}_N} \;, \tag{A.16}$$

where w is the PMF ($-\nabla_i w$ is the average force), U is the system potential energy, k_B is the Boltzmann constant, T is the absolute temperature, and $\boldsymbol{r}$ is the particle coordinates in the phase space.

The PMF $w(\eta)$ as a function of the reaction coordinate η is defined from the average distribution function

$$w(\eta) = w(\eta^*) - k_B T ln \left[\frac{\langle \rho(\eta) \rangle}{\langle \rho(\eta^*) \rangle} \right] \;, \tag{A.17}$$

where η^* and $w(\eta^*)$ are arbitrary constants. The average distribution function along the coordinate η, $\langle \rho(\eta) \rangle$, is obtained from a Boltzmann weighted average

$$\langle \rho(\eta) \rangle = \frac{\int \delta(\eta'[\boldsymbol{r}] - \eta) e^{-\frac{U(\boldsymbol{r})}{k_B T}} d\boldsymbol{r}}{\int e^{-\frac{U(\boldsymbol{r})}{k_B T}} d\boldsymbol{r}} \;, \tag{A.18}$$

where $\eta'[\boldsymbol{r}]$ is a function which allows the disturbance of a few degrees of freedom, and

$\delta(\eta'[\boldsymbol{r}] - \eta)$ is the Dirac delta function for the coordinate η.

The measure of a thermodynamic property obtained from average distribution functions is accurate provided that the system is ergodic. However, a high energy barrier along the reaction coordinate may cause poor sampling in the high energy parts of phase space, therefore, it is unrealistic to compute $w(\eta)$ or $\langle \rho(\eta) \rangle$ directly from straight MD simulations. Umbrella sampling[145, 146] is a technique to overcome the sampling problem by introducing artificial bias potentials, $U_i(\eta)$. In practice multiple simulations (windows) are conducted with different biased potentials $U^{\mathrm{bias}}(\boldsymbol{r})$, denoted by the subscript i. The unbiased PMF can be readily evaluated by biased average distribution functions

$$w(\eta)_i = w(\eta^*) - k_B T ln \left[\frac{\langle \rho(\eta) \rangle_i^{\mathrm{bias}}}{\langle \rho(\eta^*) \rangle} \right] - U^{\mathrm{bias}}(\boldsymbol{r}) + F_i \;, \tag{A.19}$$

where $U^{\mathrm{bias}}(\boldsymbol{r})$ is the biased potential

$$U^{\mathrm{bias}}(\boldsymbol{r}) = U(\boldsymbol{r}) + U_i(\eta) \;, \tag{A.20}$$

and F_i is a constant associated with $U_i(\eta)$ by

$$e^{-\frac{F_i}{k_B T}} = \left\langle e^{-\frac{U_i(\eta)}{k_B T}} \right\rangle \;. \tag{A.21}$$

After obtaining individual $w(\eta)_i$ the free energy curves are recovered with the weighted histogram analysis method (WHAM).[147] The global $\langle \rho(\eta) \rangle$ can be written as

$$\langle \rho(\eta) \rangle = \frac{\sum\limits_i n_i \langle \rho(\eta) \rangle_i^{\mathrm{bias}}}{\sum\limits_i n_i e^{-\frac{w_i(\eta) - F_i}{k_B T}}} \;, \tag{A.22}$$

where n is the number of independent data points of individual simulations. The constants F_i required in the previous equation are determined from

$$e^{-\frac{F_i}{k_B T}} = \int \langle \rho(\eta) \rangle \, e^{-\frac{w_i(\eta)}{k_B T}} d\eta \;. \tag{A.23}$$

which again needs the input of $\langle \rho(\eta) \rangle$. Practically, Equations (A.22) and (A.23) are solved through an iteration procedure so that $\langle \rho(\eta) \rangle$ and the set of F_i are self-consistent.

Appendix B

Discussion of Some Simulation Details

B.1 Cell Dimension

To verify that the dimensions of our simulation cell are not seriously influencing the results, additional simulations were performed with higher cell reservoirs (4.004 versus 2.004 nm), and the results obtained are given in Table B.1. We note that the results agree within standard deviations. It also has been reported[95, 142, 169, 170] that the length of CNT has a negligible effect on the water conduction rate.

B.2 Thermostat

As demonstrated by Thomas and Corry,[171] the thermostat employed can influence water flow dynamics through nanoscopic channels. They found that temperature control algorithms that introduce random forces, for example, the Langevin method, can lead to flow rates which depend on the length of the CNT, whereas velocity rescaling algorithms do not. Although it is not clear which type of thermostat more closely resembles a real experimental situation, we used the velocity rescaling algorithm presented by Bussi *et al.*[139] We also examined the Berendsen thermostat,[172] which is one of the velocity rescaling thermostats investigated by Thomas and Corry,[171] to test for any influence on the flow rate. The results are tabulated in Table B.2 and suggest that the flow rate is not unduly sensitive to details of the velocity rescaling thermostat employed.

B.3   Implementation of Pressure Difference

In Chapter 2.5 we discussed that an improper selection of the region where the external force f_{ex} is applied could adversely influence the fluid dynamics. To validate our choice of region thickness, which is 0.2 nm, we further tested two other thickness values: 0.4 nm and 2.0 nm (full reservoir). The results are summarized in Table B.3, and confirm that our application is reasonable, while the full reservoir method of Reference 141 obviously alters the fluid dynamics.

To work more efficiently with the GROMACS package, we arbitrarily defined the time interval of subset update as 10 ps. Another two periods, 5 ps and 25 ps, were investigated under the same conditions. The results are displayed in Table B.4, demonstrating that the selection of the time interval does not have a discernible effect on water flow rates.

We met an unexpected issue for simulations involving ions. If we applied the external force to both water molecule and ions within the selected region, it resulted in unequal NaCl concentrations at steady state, with the feed reservoir having a higher concentration than the downstream reservoir. For example, a feed solution initially at 1 mol L^{-1} ends up at approximately 1.6 mol L^{-1} at steady state. Also, the observed ion flow rates increase, as shown in Table B.5. We believe that this is a systematic artifact of periodic boundary conditions and finite size. Concentration separation did not occur if the force was applied only to water molecules. Interestingly, when we carried out simulations for a 1.6 mol L^{-1} solution without the exerting force on the ions, we obtained ion flow rates similar to those for a 1 mol L^{-1} solution applying force on the ions (Table B.5). It suggests that the flow rate increase is mainly due to the ion concentration increase in the feed reservoir, rather than to some fundamental changes in flow dynamics.

Water model	$R_{\text{flow,2.0nm}}$ (ns^{-1})	$R_{\text{flow,4.0nm}}$ (ns^{-1})
TIP4P/2005	22 (3)	23 (2)
SPC/E	34 (2)	30 (3)
TIP3P	59 (2)	61 (4)

Table B.1: Effect of the cell dimension on water flow rates. The simulations were conducted at 300 K for a (6,6) CNT. R_{flow} is the average water flow rate. The numbers in parenthesis are estimated standard deviations.

Water model	$R_{\text{flow,Bussi}}$ (ns^{-1})	$R_{\text{flow,Berendsen}}$ (ns^{-1})
TIP4P/2005	22 (3)	20 (3)
SPC/E	34 (2)	31 (4)
TIP3P	59 (2)	61 (2)

Table B.2: Effect of the thermostat employed on water flow rates. The simulations were conducted at 300 K for a (6,6) CNT. R_{flow} is the average water flow rate. The numbers in parenthesis are estimated standard deviations.

Water model	$R_{\text{flow,0.2nm}}$ (ns^{-1})	$R_{\text{flow,0.4nm}}$ (ns^{-1})	$R_{\text{flow,2.0nm}}$ (ns^{-1})
TIP4P/2005	22 (3)	22 (2)	48 (2)
SPC/E	34 (2)	32 (2)	68 (1)
TIP3P	59 (2)	63 (1)	131 (5)

Table B.3: Effect of the thickness of the force-exerted region on water flow rates. The simulations were conducted at 300 K for a (6,6) CNT. R_{flow} is the average water flow rate. The numbers in parenthesis are estimated standard deviations.

Water model	$R_{\text{flow,10ps}}$ (ns^{-1})	$R_{\text{flow,5ps}}$ (ns^{-1})	$R_{\text{flow,25ps}}$ (ns^{-1})
TIP4P/2005	22 (3)	21 (1)	22 (2)
SPC/E	34 (2)	35 (1)	36 (4)
TIP3P	59 (2)	64 (3)	59 (1)

Table B.4: Effect of the update frequency of the force exerted region on water flow rates. The simulations were conducted at 300 K for a (6,6) CNT. R_{flow} is the average water flow rate. The numbers in parenthesis are estimated standard deviations.

Force on ions	c_{initial} (mol L^{-1})	c_{steady} (mol L^{-1})	Water model	R_{flow} (ns^{-1})	
				Na$^+$	Cl$^-$
No	1	1	TIP4P/2005	0.4 (0.2)	0.2 (0.2)
			TIP3P	3.1 (0.4)	2.2 (0.5)
Yes	1	~1.6	TIP4P/2005	0.8 (0.4)	0.6 (0.3)
			TIP3P	5.2 (0.2)	4.1 (0.4)
No	1.6	1.6	TIP4P/2005	0.6 (0.4)	0.4 (0.2)
			TIP3P	4.8 (0.3)	3.7 (0.3)

Table B.5: Effect of the external force on ion flow rates. c_{initial} and c_{steady} are concentrations of the solution in the feed reservoir before and after steady states were reached, respectively. R_{flow} is the average ion flow rate. The numbers in parenthesis are estimated standard deviations.